Up-scalable plasmonic and diffractive nanostructures

THÈSE N^O 6782 (2015)

PRÉSENTÉE LE 22 OCTOBRE 2015
À LA FACULTÉ DES SCIENCES ET TECHNIQUES DE L'INGÉNIEUR
LABORATOIRE DE NANOPHOTONIQUE ET MÉTROLOGIE
PROGRAMME DOCTORAL EN PHOTONIQUE

ÉCOLE POLYTECHNIQUE FÉDÉRALE DE LAUSANNE

POUR L'OBTENTION DU GRADE DE DOCTEUR ÈS SCIENCES

PAR

Fabian Michael LÜTOLF

acceptée sur proposition du jury:

Prof. C. Moser, président du jury
Prof. O. Martin, Dr M. Stalder, directeurs de thèse
Prof. O. Parriaux, rapporteur
Dr A. Hafner, rapporteur
Prof. H. P. Herzig, rapporteur

EPFL

ÉCOLE POLYTECHNIQUE
FÉDÉRALE DE LAUSANNE

Suisse
2015

Abstract

Since most of the academic photonic and plasmonic nanostructures are based on slow and expensive electron beam lithography processes, there is a need for innovative alternatives suitable for industrial manufacturing. Large areas need to be patterned with a high–throughput, which is for example achieved with roll–to–roll machines. Up–scalable designs of photonic and plasmonic nanostructures are therefore studied in this thesis. Typical industrial processes include embossing and evaporation, which are consequently used throughout the thesis.

Diffractive gratings for example have recently been proposed for display backlights and solar cells; both of which require large area processing. Up–scalable fabrication of broad–band diffractive gratings for unpolarized light is therefore addressed in this thesis. I propose oblique evaporation of high refractive index materials to render binary gratings highly efficient for first order transmission. Zinc sulfide coatings are employed to diffract close to 70% of unpolarized green light. The replication of these gratings is not demanding when compared to state-of-the-art blazed gratings and also does not require specific (high refractive index) substrates. Furthermore, simulations show that they can be encapsulated to protect them from environmental influences like humidity, wear or dust, while retaining their exceptional diffractive properties. The research reported in this thesis offers an industry–compatible solution for existing applications, which makes rapid implementation into commercial products very realistic.

An important roll–to–roll producer of nanostructures is the security industry. Striking optical effects are highly demanded for the verification of the authenticity of banknotes or ID cards, but also for brand protection. In the advent of polymeric banknotes and display devices like smart phones, transmission based security features have received a lot of attention recently. In this thesis, I show that asymmetric, thin metallic coatings can attain diffraction efficiencies above 70% for TE polarized light. The effect is asymmetric and shows a maximum at the Wood–Rayleigh anomaly, which results in orientation dependent coloration of the zero order as well as first order transmittances. A large part of the standard RGB gamut can be covered through proper adjustment of the grating parameters. Combination of zero order and first order effects allows creation of color appearances that switch when rotating or flipping the device. I finally present how floating images become apparent when a patterned light source like e.g. a mobile phone is used in conjunction with the metallized grating. These effects could therefore find application in the aforementioned transmission based security features.

In contrast to diffractive structures, which are readily produced with roll–to–roll machines, only few reports were found for plasmonic structures fabricated on large areas or with high throughput processes. This can be understood in the context of the much shorter history of plasmonics, as the interest in the field has been reinvigorated only around 20 years ago. The complex interactions between plasmonic modes are therefore still the main subject of research and only a few mature applications, mainly in the area of biosensing, have emerged to date. The difficulties in transferring plasmonic technology from universities to industry are a main reason for this: in academia, metallic nanostructures often require a lateral resolution of a few nanometers, which is challenging to achieve in up–scalable processes. Thicknesses on the other hand can be controlled in this regime using evaporation techniques, which are hence a powerful technique for high–throughput production.

In this thesis, Fano-resonant, U-shaped nanowires are created with oblique metal deposition. Although similar structures were reported previously, they relied on deep subwavelength gratings coated with gold [1]. In order to make them available for mass-production, the period is therefore increased and aluminum is chosen as the plasmonic material. These changes demand reevaluation of the plasmonic modes forming the Fano-resonant system. The surface integral equation method is used to investigate near-fields and charge distributions, which shed light onto the physics behind the present resonances. A surface plasmon polariton is found to couple to a localized plasmonic mode with a hexapolar charge distribution. Further understanding of the interactions at hand is gained by considering both aluminum and gold nanostructures in parallel. It is finally shown that the Fano-resonance can be accurately tuned by adapting evaporation angle and metal thickness. These two parameters can easily be accessed and would allow for good control over the optical response even in an industrial environment.

The applicability of the above insights is then demonstrated by creating a strain sensor. To that end, the process is transferred to a stretchable polymer and when elongating the structure perpendicular to the wires, the polymeric spacing between them is expanded. The sensitivity of the Fano-resonance to this change in inter-wire distance is investigated and a strong damping is observed for increasing gaps. This damping is attributed to destructive interferences from the Wood-Rayleigh anomaly, which shifts close to the Fano-resonance upon strain. Through careful design, a clearly visible color switch from purple to green is achieved for elongations less than 20%. The sensor was deemed to be very durable, as no deterioration in the color or the spectral response was observed even after several strain cycles. This finding could lay the foundations for a low-cost, large area strain sensor, which can be conveniently evaluated remotely or even with the naked eye.

Keywords: Diffraction, plasmonics, Fano-resonance, strain sensing, color effect, periodic nanostructure, oblique deposition, high-throughput, up-scalable production, Wood-Rayleigh anomaly, UV replication, hot embossing, optical grating, laser interference lithography, numerical simulation.

Zusammenfassung

Die Erforschung innovativer Lösungen für die industrielle Herstellung photonischer und plasmonischer Nanostrukturen ist notwendig, da die meist benutzten Verfahren auf der langsamen, teuren Elektronenstrahllithografie basieren. Das Strukturieren grosser Flächen mit hohem Durchsatz kann z.B. mit Rolle−zu−Rolle Maschinen erreicht werden, bei welchen diese Technologie nicht integrierbar ist. Da stattdessen Prägen und Aufdampfen die am häufigsten verwendeten Prozesse in solchen Anlagen sind, können die hier untersuchten Strukturen mit diesen Techniken hergestellt werden.

Beugungsgitter, die am weitest verbreiteten optischen Nanostrukturen, sind nicht nur der Ausgangspunkt für diverse Elemente in der Sicherheitsindustrie, sondern werden seit Kurzem auch für die Beleuchtung in Bildschirmen oder zur Effizienzerhöhung von Solarzellen eingesetzt. Gerade diese beiden Anwendungsbereiche benötigen grossflächige Strukturen, weshalb skalierbare Herstellungsmethoden attraktiv sind. Bei diesen Fällen ist vor allem polarisationsunabhängige Diffraktion gefragt, welche ich mittels Schrägaufdampfen von hochbrechenden Materialien erreichen konnte. Mit diesem Verfahren können binäre Gitter mit bis zu 70% unpolarisierter Diffraktionseffizienz in der ersten Transmissionsordnung versehen werden. Die Replikation dieser Gitter ist dabei wesentlich einfacher als diejenige von bekannten Alternativen und stellt auch keine Anforderungen an den Brechungsindex des Substrats. Des Weiteren können sie eingebettet werden ohne die hohe Beugungseffizienz zu verlieren, was einen wirksamen Schutz vor Umwelteinflüssen wie Feuchtigkeit, Partikeln oder mechanischer Beanspruchung ermöglicht.

Die oben erwähnte Sicherheitsindustrie ist wohl einer der grössten Hersteller von Nanostrukturen, welche Rolle−zu−Rolle Verfahren nutzen. Auffällige optische Effekte sind sehr wichtig zum Nachweis der Echtheit von Banknoten oder Ausweisen, aber auch für den Markenschutz teurer Produkte. Durch die steigende Verbreitung von Polymer−Banknoten und Bildschirm−Geräten wie z.B. Smartphones, haben vor allem Sicherheitsmerkale mit Transmissionseffekten seit Kurzem viel Beachtung erhalten. In meiner Arbeit zeige ich, dass dünne, asymmetrische Metallbeschichtungen Diffraktionseffizienzen von über 70% für s−polarisiertes Licht ermöglichen. Dieser Effekt ist asymmetrisch und zeigt ein Maximum bei der Wood−Rayleigh Anomalie, was zur ausrichtungsabhängigen Färbung der nullten sowie der ersten Beugungsordnung führt. Ein grosser Teil der standard RGB Farben können durch Anpassen der Gitterparameter erreicht werden. Die Kombination der Effekte aus erster und nullter Ordnung ermöglicht die Herstellung von Farben, die wechseln wenn das Substrat beispielsweise um 180° oder auf den Kopf gedreht wird. Schliesslich zeige ich, wie schwebende Bilder generiert werden können wenn das metallisierte Gitter mit einer schattierten Lichtquelle wie z.B. einem Smartphone beleuchtet wird. Diese Effekte könnten in transmissionsbasierten Sicherheitsmerkmalen verwendet werden.

Im Gegensatz zu Beugungsgittern, die bereits zuverlässig Rolle−zu−Rolle hergestellt werden können, sind plasmonische Strukturen bisher selten auf grossen Flächen oder mit hohem Durchsatz hergestellt worden. Dies ist wenig überraschend wenn man berücksichtigt, dass das Forschungsfeld der Plasmonik erst vor etwa 20 Jahren wiederbelebt wurde. Die Hauptthemen der Forschung sind dabei die komplexen Interaktionen zwischen plasmonischen Moden; nur im Bereich Biologie sind einige ausgereifte Anwendungen anzutreffen. Gründe dafür sind unter anderem die Schwierigkeiten im Technologietransfer: Universitäre Methoden benötigen eine

laterale Auflösung im Nanometerbereich, was mit skalierbaren Methoden sehr schwierig zu erreichen ist. Die Schichtdicke kann im Gegensatz dazu bei Verwendung eines Aufdampfprozesses im Nanometerbereich kontrolliert werden, was deshalb eine leistungsfähige Methode für die Massenproduktion ist.

Eine Schrägaufdampfung von Metallen wird in dieser Arbeit verwendet um Fano-resonante, U-förmige Nanodrähte herzustellen. Obwohl über ähnliche Strukturen bereits berichtet wurde, waren diese aus Gold und basierten auf Gittern mit sehr kurzen Perioden [1]. Um diese massenproduzierbar zu machen, wird in der vorliegenden Arbeit die Periode vergrössert und Aluminium als Material eingesetzt. Diese Veränderungen erfordern eine erneute Untersuchung der plasmonischen Moden, die das Fano-resonante System bilden. Die Oberflächenintegral-Gleichungs-Methode (surface integral equation method) wurde verwendet um Nahfelder sowie Oberflächenladungen zu untersuchen. Dies hilft, Klarheit in die Physik hinter den Resonanzen zu bringen. Die Berechnungen zeigen, dass ein Oberflächenplasmon an ein lokalisiertes Plasmon koppelt, welches eine hexapolare Ladungsverteilung zeigt. Durch die parallele Untersuchung von Gold und Aluminium wird ein tieferes Verständnis für die auftretenden Mechanismen erlangt. Es wird schliesslich noch aufgezeigt, wie die Fano-Resonanz durch Veränderung des Aufdampfwinkels oder der Metalldicke akkurat angepasst werden kann. Diese beiden Parameter können auch in einer industriellen Produktion sehr fein eingestellt werden und erlauben eine sehr gute Prozesskontrolle.

Die Anwendbarkeit obiger Erkenntnisse wird durch die Herstellung eines Dehnsensors gezeigt. Der Prozess wird dazu für ein dehnbares Polymer optimiert. Wenn dieses Substrat senkrecht zu den Drähten gestreckt wird, vergrössert sich der Abstand zwischen ihnen proportional. Die Sensitivität der Fano-Resonanz gegenüber dieser Entfernung wird untersucht und eine starke Dämpfung mit steigender Dehnung wird beobachtet. Dieser Effekt wird durch den destruktiven Einfluss der Wood-Rayleigh Anomalie auf die Fano-Resonanz verursacht, welche sich durch die Streckung spektral annähern. Dieser Mechanismus führt sogar bei Dehnungen unter 20% zu einer klar sichtbaren Farbänderung von violett zu grün. Der Sensor wurde ausserdem als widerstandsfähig befunden, da auch nach mehrmaligem Dehnen keine Verschlechterung der spektralen oder farblichen Antwort erkennbar ist. Diese Forschung könnte deshalb den Grundstein für günstige Dehnungssensoren legen, die grossflächig anwendbar sind und aus der Distanz oder sogar mit blossem Auge ausgewertet werden können.

Chapter 1   Introduction/Thesis Objectives

In academic research, innovation in photonics usually stops at sample sizes in the millimeter range, once the proof of concept could be made and the first applications could be tested. For most commercial applications, such sizes are however insufficient. Besides the need for different instruments capable of structuring sizeable areas, often the lab–scale approaches cannot be transferred to industrial fabrication at all, since they are not compatible with high–throughput, large–area production. The best known example in photonics is electron beam lithography, which is generally limited to low–throughput and small sizes due to its slow, serial patterning (depending on the resolution required). Consequently, the insights gained for such structures are of limited value for industrial manufacturing and often entirely new processes need to be developed. The latter is precisely the aim of this thesis, which focuses on high–throughput-compatible designs for photonic nanostructures.

The two main fields of research addressed in this thesis are diffraction gratings and plasmonic Fano–resonances. Both effects can be found in gratings, which are therefore a pillar of this thesis. Such periodic nanostructures are found in nature, where they e.g. account for the iridescent colors exhibited by various butterflies [2], beetles [3] or birds [4]. Man–made imitations of such effects are highly demanded [5], since structural colors show no photobleaching as opposed to e.g. chemical pigments. Physical colors are hence very attractive for many applications, ranging from coloring of everyday objects like cars or buildings, over color filters for displays to striking features for security or brand protection. Unfortunately, these structures are very complex and require features with dimensions in the sub 200 nm range, which are much smaller than what could be fabricated by humans for a long time.

The first artificial periodic structures created were diffraction gratings. They have been popular for a long time due to their ability of spectrally splitting incident light with high efficiency. The invention of the optical grating dates back to at least the 18th century [6], but it took another century until reliable production was enabled by technological progress [7]. Gratings had to be ruled with high precision scribes, which of course severely limited the achievable periods. Gratings with periods in the 10 μm to 100 μm range are sufficient to split light into its spectral components and asymmetric échelle gratings achieve very high efficiencies in higher diffraction orders [8]. For this and other favorable properties, they have become very popular for spectrophotometers and laser cavities. Today, such gratings are still standard for the aforementioned applications.

In the advent of the significant progress accomplished in micro– and nanostructuring, the feature size of man-made gratings could be scaled down by several orders of magnitude and sub–wavelength features are readily attained today. Security holograms are probably the best known optical applications emerging from these advances. They rely on the dispersive nature of gratings, which allows spreading the visible spectrum across a wide angle of view. This leads to the well–known rainbow effect of such holograms. The security/brand protection industry in

general relies heavily on physical colors and constantly has to implement new optical effects in order to stay ahead of counterfeiters. A recent trend seen in this industry, sparked by the intro-introduction of polymeric bank notes in the past decade, is the development of security elements observable in transmission[9]. Transmissive effects can be fundamentally different from reflective ones and this field of research still offers a lot of room for exploration.

Another phenomenon facilitated by short period gratings is the guiding of light in glass, polymers or semiconductors: when the diffraction angle is sufficiently steep, light can be trapped in the grating substrate. Light-guiding based applications [10], [11] and solar cells [12] therefore started to rapidly incorporate this technology in the last decades, although up-scaled adaptations of nanostructuring methods like laser interference lithography [13] only recently provided the crucial large-area, subwavelength gratings required for these implementations. Such applications are therefore on the cusp of industrial adaptation, which makes them very attractive for industry oriented research.

The use of plasmonic resonances on the other hand dates back to the Romans, who manufactured stunning glass objects relying on metallic nanoparticles for coloration [14]. Although the exact cause of the colors was not known back then, the technique stayed popular for a long time as e.g. in the middle ages similar processes were used to create stained glass windows. Although plasmonic colors arise from the electromagnetic interaction between light and free electrons in metals, they are also physical colors and hence share most advantages, disadvantages and applications with the ones mentioned above. Recent interest in plasmonic resonances however is not only driven by these color effects, but rather by the ability of concentrating radiation to subwavelength volumes [15]. The possibility of locally enhancing the electric fields by several orders of magnitude is especially attractive for sensing [16], light harvesting [17] and photocatalytic reactions [18].

Fano-resonances are a particular type of plasmonic resonances that show an asymmetric lineshape and can exhibit very sharp spectral features [19]. This particular type of resonances can occur when two or more individual resonances interact [20]. The individual modes are usually supported by a system of nanostructures and the spectral response can be very sensitive to their exact arrangement, since near-field interactions between the individual components are a defining factor. Nanoscale rulers based on Fano-resonances have therefore e.g. been proposed for strain sensing [21]. Another benefit from using sharp spectral features is their colorful appearance to the human eye. Fano-resonances have consequently also been successfully applied for color effects [22]. Since these resonances are particularly favorable for both sensing and coloration, they have the potential for making nanoscale processes visible to the naked eye through color changes. An example of such a sensor has been presented for the visual detection of biomolecules on a nanohole array [23].

This thesis aims to make the above concepts available to high-throughput manufacturing with a focus on roll-to-roll viable fabrication methods. To that end, large-area structures attainable with embossing and evaporation processes are investigated. The physical properties of the found solutions are elucidated and possible applications are experimentally demonstrated.

The thesis starts with an introduction to the fundamentals of diffraction optics and plasmonics in Chapter 2. Recent applications of the two phenomena are then discussed and possible implementations of the present research are mentioned where applicable. The final section of this chapter is devoted to colorimetry, which plays a very important role in predicting the visual

appearance of the proposed structures. Chapter 3 describes the fabrication, measurement and simulation methods used in this thesis and compares them to the most popular alternatives. I will elaborate on the reasons for the choices and discuss the actual implementations of the tech-techniques in the lab.

Chapter 4 treats the work performed on diffraction gratings. First, a novel method for blazing symmetric, diffractive gratings is presented. It relies on the oblique deposition of either high refractive index materials or metals and results in first order transmittances of up to 70%. The metallized versions show strong colors in zero order as well as first order transmission. This property is used to design orientation–sensitive devices that change appearance when rotating or flipping them. Also, a floating image effect is demonstrated by using a smart phone displaying a black and white picture.

Chapter 5 subsequently discusses how plasmonic Fano–resonances can be attained with a low–cost, high–throughput technique. U–shaped nanowires fabricated with a shadow evaporation process are shown to exhibit a specific Fano–lineshape in reflection. The underlying physics is explored through near–field and charge simulations. It is shown how this knowledge allows controlling the resonance shape and position by simple changes in the evaporation parameters. I finally also demonstrate how the present nanostructures can be applied for strain–sensing. By patterning a stretchable Polyurethane polymer, the response of this Fano–resonant system to deformation can be monitored. A distinct damping of the resonance is found upon tensile stress and a clear color change can be observed with the naked eye.

The conclusions and an outlook on possible future directions are given in Chapter 6. The following pages include the references, a list of the abbreviations used and the acknowledgements. My CV and a list of the publications, patents and presentations produced throughout the course of these doctoral studies conclude the thesis.

Chapter 2   Fundamentals

2.1   Diffracting light with gratings

The first man-made diffraction grating is attributed to Mr. Rittenhouse (1786), who based his experiments on the observations of Sir Isaac Newton [6]. At his time, Rittenhouse used a wireframe, screws and hairs to create a periodic structure. His approach could soon be scaled down thanks to the development of reliable machining processes; Henry Augustus Rowland's high precision ruled gratings could e.g. be used to create photos of the solar spectrum in 1894 [7]. Nowadays, most of these mechanical fabrication processes are replaced by lithography and/or imprinting, allowing for nanometer-scale precision and highly parallel production [24]. The reasons for our interest in periodic structures such as gratings has changed a lot since then and I will discuss recently marketed products relying on diffraction. To that end, I will start by describing the basic grating physics before turning to the actual applications. It is worth noting that periodic structures have also become very popular in the field of plasmonics; a topic that will be covered in Section 2.2.

2.1.1   Principles

Diffraction gratings are oftentimes compared to dispersive prisms because they can also be used to split light into its spectral constituents. Apart from this property, the two objects do not have very much in common: Prisms are made of a transparent bulk material that is formed into a certain macroscopic shape and shows one or multiple flat surfaces (triangles are the most widespread examples). The material has to be transparent and dispersive (its refractive index n varies with the wavelength λ of the incident light) for the wavelengths it should split. In the case of gratings, no special requirements with regard to the material's dispersion exist since the main determinant for its optical properties is its microscopic structure. Although gratings might appear flat to the naked eye, they show corrugations that typically range between tens of nanometers and several micrometers in size. Figure 1 (a) shows a magnified sketch of a one dimensional diffraction grating.
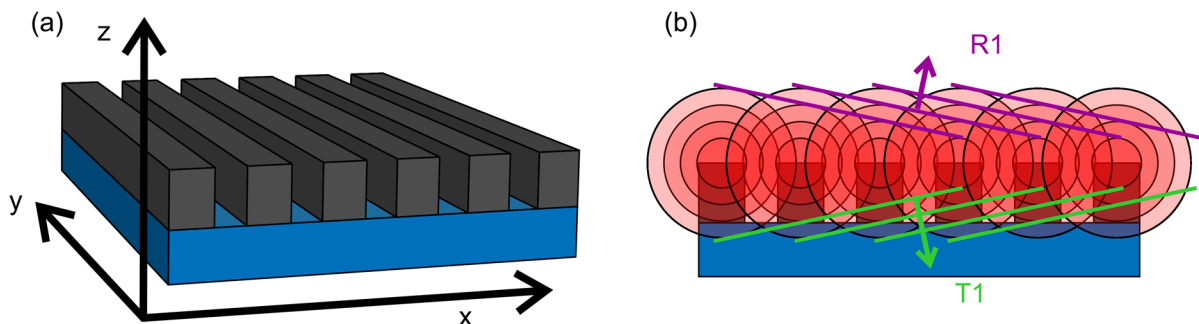
Figure 1. (a) Scheme of a 1D diffraction grating. (b) Sketch illustrating occurrence of higher orders.

The structure consists of a pattern that is periodically arranged in one direction (x) and approximated as infinitely long in the second in-plane direction (y). In the direction

perpendicular to the grating surface (z), the refractive index changes from the substrate material to the grating material and finally to the surrounding material. Some of the materials may also be identical: Substrate and incident media could both be air for a suspended grating or the grating material could be identical to the substrate material if the structure is e.g. embossed into a polymer. If a plane light wave impinges onto such a periodically corrugated surface, one can imagine that a cylindrical wave spreads from each of the grating fringes (Huygens–Fresnel Principle). Figure 1 (b) illustrates this idea; the circular lines indicate places of identical phase. At a given angle, positive interference occurs as illustrated by the green lines for the first transmission order (T1) and the purple lines for the first reflection order (R1). The angle at which such interference occurs can be determined analytically with:

$$\theta_m^{T/R}(\lambda) = \sin^{-1}\left(\frac{n_1(\lambda)\sin(\theta_i) + \frac{m\lambda}{\Lambda}}{n_2(\lambda)}\right), \qquad [2-1]$$

where n_1 is the refractive index of the incident medium, n_2 the refractive index of the substrate (for the reflected orders or embedded gratings: $n_1 = n_2$), Λ the period of the grating, m the diffraction order, θ_i the angle of incidence and λ the vacuum wavelength of the impinging wave. Figure 2 (a) illustrates the solutions of the equation and the parameters geometrically for the transmitted orders. In literature, this interference phenomenon is also often described as adding the reciprocal lattice vector ($\vec{K}, |\vec{K}| = \frac{2\pi}{\Lambda}$) to the wave vector ($\vec{k}$) of the incoming light. The wave vector notation is especially popular in the field of surface plasmons (which are in a sense a special case of the above described diffraction, where the outgoing wave propagates in x–direction along the interface, see chapter 2.2). I will consistently use wavelengths and angles throughout this thesis, but conversion to the wave vector representation is straightforward with $|\vec{k}_z| = \frac{2\pi}{\lambda}\cos(\theta)$ and $|\vec{k}_x| = \frac{2\pi}{\lambda}\sin(\theta)$.

The direct wavelength dependence of the diffraction angle in Equation [2–1] also explains why gratings split white light into its spectral components even in the absence of material dispersion ($n(\lambda) = const.$). A more figurative explanation can be obtained from Figure 1 (b): The radii of the circles scale with the wavelength of the light, longer wavelengths therefore experience positive interference at a steeper angle than short ones. This dispersion leads to a "rainbow effect", which is visible to the naked eye. The resulting angle-dependent colors form the basis for holograms, which will be discussed in Section 2.1.2.
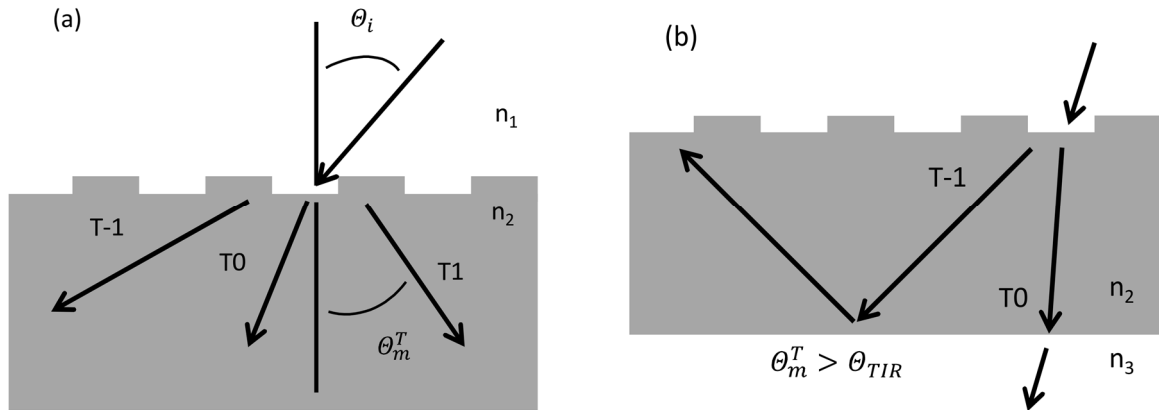
Figure 2. (a) Assignment of variables for a typical diffraction geometry and (b) occurrence of total internal reflection for higher order modes.

Another less obvious interaction that possibly occurs after diffraction is total internal reflection (TIR) at the subsequent interface with $n_3 < n_2$. The total internal reflection angle can be extracted from Snell's law:

$$\theta_{TIR} = \sin^{-1}\left(\frac{n_3(\lambda)}{n_2(\lambda)}\right). \qquad\qquad [2\text{–}2]$$

If light is for example diffracted at a sufficiently steep transmission angle θ_m^T, it is possible that TIR occurs at the back side of the grating piece. Light will therefore not exit from the back of the sample if the simple condition $\theta_m^T > \theta_{TIR}$ is met (Figure 2 (b)). For ideal dielectric interfaces, such a reflection is lossless. This phenomenon lays the foundations for the excitation of optical waveguide modes and motivates gratings as a means to feed light into them (see Section 2.1.2). If θ_m^T surpasses 90°, light of the particular wavelength cannot be diffracted into the order m anymore and only lower order diffraction is present. It is also at this precise wavelength that a feature called Wood–Rayleigh (WR) anomaly will be visible in one or several of the still present diffraction orders [25]. The anomaly manifests in the form of an extremum or a kink in at least one of the lower order spectra.

It might be astonishing at first that the diffraction angles do not depend on the grating material or shape, but when considering Figure 1 (b) we easily see that only the grating period and the surrounding materials influence the angles at which positive interference takes place. Material and shape however do become important when efficiencies (η) are of interest. For the exact determination of diffraction efficiencies, simulations are required. Modern simulation tools can handle arbitrary forms or materials and only require sub-minute computation times. More information on simulations can be found in Section 3.4. Some fundamental limits can however be imposed to diffraction efficiencies through consideration of symmetry and reciprocity. When dealing with symmetric gratings (in x–direction) at perpendicular incidence (or incidence within a solid angle centered around the surface normal), each positive order needs to have the same efficiency as the corresponding negative order ($\eta(m) = \eta(-m)$). As a consequence, all the non–zero orders will show diffraction efficiencies below 50% in such a configuration. This constraint is released for oblique incidence or gratings with asymmetric lineshapes. Such "blazed" gratings have therefore become prevalent in diffraction applications and a short review on the existing types will be given in Section 4.1.

2.1.2   Applications of Diffraction gratings

Gratings have been applied in spectrophotometers and lasers for several decades. In spectrometry, they replaced and outperformed bulky prisms [26]. For laser physics, especially blazed gratings (showing an asymmetric line shape) became very popular as they are capable of reflecting close to 100% of the incoming light in certain configurations. This feature together with the mode filtering provided by the grating dispersion [27] let such structures become standard components for cavities. Those two well-known applications will not be discussed any further, but they already illustrate three main incentives for using gratings: They can be smaller, more efficient and easier to fabricate than their non-diffractive counterparts. Although diffraction gratings are perceived as an "old" technology nowadays, there is still room for innovations as will be presented in Chapter 4. Also, technologies based on diffraction gratings are at a stage that is readily transferrable to industrial partners, which is CSEM's mission and therefore a linchpin of this thesis.

Wave/Light guiding

Coupling light into fibers, strips or slabs and guiding it in a theoretically lossless fashion is incredibly important for optical communications and circuits. Historically, most of the research has been devoted to silicon dioxide (SiO_2, fused silica) based systems as they are used for telecommunication purposes. The most prominent example of course is the glass optical fiber, which is not only used in almost every optical lab but also deployed in large data transmission networks, such as e.g. across the Atlantic Ocean [28]. Those fibers usually consist of a core, in which the light travels, a cladding and a coating for protection. The refractive index of the cladding has to be lower than the one of the core in order to prevent the light from leaking into the cladding (equation [2-2] would have no real solution and no total internal reflection would occur between core and cladding). Optical fibers exist in either single- or multi-mode variants. The single-mode fiber has a smaller core and is designed to support only one optical mode. The main advantage of this kind of fiber is the possibility of minimizing dispersion and therefore the ability to support higher bit-rates than their multimode counterparts [29]. Multimode fibers have a larger core and its exact size and shape determines the types of modes supported. Heavily multimode guides, which are used in this thesis, are often referred to as light guides, whereas the term waveguide is typically used for structures supporting only one or a few modes. Such guides can also have various other shapes: Strip waveguides e.g. maintain the two dimensional confinement but have a rectangular cross section. Slab waveguides on the other hand are only confined in one dimension. Like fibers, both of these waveguide geometries can be realized in different systems, including photonic crystals [30], [31], silicon-on-insulator materials [32], [33] or diverse polymers [34], [35]. Although less prevalent than fibers, planar waveguides are of high interest for integrated optical systems and low-cost applications (due to the cheap polymers and easy processing available). Energy and cost efficient LEDs can thereby e.g. be used in conjunction with patterned polymer slabs.
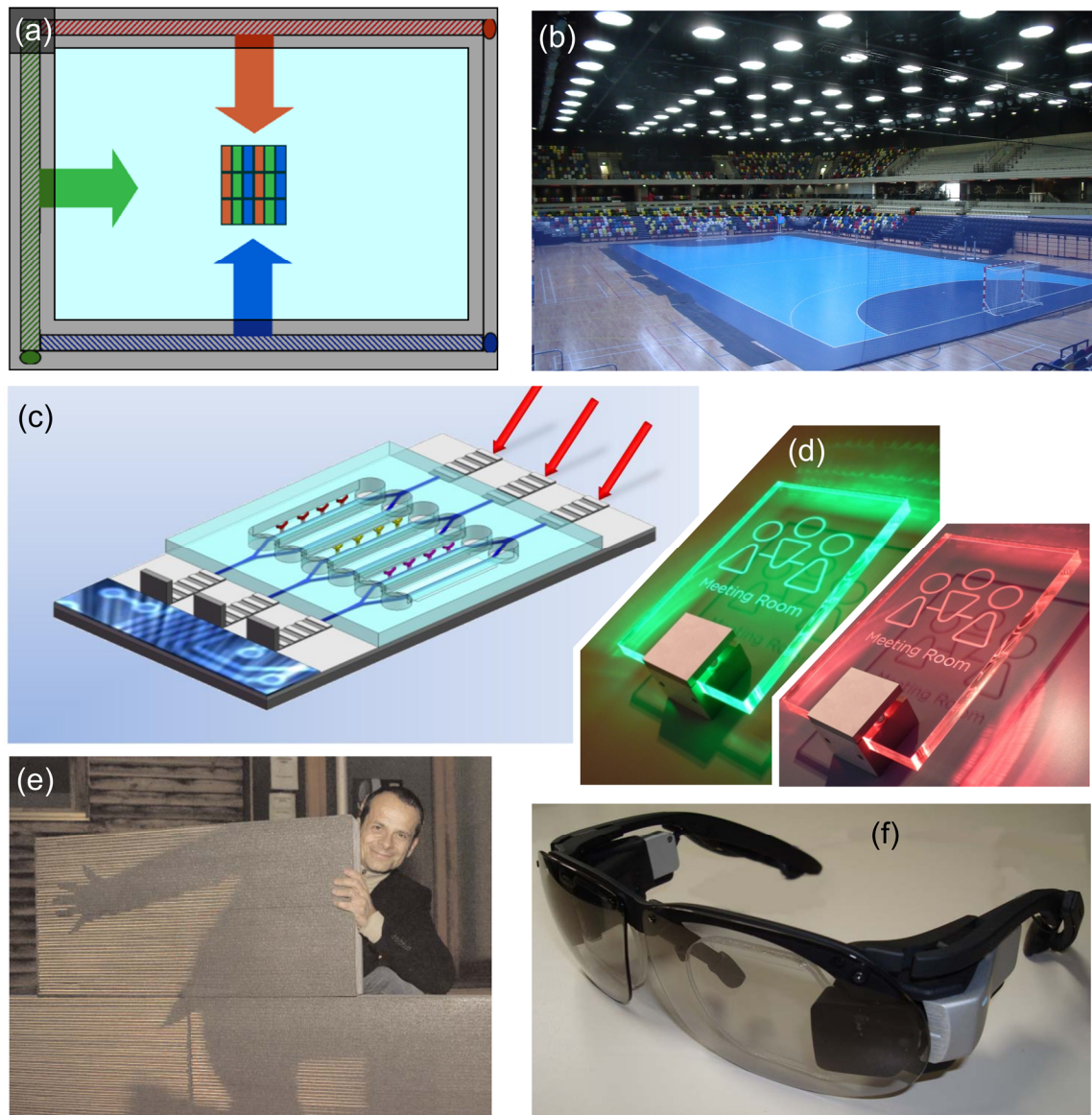
Figure 3. Applications of Light guiding: (a) backlights for displays [36], (b) light tubes for lighting buildings [37], (c) lab–on–a–chip [38], (d) meeting room signs [39], (e) light transmitting concrete [40] and (f) Near–to–eye displays [41].

Light guiding is making its way into a variety of applications, ranging from backlights for displays (Nokia, Figure 3 (a)) or lighting of buildings (Copper Box Arena London (b)) over Lab–on–a–chip signal transduction (nanoB2A (c)) to exotic applications like advertisement/information signs (Signbox Ltd. (d)) or light transmitting concrete (Luccon (e)). In a similar vein, the transduction of diffractively coupled images through slab waveguides has been proposed as a basis for Head–up or near–to–eye displays (Sony (f) but also Nokia/Vuzix [11]). Such systems could be produced at low costs, but they rely on efficient in– and outcoupling of radiation into light guides, which currently seems to work best with expensive volume holograms [42]. These devices could also greatly benefit from the diffractive structures presented in Section 4.2.

Security and brand protection

This application of gratings is well-known to a broad audience, since many valuable documents or electronic devices possess some sort of hologram to verify their integrity. They often incorporate a picture or logo, which makes them more difficult to counterfeit. In general, holograms or grating based security features have proven to be well suited for their task since they cannot be copied or photographed in a simple way. New security features however need to be developed regularly, since counterfeiters also gain access to modern replication and origination tools. It is therefore important to make such features hard to imitate by deterring forgers from observing certain parameters or by using sophisticated processes they cannot access. In the case of microstructures, it is also very important that the structure is neither directly accessible on a surface nor reproducible through a simple nanoimprint process. For the same reason, companies active in the field are reluctant to publish any information on their devices, since this could also enable counterfeiting them [43]. It is therefore understood that none of the structures discussed in this section or in the results are fully disclosed, unless they are either not directly intended for security applications or then already outdated.

As holograms are already very well described devices, I will only briefly touch this topic and refer the reader to existing literature for further details [44], [45]. In short, holograms are pictures recorded with a coherent light source such as a laser. The interference between the incoming wave and the diffusely reflected beam off the object thereby forms a fringe pattern. This pattern can be recorded in a volume of photosensitive material to realize a so-called volume hologram, or a flat substrate, such as on a photoplate or in a photoresist, which then results in a surface hologram. A diffractive picture of the object is observed after fixation of the fringe pattern. Typical surface holograms are covered with a metallic or high refractive index coating to enhance the visibility of the effect. An additional embedding layer is applied to protect the structure from wear and disable forgers from accessing the surface. Several more sophisticated types of holograms have been developed recently, with optically variable devices (OVDs) being one of the most attractive amongst them. Kinegrams® (e.g. on Swiss ID cards), dot matrix holograms (e.g. former packaging of Microsoft products) and Rainbow Holograms (e.g. Dove on VISA cards) belong to this class of devices and share the property of moving or switching parts upon reorientation of the hologram [46], [47]. A basic concern with all of these variations is that a customer does not know how the hologram has to look like, which opens up the market to poor counterfeits exhibiting any sort of first diffraction order effect [48]. The industry has therefore started to shift its attention to effects that show no rainbow effects to prevent such simple forgeries.

Holograms are not the only security features based on periodic nanostructures. Inspired by nature [49], structural zero order colors (visible in direct reflection or transmission instead of first order) are also popular [50]. One example is the so called diffractive identification device (DID) [51]. It is also based on diffractive gratings, but the diffracted light does not become visible to the observer and hence no rainbow effect is visible. This can be achieved by using lower grating periods, which do not diffract visible wavelengths towards the spectator in the chosen configuration. Instead, all the radiation redirected into the 1st order is "missing" in specular reflection. Additionally, the different colors of a white light spectrum are resonating with the subwavelength gratings, enabling their selective transmission or reflection at various angles of incidences. This leads to an according modulation of the zero order spectrum and can, in combination with resonances above the WR anomaly, lead to very sharp spectral features [51]. An additional feature of this approach is the possibility of generating orientation dependent

colors: Since the different wavelength components impinging parallel to the grating lines are not reflected with the same efficiency as light impinging perpendicularly to them at the same angle, a rotation by 90° causes a visual color change. In contrast to previously produced OVDs, such security elements are well visible in any lighting conditions, including very diffuse ambient light. This mechanism is e.g. implemented to secure the data pages of the passports of more than 20 countries and in the Philippine bank note series shown in Figure 4. Another trend in banknotes is the use of polymers to incorporate transparent parts: The Reserve Bank of Australia introduced the first fully polymeric banknote containing a window with an OVD and other countries like Canada (or Switzerland for the subsequent series) adopted similar materials. Security features working in transmission are therefore also becoming an increasingly important topic in the industry. I present a candidate for such applications in Section 4.3. In that respect, plasmonic colors have also become very popular for zero order effects [9]. They are however not based on diffraction and will be treated in Section 2.2.4.


Figure 4. Philippine bank note exhibiting a DID security feature that switches color upon rotation by 90°.

It is finally worth noting that low costs and high throughput are especially important for document or bank note security due to the large volumes and the high replacement frequency required. The same is also true for brand protection, where the price becomes even more important. Brand protection is usually employed as a seal of quality by companies with high visibility. This signal for the customer adds value to the product, which turns its application also into a marketing argument. Large size, interactive objects like tamper seals are therefore often applied for their conspicuousness (e.g. certificate of authenticity on most Microsoft software). They allow such companies to face less competition and create a sort of quasi–monopoly. On the other hand, this position is also very appealing for counterfeiters due to the high margins they can realize by imitating successful brands.

Light harvesting

The basic idea behind using diffractive gratings for light harvesting is increasing either the path length of the light in the active medium of a photovoltaic device (compare Figure 5 (a), (b), (c)) or using guided modes to funnel the light (Figure 5 (d)). Elongation of the optical path within the absorber of a solar cell through surface structuring has been proposed decades ago [52], but no optimal structure has become evident in the meantime. It is not even clear whether periodic or

random structures should be preferred for this purpose [53]. The use of improper measurement setups and the resulting overestimation of efficiencies add another layer of confusion to a re-research field that is already hard to survey [54]. This thesis therefore aims to only give a brief overview on grating based concepts for solar cells applications, but eschews the comparison of performances.
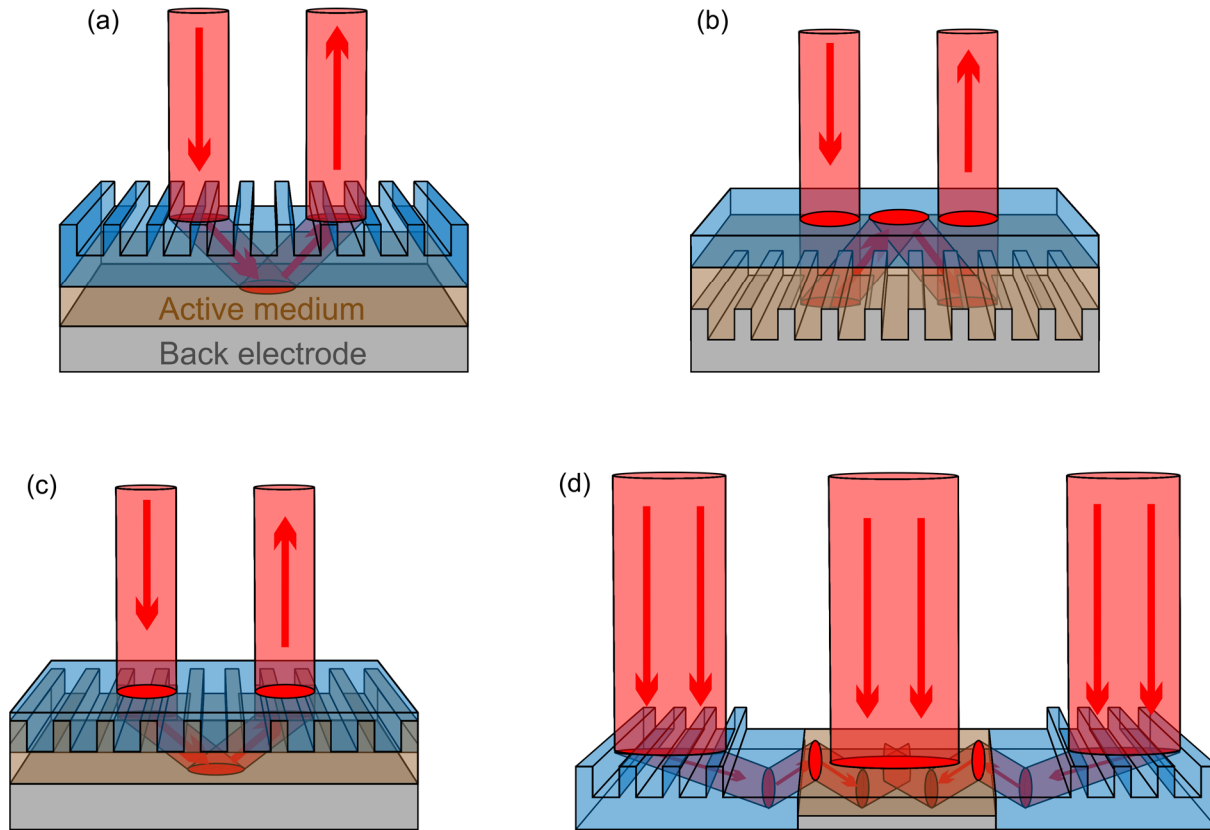
Figure 5. Applications of gratings in solar cells: Elongation of the optical path within a solar cell is achieved by patterning (a) the cover material, (b) the back electrode or (c) the active medium. (d) Shows a solar concentrator geometry enabled by grating diffraction and commercialized by Prism Solar Technologies Inc.

Optical path enhancement is still one of the most popular light management techniques for solar cell applications. It relies on the efficient redirection of light to make it impinge onto the semiconductor at a steep angle. Eli Yablonovitch proposed random structures for that purpose in the 1980s and also established the $4n^2$ limit for the achievable light concentration through surface structuring on a weakly absorbing bulk solar cell [55]. Periodic structures have subsequently been explored in the 1990s [56]. Neglecting near−fields and refractive index differences, they enable a wavelength dependent increase of the path through the cell, scaling with $1/\cos(\theta_m)$ (where θ_m is obtained from Equation [2−1]). Typical configurations therefore included patterning of the front surface (Figure 5 (a)) or the back reflector (e.g. the back electrode, Figure 5 (c)) [57]. Direct nanostructuring of the semiconductor's interface (Figure 5 (b)) on the other hand is a convenient approach for silicon solar cells, since silicon etching is a well−established and controllable process. Recently, this approach also received a lot of attention for other systems. Patterning the active material either on the front or the back side is especially favorable for high index semiconductors, since higher diffraction/scattering angles can be achieved in these geometries [58]. If structuring a lower index cladding layer, Snell's law

limits the angles available in the active material. Further, these approaches allow near–field in-interactions to take place and the transition away from the ray–optics regime bears the potential of pushing absorption beyond the $4n^2$ limit [59], [60]. This is also one of the driving incentives to use plasmonics in solar cells, a thriving field of research that will be covered in Section 2.2.4. When patterning the semiconductor or contacts, it is however very important to also consider (detrimental) electrical effects [61]. Introducing roughness to the interfaces can e.g. cause a significant increase in the surface recombination rate within the semiconductor. Coverage of this topic would however go beyond the scope of this thesis; the reader may therefore refer to the existing literature [62].

More recently proposed geometries rely on the guiding of light as depicted in Figure 5 (d) [63]. Here, the size of the absorber should be minimized and the light management structure covers the major part of the area. The total efficiency here cannot compete with full area solar cells due to outcoupling losses, but the cost–benefit–ratio is much better. Prior to gratings, luminophores have mainly been proposed for this form of solar concentration, sharing similar strengths and weaknesses [64], [65]. Such waveguide solar cells can find application in partially transparent objects like e.g. roofs or windows, since they mainly consist of semi–transparent coupling structures [66]. Commercial solar cell modules based on diffractive light guiding have recently been introduced to the market by Prism Solar Technologies Inc., who claim a significant energy yield improvement over standard solar cells [67]. The asymmetric diffraction gratings reported in Section 4.2 could help boosting such cells even further.

Finally, nanostructures can be used to decrease reflection losses (configuration Figure 5 (a) or (b)). A prerequisite is a deep–subwavelength feature size, such that the structure acts as an effective medium [68]. This implies that the optical response of the structure is solely governed by the volume fractions of the different refractive indices. A nanopyramid therefore e.g. represents a smooth transition from air to substrate and a binary grating acts as a layer of constant refractive index (adjustable by tuning the fraction of ridges). Antireflective structures are especially desirable for high refractive index substrates like silicon ($n_{Si} \approx 3.45$), since they exhibit large Fresnel reflections when interfacing air. With proper structuring, "black silicon" can be achieved in this way [69], [70].

Up–scalable production of light management structures is crucial. First, they should be available on large areas, since solar panels cover whole roofs, and second, their costs should not surpass the corresponding cost of an additional solar cell yielding the same performance enhancement. Industrial production of such structures is still very challenging [71], but roll–to–roll nanoimprinting of gratings could be a promising candidate for this purpose.

2.2   Plasmonic resonances

Plasmons represent the quanta of the combined free electrons and electromagnetic field oscillations that can occur in specific metals, so-called coinage metals, where the density of free electrons is so high that they behave like a solid-state plasma in the ion background. Although this definition includes light interaction with bulk materials, plasmons are more often associated with the resonant interaction of light with subwavelength metallic structures. Especially in the context of periodic arrays of metallic materials, two different types of plasmon resonances should be distinguished: Localized surface plasmon resonances (LSPR) and surface plasmon–polaritons (SPPs also known as propagating plasmon resonances). The former can be found in objects as old as the Roman Lycurgus cup [14] displayed in the British Museum (Figure

6), but the interest in plasmonic resonances has resurged only recently upon publication of the famous article by Ebbesen *et al.* on extraordinary optical transmission (EOT) through metallic subwavelength apertures [72]. This recent rediscovery of the topic is also one of the reasons for the relatively few products available incorporating plasmonics. A second reason can be found in the target fields of research: The most popular applications are related to biology [73], where development cycles tend to take longer due to the complexity of the systems. Medical applications finally are even more difficult to market due to the clinical trials and admissions required.
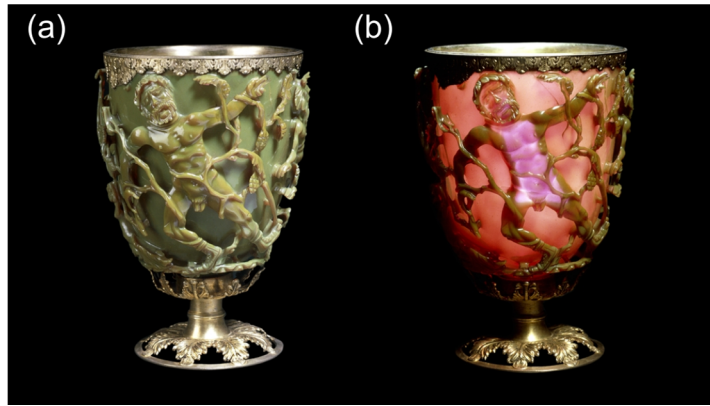
**Figure 6. Lycurgus cup (a) in reflection and (b) in transmission [74].**

2.2.1   Localized surface plasmon resonances (LSPR)

Localized surface plasmon resonances occur, when light interacts with confined free charges as e.g. present in particles or wires. The electric field of the irradiated light excites the conduction electrons and forces them to dislocate. Because of the fixed atomic cores of the metal, this periodic movement forms oscillating dipoles. Note that these movements cause current flows and therefore ohmic losses, since the metal conductivity at the frequency of light is finite. The size of the particles can be much smaller than the wavelength of light and the incident radiation is therefore concentrated to subwavelength volumes in this process. The wavelength dependent polarizability $\alpha(\omega)$ of a spherical particle in the quasi–static limit can be described by [75]

$$\alpha(\omega) = 4\pi\varepsilon_0 r^3 \frac{\varepsilon_1(\omega) - \varepsilon_2(\omega)}{\varepsilon_1(\omega) + 2\varepsilon_2(\omega)}, \qquad [2\text{--}3]$$

where ε_0 is the vacuum permittivity, r is the radius of the particle, $\varepsilon_1(\omega)$ is the complex permittivity of the particle and $\varepsilon_2(\omega)$ is the permittivity of the surrounding medium. We see that for $\varepsilon_1(\omega) = -2\,\varepsilon_2(\omega)$, the polarizability diverges. Assuming air as the surrounding medium ($\varepsilon_2(\omega) = 0$), the relation simplifies to $\varepsilon_1(\omega) = -2$. This corresponds to the resonance condition, where the electrons are maximally displaced. The results are a maximal scattering cross section, dipole moment and therefore field enhancement. For metals like silver, gold or aluminum this condition is fulfilled either in the UV or the visible. This resonance e.g. explains the different colors visible in transmission and reflection for the Lycurgus cup (Figure 6): At the resonance position, scattering becomes maximal and this scattered light (green) is visible under ambient lighting. In transmission, the light scattered by the nanoparticles is invisible to the spectator and the complementary color appears. Note that this simple approximation only works for particles much smaller than the wavelength (around 20 nm) [76]. For larger objects, the particle size and shape strongly affect the resonance wavelength [77]. Appropriate tuning of these properties has

become the most popular way of tuning the spectral position of plasmonic resonances in nano-nanoparticles.
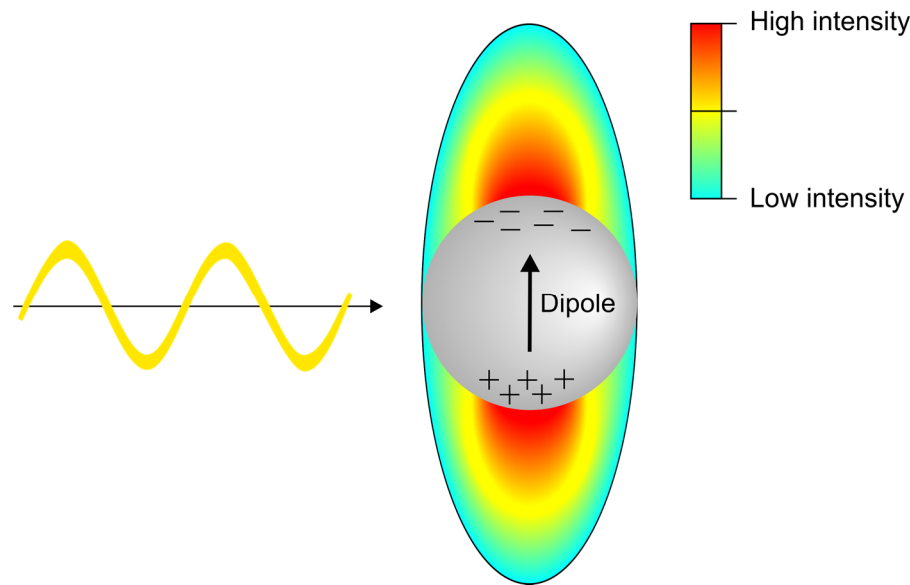
Figure 7. Response of a subwavelength plasmonic object to incoming electromagnetic radiation, the color scale shows the electric field intensity.

The deep–subwavelength resonance condition for infinite wires [75] would require $\varepsilon_1(\omega) = -\varepsilon_2(\omega)$. For wires however the polarization of the incoming light becomes crucial: Plasmonic resonances can only be excited if the electric field vector of the light is aligned perpendicularly to the wire, since the charges need to be confined when excited by the incoming field. This configuration is often referred to as TM or p–polarized incidence, although this is only true for the so-called classical mount (plane of incidence is perpendicular to the wire). When exciting LSPRs in any system, electric near–field intensities can surpass the intensity of incident light by several orders of magnitude (sketch in Figure 7). Favorable geometries for strong near–field enhancement usually include several particles or wires, arranged in such a way that they "funnel" the light to a defined spot (e.g. bowtie antennas [15]). Such high field enhancements are very crucial for sensing applications (e.g. Surface enhanced Raman Sensing [78]), solar energy harvesting or optical trapping [79]. If the E–field vector of the incoming light is parallel to the wire (TE in classical mount), the response of the electrons is more comparable to the one of bulk material and no localized plasmonic resonances can be excited. For an array of many parallel wires, TE polarized radiation is therefore usually strongly reflected at frequencies below the bulk plasma frequency. The plasma frequency is given by $\omega_p = \sqrt{\frac{ne^2}{\varepsilon_0 m_e^*}}$, where n is the density of electrons, e is the elementary charge, ε_0 is the vacuum permittivity and m_e^* is the effective electron mass. By properly tuning the grating parameters it is therefore possible to create highly efficient wire–grid polarizers [80].

2.2.2   Surface plasmon polaritons (SPP)

SPPs are propagating modes at a metal/dielectric interface. They consist of a fluctuating charge density at the metal surface and an exponentially decaying field into the dielectric as well as the metal (Figure 8 (a)). The wavelength of such a polariton is lower than the vacuum wavelength of the light it is excited with, which means that it cannot be launched by simply shining light onto a metal film. This effect is usually referred to as a mismatch between the momentum (or k–vector)

of the incident light and the momentum of the mode to be excited. The two most popular ways to excite SPPs on flat metal films include adding the missing momentum via the use of prisms or gratings. When using a prism, light can impinge onto a metal surface at an angle higher than the total internal reflection angle. The most popular geometry is the Kretschmann configuration: A prism is coated with a metal film and light is directed to this coating through the prism (Figure 10). At a specific, wavelength-dependent angle, the momentum can be matched and an SPP is excited. Figure 8 (b) shows how this coupling can be identified in typical rigorous calculations of the Kretschmann configuration: For a gold film on a glass substrate, we can choose the incident field coming from the glass side and then vary the angle of incidence θ inside the medium as well as the wavelength of the incoming light. At an angle slightly larger than the total internal reflection angle ($\theta_{TIR} \approx 41°$), a steep drop in reflectance becomes visible for this configuration (blue stripe). The decrease in reflection results from the absorbing nature of the excited plasmon as also illustrated by the decreasing electric field along the propagation direction in Figure 8 (a). The excitation angle for each wavelength is very sensitive to the refractive index close to the surface, which motivates this system for sensing applications (Section 2.2.4).
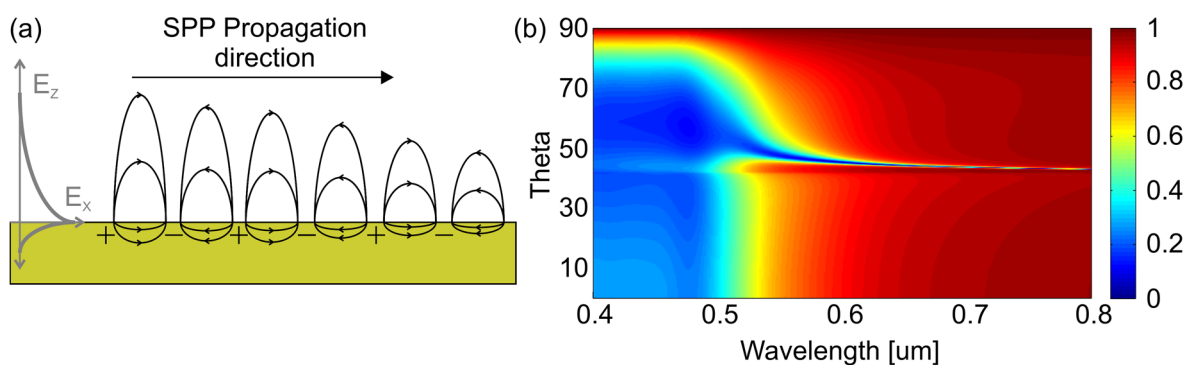
Figure 8. (a) Schematic of a propagating surface plasmon polariton and (b) SPP dispersion as found for TM polarized light reflecting off a 60 nm thick gold film at an air/glass interface (illuminated through the glass).

Note that, in a wire grating, SPPs and LSPRs may exist at the same time (among other resonances). Careful investigation of the present charges and near–fields as well as the dependence of the resonances on properties like e.g. materials or periodicity is therefore necessary to identify the occurring resonances. More details on the occurrence of different resonances in gratings will be provided in Section 5.1.

2.2.3 Materials

As mentioned earlier, metals are typically used in plasmonic devices since they provide negative permittivities, $\varepsilon_1(\omega) < 0$ with moderate imaginary parts, which are required to excite plasmonic resonances. Typical metal choices include the coinage metals (gold, silver, copper) and aluminum. Gold is especially popular for biological and chemical applications due to its chemical inertness and the established technique of (reversibly) thiol–functionalizing such surfaces. A major drawback of gold is its significant absorption in the visible (below ≈ 550 nm wavelength [81], see Figure 9) due to interband transitions. Another concern is its high cost: Although only thin layers or small particles are included in the final device, a multiple of this will be wasted during development and production. The existing applications of gold plasmonics therefore are usually rooted in biology, where manipulation of visible light is not required and costs are less of an issue. Silver is an attractive alternative. It has the lowest absorption of all the metals at wavelengths down to ≈ 350 nm wavelength and also features reasonable costs. Unfortunately,

silver oxidizes relatively quickly at ambient conditions. The tarnished silver (as e.g. in Ag_2S or AgO) has much inferior optical properties, which imposes severe constraints on the possible applications. Copper suffers from the same problems since Cu_2O and CuO also form readily, but received much less attention than the other noble metals in spite of encouraging results [82]. More recently, research on aluminum has gained a lot of momentum. The interband transition for aluminum lies below 200 nm wavelength, which allows excitation of plasmonic resonances down to UV wavelengths without increased losses. Applications like Fluorescence sensing [83]–[85] or UV lasing [86] can therefore strongly profit from aluminum. Also, aluminum is the third most abundant element on earth and therefore costs much less than the two noble metals. In contrast to silver, aluminum forms a self–protecting, native Al_2O_3 layer of a few nanometers. The major part of a typical aluminum nanostructure therefore remains pristine and the thin oxide only slightly modifies the optical response for most wavelengths [87].
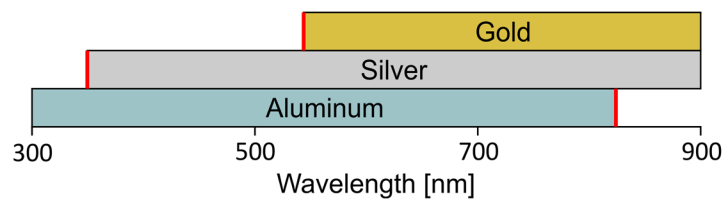
Figure 9. Eligibility of popular plasmonic materials for wavelengths around the visible range, the positions of notable interband transitions are marked red [88].

A final material that recently received a lot of attention for supporting plasmonic resonances is graphene. Graphene is a two dimensional sheet consisting of a hexagonal arrangement of carbon atoms. Although it technically is a zero bandgap semiconductor, this material exhibits metallic properties and surface plasmons can be excited in it. It further promises high electron mobility [89], [90] and unprecedented confinement of SPPs due to the two dimensional nature of the material [91], [92]. Another exciting property of graphene is the ability to electrostatically tune the plasmonic resonances [93], [94]. Graphene plasmonics is unfortunately limited to the mid infrared to Terahertz waveband and difficult to transfer to the visible. This shifts the focus of graphene based devices to applications like e.g. plasmonic circuitry, where low losses are of great importance [95]. Plasmonics in graphene is however a new and strongly growing field of research that has a lot of potential due to the fantastic intrinsic properties of this material.

2.2.4   Applications

Applications of plasmonics range from sensing over color effects to solar cell enhancement. Most applications rely on the strong near–field enhancement plasmonic nanostructures can generate in their vicinity. Color effects on the other hand profit from the sharp spectral features plasmonic resonances can create. Finally, the Ohmic losses occurring in the metal can also be turned into an advantage as they allow for strongly localized heating.

Structural colors

The origins of physical colors can be manifold, but are often related to periodic structures. This is also true for many iridescent colors found in nature like the wings of the famous morpho butterfly [5], [96] or chameleon scales [97]. Physical colors are preferred over chemical colors because they do not photobleach (the loss of color upon continued irradiation). This is a very important property for color filters used in research but also for any object used under daylight

illumination. Besides coloration of objects like e.g. cars or mobile phones, physical colors are particularly sought after for display filters and optical effects in the security and brand protec-protection industries (as discussed in Section 2.1.2). Systems capable of generating colorful effects are thin film interference [98], photonic crystals [22], nanoparticles [99]–[101], or metallic grating structures [102] to cite a few. Periodic plasmonic structures have generated a lot of interest as they can be tuned across the visible spectrum by changing e.g. the structure size or spacing [103]–[105]. As a result, with pixelization entire images can be "printed" in up–scalable ways [106]. In contrast to diffraction gratings, photonic crystals or thin films, plasmonic colors can be designed to be insensitive to the viewing angle [107]. Various geometries have been considered, each offering individual design parameters; a recent summary of the most popular approaches can be found in [108].

Transmissive plasmonic colors have also generated a lot of interest and were e.g. implemented in security features, which could be incorporated into polymeric banknotes [109]. More information on security features can be found in Section 2.1.2. A large share of the color filter research however targets display technologies and image sensors [110]. The requirements for such devices however are challenging: angle independence [111], high transparency [112] and narrow–band response are essential. Fano–resonances exhibit sharp spectral features, which are especially favorable for such applications and could therefore be a promising candidate for such applications. This type of resonance will be detailed in Section 5.1.2.

Sensing

Historically, surface plasmon resonance (SPR) sensing is one of the oldest applications intentionally using plasmons. Proves of concept for detecting the refractive indices of organic monolayers [113] and electrochemical interfaces [114] date back to the 1970s and 1980s. The sensing principle is thereby usually based on the angle–sensitive excitation of the SPP, which depends on the refractive index of the material interfacing it [73]. The most commonly used Kretschmann configuration is displayed in Figure 10, the sensing layer in purple hereby responds to stimuli with refractive index changes. A variety of events can cause such refractive index changes and are therefore monitored with this technique, the most popular being antigen/antibody reactions, biotin/streptavidin binding and oligonucleotides complementation [115]. Surface plasmon resonance sensors are commercially available and are popular for monitoring small sample volumes with low limits of detection (in the order of ng/ml [116], depending on analyte and solution) in real–time. Recently, gratings were also used for coupling the surface plasmons, which enables unique sensing mechanisms and higher packing density [117], [118], but also creates additional difficulties. A more complete overview of surface plasmon sensing can be found in the extensive literature existing on this topic [115], [119].
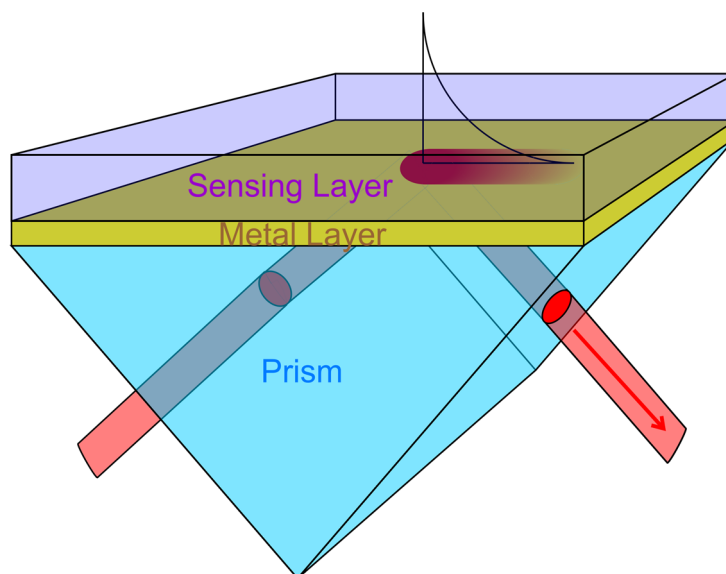
Figure 10. SPR sensing setup in Kretschmann configuration.

Besides this "classical" approach for plasmonic sensing, many other schemes have been proposed in the meantime. Techniques based on LSPRs in either periodic [120]–[123] or random nanoparticles [124]–[126] received a lot of attention since they promise strongly reducing the setup cost when compared to SPP sensors. The sensing principle though is similar: As visible in equation [2–3], the resonance position of particles depends on the permittivity of the surrounding medium ε_2. Any change of the refractive index will therefore lead to a shift of this resonance position. The main disadvantage is a strongly reduced sensitivity to refractive index changes outside of the closest 5–15 nm mantle around the metal particle, but on the other hand this technique can even work with smaller sample volumes than SPP sensors [127]. A comprehensive summary of LSPR sensing approaches can e.g. be found in [128], [129].

Finally, plasmonic structures were shown to strongly enhance Raman scattering signals, which resulted in the development of the surface enhanced Raman scattering (SERS) technique. Two enhancement paths exist: On the one hand, the strong near–field enhancement, which plasmonic substrates can provide, increases the interaction between the impinging radiation and the substance. On the other hand, general chemical interactions between the metal and the analyte also have a significant influence [130]. Nanoparticles [131] as well as periodic metal structures [16], [132] have proven to be effective substrates for this purpose. Enhancement factors of up to 10^{12} have been reported for ideal cases, which allows for single–molecule Raman spectroscopy [133].

Photovoltaics and catalysis

Photocatalysis and photovoltaics can profit from plasmonic resonances in a similar way. Two modes of action are conceivable: First, plasmonic resonances can enhance the interaction between the incoming light and the active material (be it a reactant or a semiconductor) by concentration of the radiation. The active material is thereby either loaded with nanoparticles [134] or it is placed at the hot spot of a plasmonic resonance [18]. A possibility to achieve the latter is e.g. placing it inside a plasmonic cavity [135] or close to an antenna [136]. In the same vein, surface plasmon polaritons can also "trap" the incoming light at an interface. Through this propagation, the interaction with the active material can be increased [12]. These configurations require careful design of the interfaces due to the resulting enhancement of surface

recombination rates [137]; but at the same time plasmonics has the potential to still represent a significant upgrade over direct patterning of the semiconductor in this regard [138].

The second route consists in the transfer of hot electrons and has become a very active field of research. The term hot electron describes an electron that possesses a higher energy than electrons thermally excited by the ambient. This can e.g. be achieved through excitation of an LSPR. Relaxation of these electrons is extremely fast in metals (picosecond range [139]), which means that they have to be extracted before they thermalize. Dye sensitized solar cells are based on such a principle where electrons are typically injected into TiO_2 [140]. It is therefore unsurprising that such systems are also very popular for hot carrier transfer from LSPRs. For Photocatalysis, many different reactions are under investigation, with water splitting at TiO_2 electrodes being the most noticeable amongst them [141]. Here, LSPRs can e.g. shift the photocatalytic reaction from UV into the visible [142], which paves a way to perform such processes with solar light. Finally, plasmonic resonances can also be used for scattering, comparable to the random photonic structures mentioned earlier. They are usually placed at the incident air interface of the device, since this configuration significantly enhances the transmissive over the reflective scattering due to the high difference in refractive index [17], [143].

Through plasmonic amplification, photovoltaics and photocatalysis could not only become more efficient, but also require lower amounts of active material. This is especially important for organic solar cells, where the material has to be kept thin due to low carrier diffusion lengths [144], and thin–film solar cells based on expensive semiconductors [12]. Plasmonic enhancement of these processes is still heavily investigated as the underlying processes are very complex and not fully understood to date, but reviews on photovoltaics as well as photocatalysis give a great overview on the state of the art [145].

Nanomedicine

Various applications in nanomedicine can strongly benefit from LSPRs. Metals (especially gold) have low chemical reactivity and are therefore believed to show low toxicity for the human body. As the size of the objects becomes smaller, this might not hold true anymore since they can e.g. diffuse between the cell walls or pass the blood–brain barrier [146]. Size dependent toxicity of such devices is therefore an important topic to be considered when designing plasmonic structures for in vivo applications. Gold nanoparticles are favorable for biological applications due to their low toxicity (they were even suggested as a benchmark for non–toxicity [147]). They further profit from the well–known functionalization chemistry with thiol–bonds, which e.g. also enables size control [148]. A simple application of such particles is signal enhancement of X–ray, fluorescence or optical microscopy techniques through the enhanced scattering of the incoming radiation [149]. With the proper biological functionalization, the particles are able to specifically attach to (and thereby stain) certain cell types or organs [150]. With this specific addressing of e.g. tumor cells with nanoparticles, exciting opportunities arise: By properly tuning the particle size, the corresponding resonance wavelength can e.g. be fit to the transparency window of mammals. This allows non–invasive energy transfer to specific targets through Ohmic heating associated with the LSPRs. In the case of cancer, the vision is to photo–thermally ablate the tumor cells without damaging the remaining tissue. Experiments on mice already showed positive results and hopes for real world applications are high [151]. Specific targeting of cancer cells can also be combined with drug release, which allows enhancing the efficiency of the substance [152]. An option here is site–specific, light stimulated

drug release through LSPRs. This allows mitigating side effects on other organs and accurate dosage of the medicine [153]. There are many other possible applications of plasmonic reso-resonances in medicine and a very thorough treatment of this topic can be found in a recent review [154]. Nanoparticles can take over different tasks in drug delivery and the possibility of integrating multiple functionalities into a single particle is what makes this field very exciting.

2.3   Colorimetry

Colorimetry aims to enable the "objective description of the physical correlates of color perception" [155]. This means it is a quantitative approach to the bases of human color sensation in contrast to spectroscopy, which only tries to determine spectral compositions. Therefore, after starting this chapter with a short historical perspective, I will quickly touch on the biology of human color perception and then transit to the color spaces introduced by the "Commission internationale de l'éclairage" (CIE). These spaces allow the calculation and representation of colors based on simulated or measured optical spectra. The relevant parameters for implementation of the simulations are finally discussed. Further information on colorimetry can be found in the comprehensive books this section is also based on [155], [156].

2.3.1   History

Colors and vision in general fascinated humanity since millennia as e.g. Greek philosophers such as Aristotle already wrote on this topic. Theoretical approaches to describe colors can be found in works of Leon Battista Alberti (1404–1472) and Leonardo da Vinci (1452–1519), but the actual starting point of color theory is generally assigned to Newton's "Opticks" printed in 1704 [157]. He described white light as a superposition of different hues and found that colors can be generated by mixing those hues. In the following, different color circles, spaces and other schemes were developed to asses this phenomenon for additive (e.g. light) as well as subtractive (e.g. paint) mixing of colors. One historical example of such a color circle (1855, including e.g. complementary colors) stemming from Michel–Eugène Chevreul is shown in Figure 11. These efforts mark the starting point of colorimetry, which has later been unified by the CIE.
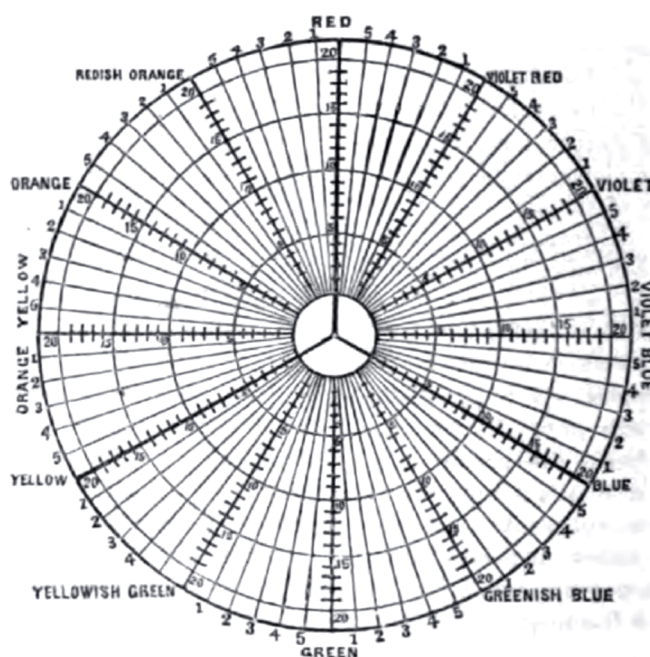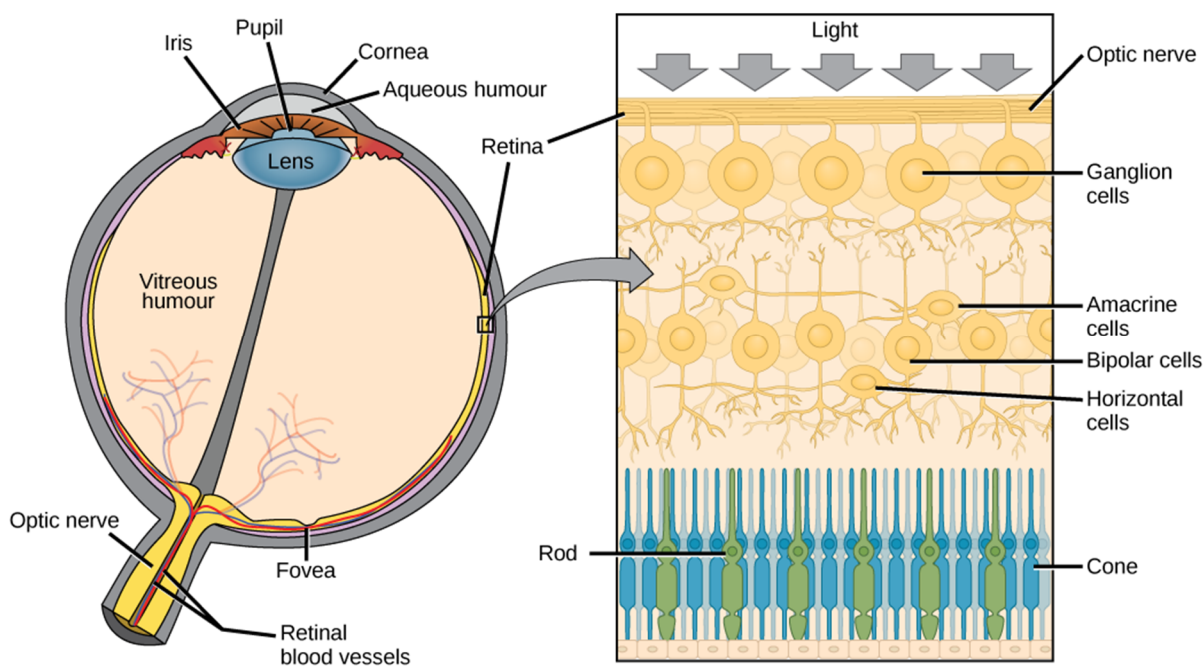

Figure 11. Chromatic diagram by Michel–Eugène Chevreul (1855) [158].

2.3.2   Human color vision

Figure 12. Schematic of the human eye highlighting the retina containing light sensitive rod and cone cells [159].

The retina of the human eye contains two different light sensitive cell types, the "rods" and "cones", named after their approximate shape (schematic shown in Figure 12). Rods are only able to distinguish between light and dark, but are much more sensitive to the light intensity. Cones on the other hand exist in three different varieties and each of them is stimulated by a different wavelength range of incident light; they are hence also called "S" (short), "M" (middle), and "L" (long wavelength) cones. The exact spectral response of each cell type is displayed in Figure 13 (a). These three cell types motivated the "trichromatic theory of color vision" by Young [160] and later Helmholtz, which subsequently served as a basis for the XYZ and RGB color spaces (Section 2.3.3). The spectral response of the cones though only shows one part of the color sensation taking place in the human eye: Part of the signal processing is already performed in specialized neurons in the retina.
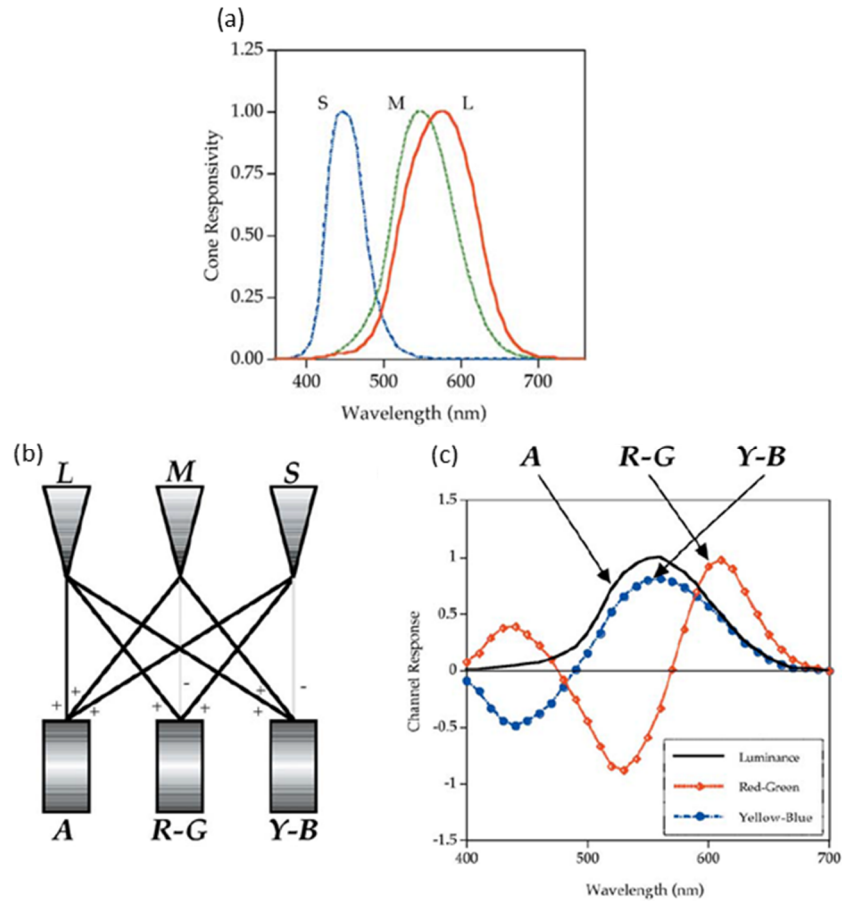
Figure 13. (a) Responsivity of the three different cone types, (b) signal processing taking place in the eye, (c) processed signal transmitted by each of the outgoing channels, adapted from M. Fairchild [156] © 2005 John Wiley & Sons Ltd.

The signals coming from the three different cones are thereby simply summed in one neuron (A), the difference between red and green is formed in a second one (R–G, long+short–middle wavelengths) and blue is subtracted from the yellow response in a final neuron (Y–B, long+middle–short) as illustrated in Figure 13 (b). The resulting output signals with respect to the incoming wavelength are shown in Figure 13 (c). This theory of preprocessing is called "Opponent colors theory", is attributed to Ewald Hering (also early 19th century) and was motivated by observations on e.g. the color pairs indiscernible by color blind people or the impossibility of seeing certain combinations of hues (reddish green or yellowish blue). Finally, the processed signals shown in Figure 13 (c) served as an important input to colorimetry as e.g. the CIE Lab system which is based on these opponent colors.

2.3.3   "Commission internationale de l'éclairage" (CIE)

The "Commission internationale de l'éclairage" (CIE) established in 1931 provides the to date best known approach to colorimetry. The basis of the CIE approach consists of four pieces (Figure 14): an illuminant (a), the measurement geometry (b), an observer (c) and a color space (d). CIE elaborated standards for the parametrization of each of the pieces, which will be discussed in the following.
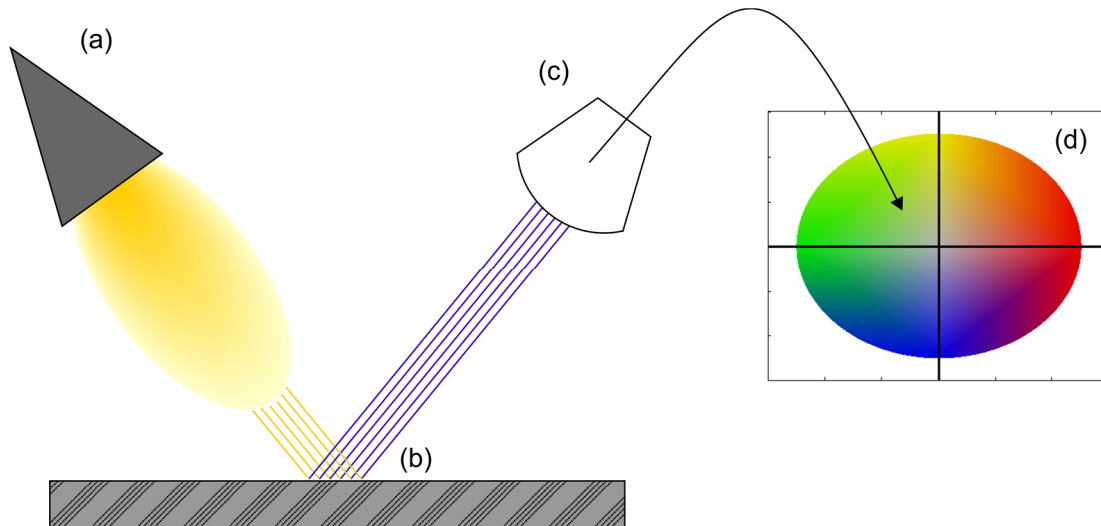
Figure 14. The parametrized and standardized components of colorimetry include (a) the illuminant, (b) the measurement geometry, (c) the observer and (d) the color space.
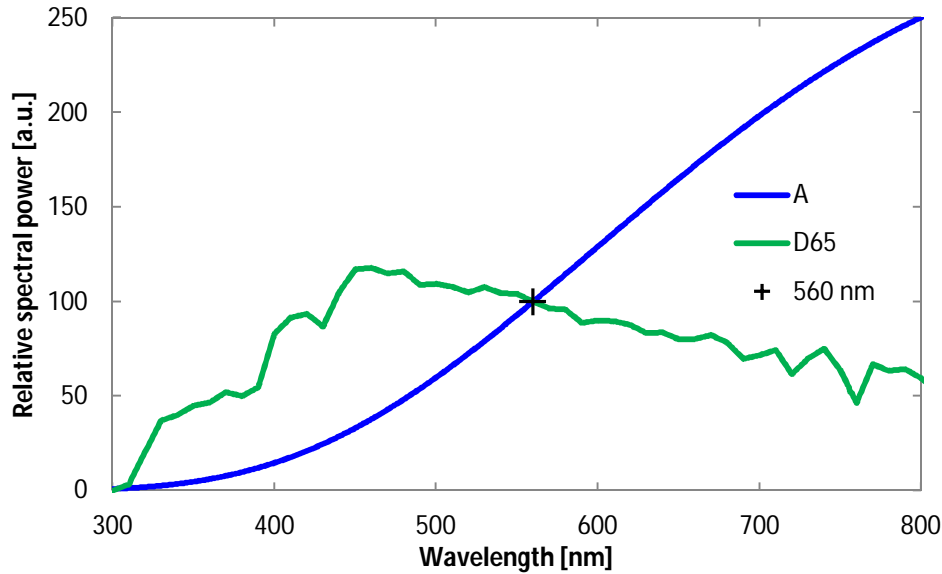
a) Illuminants

Illumination can have strong influence on the appearance of colors as we e.g. know from the different perception of clothes in a changing room when compared to ambient light. Important properties are directionality (diffuse vs. direct), overall intensity and spectral composition, whereas the latter is the most relevant one for the purposes of this thesis. CIE advocates using one of the two standard illuminants called A and D65 [161]. Illuminant A reproduces the spectrum of a tungsten filament light bulb and is approximated by a black body radiator of 2856 K ("color temperature") according to Planck's law. The resulting relative spectral power distribution $S_A(\lambda)$ as used in the CIE table is:

$$S_A(\lambda) = 100 \left(\frac{560}{\lambda}\right)^5 \frac{exp\left(\frac{1.435 * 10^7}{2848 * 560} - 1\right)}{exp\left(\frac{1.435 * 10^7}{2848\lambda} - 1\right)}. \qquad [2-4]$$

Illuminant D65 on the other hand corresponds to the average spectrum of the sunlight throughout the year for Europe ($S_{D65}(\lambda)$, which is close to a color temperature of 6500 K, hence the name). A graph containing those two illuminants is shown in Figure 15, the corresponding tabulated data can be found on the CIE website [162] or in various textbooks. Note the typical normalization to 100 at 560 nm wavelength (cross in Figure 15).

Figure 15. Graphs of illuminants A (blue) and D65 (green) are shown together with the normalization point at 560 nm wavelength (cross).

b) Geometry

CIE has set standards for the arrangement of illuminant, object under investigation and observer for measurements in either transmission or reflection. These standards comprise parameters like angle of incidence and handling of haze (directional vs. diffuse). The desired geometries however vary with the application, which makes it difficult to follow the standard. I indicated the parameters used in the corresponding chapters; haze is very low for the investigated structures and can thus be ignored. Reflectance $R(\lambda)$ and transmittance $T(\lambda)$ of the structures are determined through simulations (Section 3.4) and the output intensities $\phi(\lambda)$ are equal to $S(\lambda) R(\lambda)$ or $S(\lambda) T(\lambda)$ respectively.

c) Observers

The function of the observer is to transform a spectral power distribution into a visual response. This centerpiece of the CIE approach is still the standard today and relies on 3 color matching functions inspired by the trichromatic theory of color vision (called $\bar{x}(\lambda)$, $\bar{y}(\lambda)$ and $\bar{z}(\lambda)$, see Figure 16). Two standard observers are advised, CIE 1931 and CIE 1964. The principle behind both is the same but CIE 1931 should be used for a field of view below 4° and CIE 1964 for larger fields of view. The former is the case for my experiments and the CIE 1931 observer is therefore used. The corresponding color matching functions are given in Figure 16 (as available in the CIE downloads section). Mathematically, the response of each of these artificial cone cells is given by the convolution of the incoming spectral power distribution with its response function:

$$ X = \int_\lambda \phi(\lambda)\, \bar{x}(\lambda)\, d\lambda\,, \quad Y = \int_\lambda \phi(\lambda)\, \bar{y}(\lambda)\, d\lambda\,, \quad Z = \int_\lambda \phi(\lambda)\, \bar{z}(\lambda)\, d\lambda\,. \qquad [2\text{--}5] $$

Technically, there are infinite possibilities of defining such functions, but two deliberately chosen properties of the CIE observers are worth mentioning. First, no negative values occur, although they were part of the initial proposition [155]. Second and most importantly, the luminosity function (describing the sensitivity of the human retina to a flat spectrum) was chosen for $\bar{y}(\lambda)$. This stores a pure light/dark response in Y and decouples it from the hue.
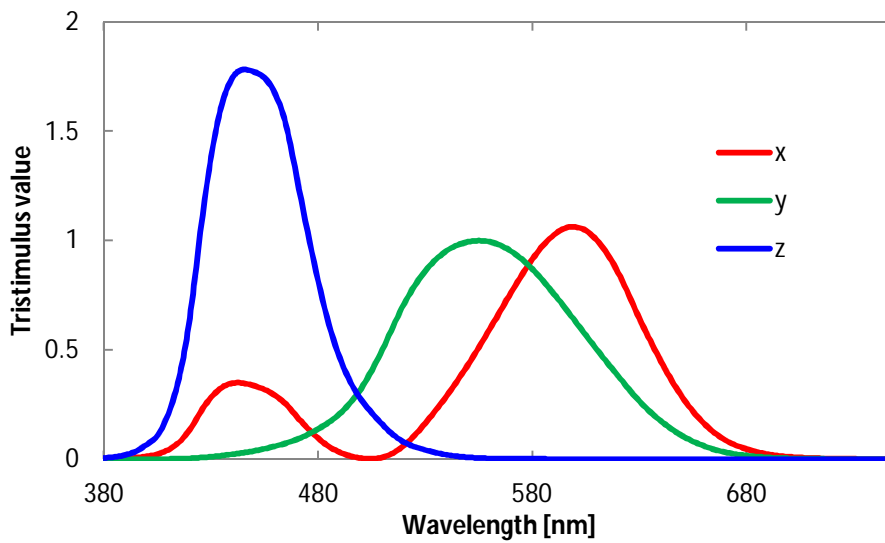
Figure 16. CIE 1931 color matching functions, $\bar{x}(\lambda)$ in red, $\bar{y}(\lambda)$ in green and $\bar{z}(\lambda)$ in blue.

d) Color systems

There exists a wide variety of color systems and covering all of them is beyond the scope of this thesis. I will focus on the most predominant systems in use, which are the *xyY* and standard red green blue (sRGB) color spaces. Information on the Lab/Luv system are not crucial to understand the work performed in this thesis but the knowledge provided is very important if the visual response of a sensor (as e.g. the strain sensor presented in Section 5.3) should be quantified and optimized. This could be a future goal in continuation of the work presented here.

Although the *XYZ* responses directly constitute a color space, it is more convenient to reduce the parameters to 2D. As *Y* only contains information on the lightness, hues can be represented using the following normalizations:

$$x = \frac{X}{X + Y + Z},\qquad\qquad\qquad\text{[2–6]}$$

$$y = \frac{Y}{X + Y + Z}.\qquad\qquad\qquad\text{[2–7]}$$

This color space is referred to as the CIE *xyY* color space. The initial tristimulus values can also be reconstructed by using the inverse transformation:

$$X = \frac{xY}{y},\qquad\qquad\qquad\text{[2–8]}$$

$$Z = \frac{(1 - x - y)Y}{y}.\qquad\qquad\qquad\text{[2–9]}$$

The *xyY* representation of colors allows for a 2 dimensional plot called the chromaticity diagram and Figure 17 shows the spectral locus of this space (maximally saturated colors). The white point can be found close to $(\frac{1}{3}, \frac{1}{3})$ where $X = Y = Z$ (Point "w" in Figure 17) and depends on the light source. The saturation gradually decreases when moving from the locus towards the white

point. There are some caveats associated with using the *xyY* color space, because it is not percep-perceptually uniform and does not take into account adaptation of e.g. the human eye to lasting stimulus, which also makes it a bad choice for comparing color gamuts of imaging devices [156]. Further, if the lightness *Y* is not provided, an uncommented *xy*–plot can lead to strong misconception about the actual stimulus (especially when additionally colored like e.g. the graph in Figure 17). But in the end, this representation allows for comparison between colored devices such as nanostructures at a glance and is therefore still heavily used [163].
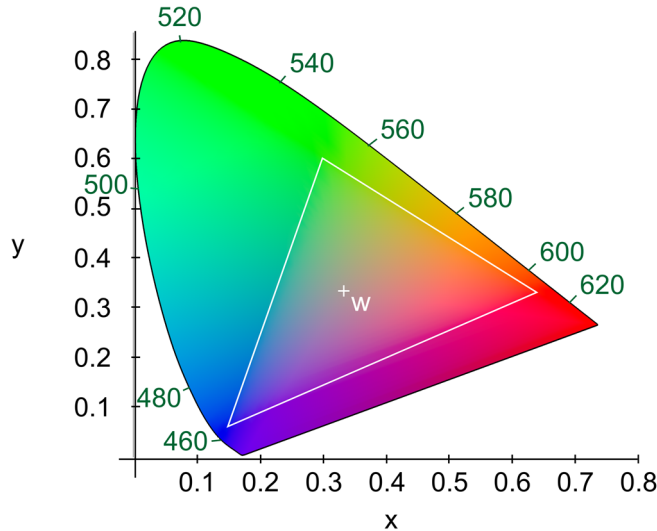
Figure 17. Chromaticity diagram including spectral color gamut, the white point (labelled "w") and the standard RGB color triangle created in Matlab.

It is worth noting that the colors on the straight line connecting 400 nm and 700 nm are not spectral colors but mixtures of blue and red hues. This mixing of distinct colors in order to obtain a variety of perceptually homogeneous hues (Grassmann's law) also applies to any point within a given locus and is an important concept that e.g. enables pixelation in display or printing applications. A standard computer screen e.g. uses three primary colors called sRGB, which constitutes the final color space relevant to this thesis. The sRGB space is much more limited than human color vision, as only hues lying within the white triangle visible in Figure 17 can be displayed. The colors shown in this figure therefore are also not accurate outside of the mentioned triangle, which makes this representation somewhat misleading. Mapping *XYZ* values to RGB can be done with a matrix multiplication (here for D65 as the reference white point [164]):

$$\begin{bmatrix} R \\ G \\ B \end{bmatrix} = \begin{bmatrix} 3.2410 & -1.5374 & -0.4986 \\ -0.9692 & 1.8760 & 0.0416 \\ 0.0556 & -0.2040 & 1.0570 \end{bmatrix} \begin{bmatrix} X \\ Y \\ Z \end{bmatrix}. \qquad [2\text{--}10]$$

For displaying the RGB colors e.g. on a computer screen, which is the main application of this space, the obtained data first need to be clipped. Only values between 0 and 1 are within the sRGB gamut as shown in Figure 17 and larger or smaller values need to be fitted to this range. Subsequently, the data are adapted to the gamma correction of the respective output device (nonlinear transformation that adjusts the brightness of the displayed colors to the human perception). These RGB values can e.g. be used to complement an *xy*–graph and show good approximations of the actual colors that can be expected. A comprehensive guidance to the RGB color space is available in reference [164]. Extensive literature exists on the implementation of

color spaces in MATLAB [165]; programs as well as data available from reference [166] provide another great starting point.

CIE Lab and CIE Luv finally are the two 3D color spaces introduced and advocated by CIE in 1976. Although they do not lend themselves as well for printed visualization as the chromaticity diagram, they do offer some key advantages. Most importantly, they are perceptually uniform which the CIE XYZ is not. This means that the Euclidean distance between two points can be used as a measure for the perceptual difference between the according colors. It therefore e.g. allows quantification of the response of a visual sensor.

Since both color spaces are based on the same principles, I will only discuss the CIE Lab space briefly as it has become the standard in the meantime. As mentioned in Section 2.3.2, they are based on the opponent color theory: The constituent values, L^*, a^* and b^* are corresponding to the lightness, the redness–greenness and the yellowness–blueness. They can be calculated from the *XYZ* values with:

$$L = 116\left(\frac{Y}{Y_n}\right)^{\frac{1}{3}} - 16\,, \qquad\qquad [2\text{--}11]$$

$$a^* = 500\left(\left(\frac{X}{X_n}\right)^{\frac{1}{3}} - \left(\frac{Y}{Y_n}\right)^{\frac{1}{3}}\right), \qquad\qquad [2\text{--}12]$$

$$b^* = 200\left(\left(\frac{Y}{Y_n}\right)^{\frac{1}{3}} - \left(\frac{Z}{Z_n}\right)^{\frac{1}{3}}\right). \qquad\qquad [2\text{--}13]$$

Those equations also immediately show the departure from the *XYZ* system in that they use normalization parameters X_n, Y_n and Z_n for a "reference white". This allows for correction of the effect that the human perception adapts to the colors of the incident light and/or surrounding objects.

Chapter 3   Materials and Methods

3.1   Fabrication of periodic nanostructures

This section will start by reviewing the most popular fabrication processes for photonic and plasmonic devices. Laser interference lithography will be introduced as the wafer–scale origination process of choice. Tooling and embossing techniques to replicate the fabricated originals will then be covered. I will then turn to physical vapor deposition, which is one of the most popular coating processes in physics, but still a subject of debate. Especially in the context of plasmonics, the importance of this process is underappreciated and the important parameters will therefore be discussed. It is important to note that the fabrication process played a pivotal role in this thesis: Most of the techniques used in academia are limited to sub–centimeter sizes and therefore not suitable for industrial production. Development of up–scalable processes was therefore crucial for this thesis, but also constrained the design space heavily. The structures fabricated under these restrictions will be seen in Chapter 4 and Chapter 5, where the results will be discussed. The detailed parameters for the processes will also be given in the corresponding chapters for the sake of clarity.

3.1.1   Lithographic techniques

The product of Lithographic processes can either directly be the final device or then serve as a template for replication (Section 3.1.3). Lithography consists of three main steps: Resist patterning, Evaporation and/or Etching and resist stripping. Plasmonic nanostructures are often fabricated with a so called lift–off process, outlined in Figure 18 (a1) to (a3). The patterned photoresist covers part of a substrate (a1) and acts as a mask for the subsequent evaporation process at normal incidence (a2). After dissolving the photoresist, the metallic pattern is left behind on top of the substrate. The etching based process sketched in Figure 18 (b1)–(b3) is particularly useful if the pattern should be transferred into a homogeneous, durable material like e.g. quartz or silicon as a surface relief. Here, the (metallized) photoresist acts as a hardmask for an etching step (b2). Depending on the material and (etching) process, various shapes can be obtained. High quality gratings or photonic crystals are often fabricated in this manner, but such surface reliefs are also crucial for replication processes as will be shown in Section 3.1.3. It is worth noting at this point, that lithographic processes are high–throughput when considered in the context of semiconductor industry, but slow and expensive when compared to roll–to–roll embossing. It is therefore clear that this thesis aims to use such techniques only for the fabrication of grating originals, which then serve as masters for replication tools. Especially the size of the patterned surface area is crucial for this purpose, but price and feature size also play a role. Choice of the proper resist patterning process has a great influence on these parameters and I will therefore quickly review the most popular methods.
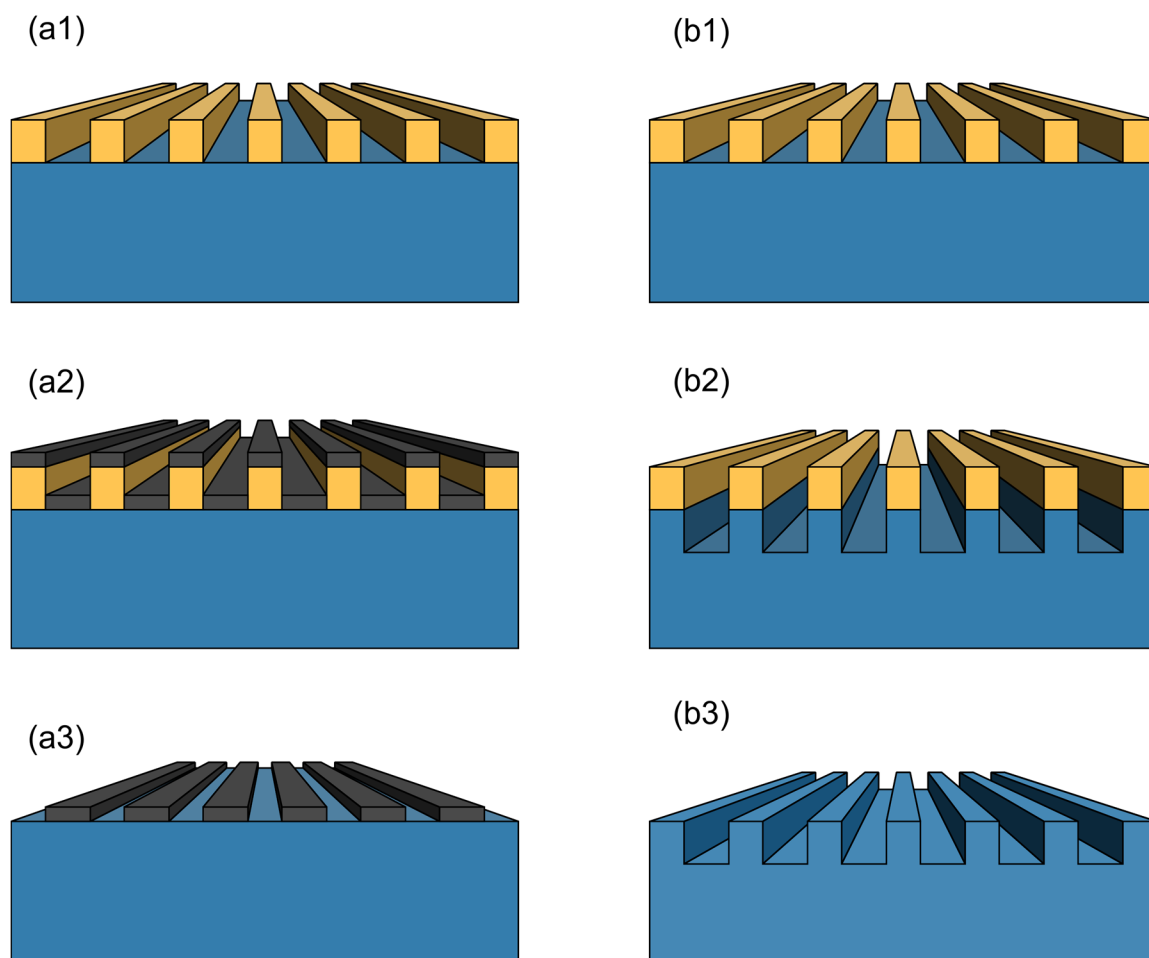
Figure 18. Examples of lithographic processes including (a1)–(a3) evaporation or (b1)–(b3) etching steps.

Patterning techniques can be divided into serial and parallel processes. In general, serial processes are more flexible but operate at a much lower patterning speed, which limits them to sample sizes in the centimeter regime. It is therefore not surprising that these processes are popular in academia and for proof–of–concept devices, but not suitable for industrial production. E–beam lithography (EBL) is the most popular amongst them for photonics research. It relies on scanning a focused electron beam across a photoresist in order to pattern it. The process is well–established, capable of generating structures with sub 10 nm resolution and allows for very flexible design in two dimensions [167]. Techniques sharing similar properties are most of the focused ion beam (FIB) methods, which use charged ions instead of electrons. An advantage of these methods is the increased choice of suitable substrates: since ion bombardment can etch patterns into virtually any material, no resist is required [168]. Although etching processes in general would allow using the resulting structures as templates for replication, lift–off processes seem to be more popular in plasmonics research. The latter is more convenient for creating disconnected nanostructures, as it e.g. allows for reduced dimensionality (2D instead of 3D), but becomes much more time consuming if large quantities are required.

The best known parallel process is photolithography. Here, a photoresist is cured by flood exposure through a photomask. Since photomasks are relatively easy to produce for feature sizes down to the micron regime, photolithography is very popular for rapid prototyping of structures above the diffraction limit. Photolithography has also been the standard process for

producing integrated circuits for a long time. The size limit imposed by light diffraction has however become increasingly problematic and alternative parallel techniques have been sought after, but none of them could outperform advanced photolithographic techniques that have been developed in the meantime (lab scale approaches reach feature sizes down to 15 nm [169]). The most popular alternative in photonics is nanoimprint lithography (NIL) [170]. Here, a resist is patterned by embossing it with a surface relief structure (e.g. by utilizing one of the replication processes discussed in Section 3.1.3). The prerequisite of a replication master mostly limits the applications of NIL to the fabrication of final products and not templates. The structure size here can theoretically be smaller than in photolithography since the patterning process is mainly limited by the molecular properties of the resist. An important problem with NIL is that, after imprinting, a small layer of resist will remain even in the recessed regions. An additional etching step is therefore required in order to remove this residue and access the substrate. Note that sometimes, simple embossing processes are also referred to as NIL, which I will refrain from doing. The resist patterning part of NIL is fully roll–to–roll compatible, but the etching and resist stripping steps are much more challenging to implement.
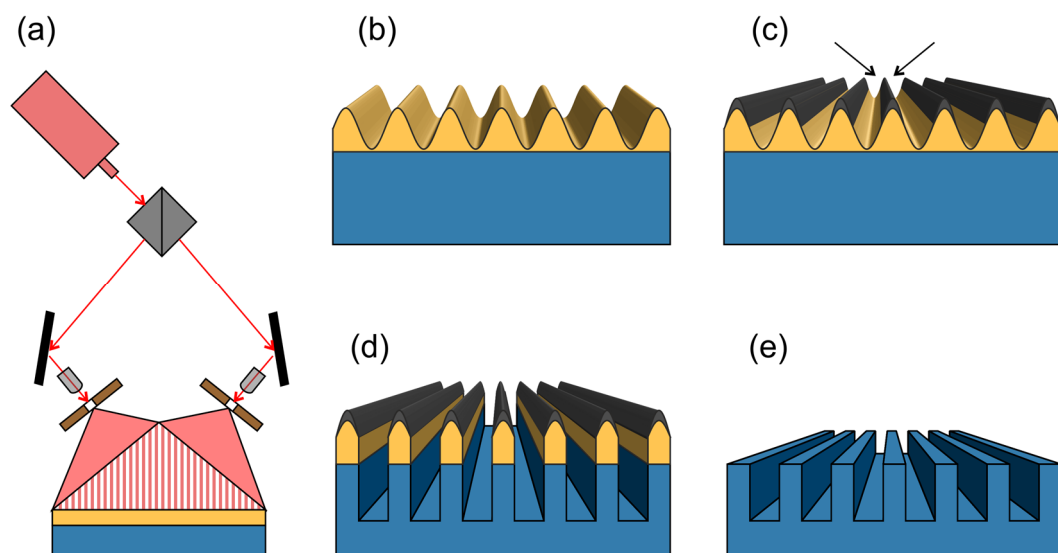
Figure 19. (a) A schematic of the laser interference setup is shown together with the following lithographic process for generating binary gratings: (b) the photoresist (orange) is developed and (c) metallized (black) before (d) an etching process transfers the pattern into the substrate (blue) and (e) the resist is lifted.

The parallel process of choice for this thesis is laser interference lithography (LIL). The setup for this patterning method is shown in Figure 19 (a). A laser beam is thereby split (beam splitter, shown in grey) and, after being reflected by mirrors (black), focused through pinholes (brown). The expanded beam then interferes with itself and, due to the coherence of the laser radiation, standing waves will form. These standing waves can be used to expose a photoresist (orange) and after development, a periodic sinus pattern can for example be recovered (Figure 19 (b)). This pattern can either directly be used for replication, or then be etched into the substrate: Usually, an additional protective layer is applied (e.g. by evaporating from both sides, Figure 19 (c)) and after removing the unprotected photoresist with reactive ion etching, the binary pattern is transferred into the substrate with ion beam milling (Figure 19 (d)). A binary grating can finally be obtained after lift–off (Figure 19 (e)). The evaporation angle determines the width of the ridges and therefore the duty cycle dc (ridge width divided by the grating period) of the resulting grating. The etching time finally determines the depth of the trenches. Dry etching at

normal incidence is used for binary gratings, but the same process performed at an oblique an-angle would yield slanted gratings [171]. When working with silicon, proper orientation of the crystal planes during wet etching can be used to create various other shapes like for example triangular trenches. LIL allows for close to m^2 size generation of periodic nanostructures in a single exposure [13]. The possibility of rotating and re–exposing the same resist several times also provides access to two–dimensional structures. The patterns available with laser interference are restricted though, which is the main downside of this technique. Another issue is the limitation of the feature size due to the wavelength of the laser. Periods down to 250 nm are readily achieved with the above setup and a 441.6 nm He–Cd laser, which is sufficient for all the work presented in this thesis. For deeper subwavelength structures, a shorter wavelength laser (which requires costly UV compatible equipment) or immersed holography could be used.

Colloidal or nanosphere lithography is another technique suited for parallel, wafer–size patterning that is based on the self–assembly of nano–beads [172]. Subsequently, shapes varying from nanodisks [173] over (split–) rings [174] to triangles [175] can be generated using different evaporation and etching steps. Assembling nano–beads on each product is clearly not profitable; creating a replication tool by etching the nano–bead pattern into the substrate on the other hand could be interesting for up–scalable processes but is rarely reported. A major drawback of the self–assembly technique in general is the small size of the individual crystalline areas ($100 \mu m^2$ range [172]), which introduces inhomogeneity on the wafer–scale. Target applications therefore mainly include scattering and anti–reflection layers for optical components or effects based on the response of individual plasmonic structures, where long–range ordering is not important.

An excellent overview on nanofabrication techniques for plasmonics is available from Lindquist *et al.* [168].

3.1.2   Physical vapor deposition (PVD)

Physical vapor deposition is the most popular metallization process for plasmonics as has been mentioned in the previous section. High quality metal layers are required for these applications and defects as well as granularity in the metal layers can lead to increased losses or scattering in the material. Here, I therefore intend to first discuss this defining process in a broader sense by identifying the important parameters and showing their influence.

Physical vapor deposition (PVD) is the deposition of material on a substrate in the absence of reactive gases. A source of the desired material is thus either heated resistively (thermal evaporations) or bombarded with inert ions/electrons (sputtering/e–beam evaporation) to transfer an adjustable amount of it to the sample and subsequently condensate it there. The atmosphere under which this process is performed thereby significantly influences the free path length (the distance between scattering events due to the residual gas) and thus the shape and quality of the resulting film. High vacuum conditions (preferably below $\approx 10^{-4}$ Pa/10^{-1} mbar) are commonly used for the fabrication of plasmonic nanostructures: residual gas molecules (especially water and O_2) have a strongly detrimental effect on the optical properties of the deposited metal. They can adsorb to the growing surface and pin grain–boundaries, which will cause increased electrical losses in the final metal film [176]. The increased path length at low pressures (a multiple of the chamber length) further allows for directional deposition of material, since only a very small fraction of the emitted metal gas is scattered before reaching the substrate. In the case of perpendicular evaporation at a grating, disconnected wires form on

the ridges as well as on the bottom of the grating (Figure 20 (a)). By changing the angle of inci-dence, the ridges start to shadow the trenches and different shapes can be obtained (Figure 21). This oblique deposition technique, also called shadow or angle/angular evaporation, is the core process used in this thesis. On the one hand, disconnected metal structures allow excitation of LSPRs (Chapter 5), which is not possible with continuous metal films. Furthermore, asymmetric coatings also introduce an asymmetric refractive index, which is interesting for diffractive appli-cations (Chapter 4). Oblique deposition therefore has the potential to become an important link between academic research and industry.
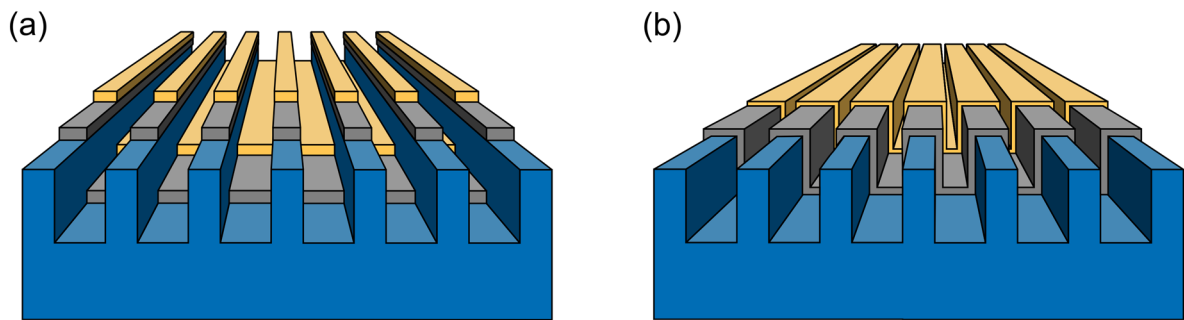
Figure 20. (a) Disconnected structures as obtained in a vacuum evaporation process and (b) conformal layers as would result from sputtering or short–distance evaporation are sketched.

Important geometrical parameters for directional evaporation (besides the evaporation angle) are the source–substrate distance and the respective sizes of the crucible as well as the sample. If the distance is large and the objects are small in comparison, simple geometrical considerations allow prediction of the resulting shape. Figure 21 (a) illustrates this situation and the resulting L–shaped, disconnected wires. For smaller distances, the angle of incidence will not be as well defined anymore and shadowing becomes imperfect (Figure 21 (b)). The decreased chamber size can even cause the far side of the sample to be coated (illustrated by the red dashed line), which will connect the structures. This is not particularly problematic when working with dielectrics and just needs to be kept in mind in the designing phase. When fabricating plasmonic devices however, the connection will cancel the confinement of the electrons and thereby destroy the resonance. Also, a thickness gradient is typically observed across the sample since the source gas concentration decreases for the distant parts of the substrate. Note that also for perpendicular incidence, the same issues can occur (Figure 20 (b) illustrates the possible connections between the wires).
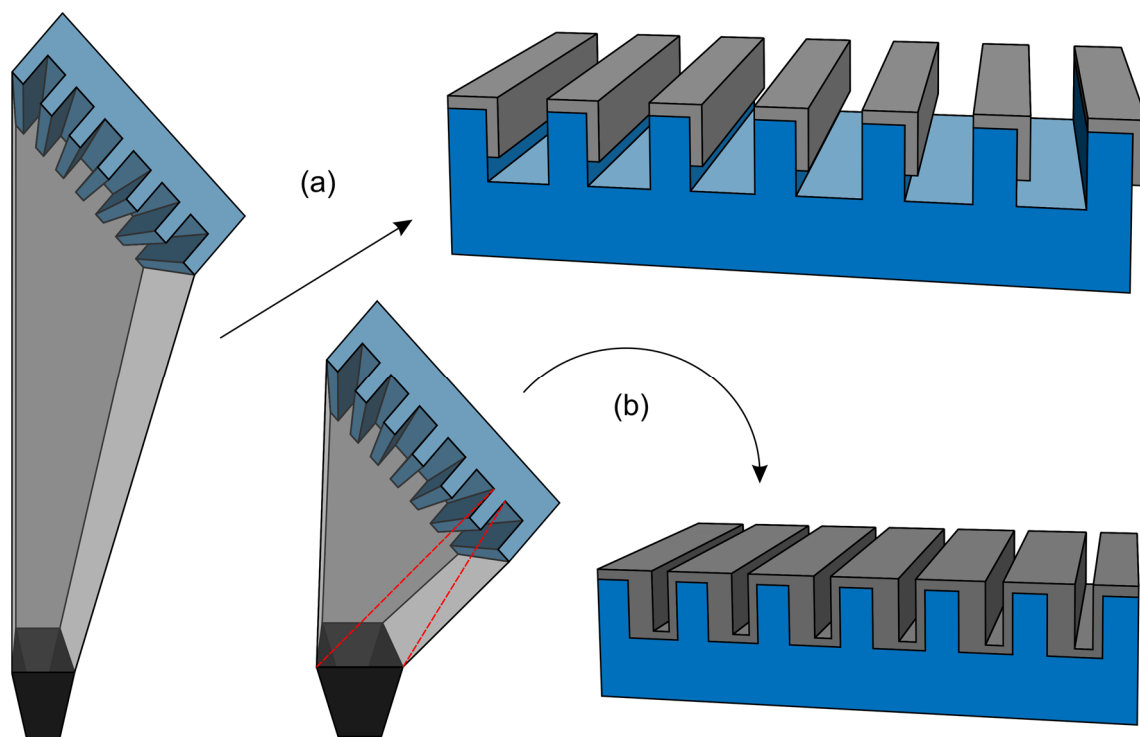
Figure 21. Schemes of the oblique angle deposition setup and the resulting coatings (a) for a large distance between the crucible and the sample and (b) for a small distance between the two are shown.

Another important parameter is the evaporation rate. It has been known for a long time, that fast rates e.g. help reducing the oxide content in the deposited films when working with reactive materials like aluminum [177]. Due to the grain–boundary pinning mentioned earlier, fast evaporation can however also help improving the film quality when evaporating less reactive materials like e.g. coinage metals. In a sense, fast evaporation can therefore be used to counteract suboptimal vacuum conditions (e.g. pressures above 10^{-6} mbar for Al) [176]. It is finally important to note that the evaporation rate has a strong influence on the heat transfer and dissipation in the substrate. Although it seems counterintuitive at first, high rates heat the sample less than low rates [176]. This property was especially important for the polyurethane fabrication process, as low rates caused melting of the grating ridges and thereby visible scattering. Finally, a popular approach to reduce granularity and increase adhesion is the evaporation of a very thin seed layer (1–10 nm, for example Cr or Ti [178]) below the actual metal layer. A major drawback of such techniques is that these layers often cause the plasmonic properties of the structure to deteriorate.

So–called sputter deposition of material finally requires the presence an inert gas (often argon) in the deposition chamber, which is ionized and accelerated towards the source to eject atoms. The gas at the same time acts as a scattering medium for the freed atoms, sending them on a random walk until they either adhere to the substrate or the chamber wall. The resulting coating is therefore continuous and conformal by design (Figure 20 (b)). This process is rarely used in plasmonics since the residual gas can have a negative influence on the optical properties of the deposited metal. Also, disconnected structures are often preferred and they are much easier to accomplish with evaporation processes.

3.1.3   Replication techniques

Low−cost and high−throughput processes capable of transferring patterns from a template into inexpensive materials are of paramount importance for mass−production. The most popular substrate materials include thermoformable or UV−curable polymers. Processes that are capable of transferring surface reliefs into such plastics are usually termed embossing, molding or imprinting. In this section, the basics of replication processes are presented together with the transfer of these nanostructures into metals. Deposition of thick metal layers (more than 100 nm, possibly up to several millimeters) on nanostructures and subsequent peeling can be used for manufacturing industrial replication tools, but also exhibits favorable optical properties for plasmonics. Many different replication methods exist for metals as well as polymers and I will only highlight some of the most popular ones in the following.

I will discuss two techniques capable of transferring nanostructures into metallic substrates, which both start with the evaporation of a metal film on a surface relief. A first process called electroplating or galvanic growth can be used to fabricate several millimeters thick metal shims. In this process shown in Figure 22 (a), the metallized master and a nickel plate are electrically contacted and immersed in a bath. The solution contains anions, which help transporting the positively charged metal cations to the grating. After growing an up to several millimeters thick metal layer, the freshly manufactured shim can be peeled off the template. Nickel shims are popular embossing masters, since this material is relatively hard and durable, but it is also flexible enough so that it can be bent around the cylinders e.g. used for roll−to−roll processes [179]. Nickel mold inserts can also be used for injection molding [180]. Nickel masters were also used in this thesis for all the embossing procedures. Note that many different materials like polymeric replicas or nickel masters themselves can be used as templates for electroplating. Step−and−repeat replication (Section 3.1.4) can therefore be used to create large−area mold masters from a smaller single structure. It is also possible to replicate surface holograms and create a mold master of the replica, which is a major issue for the security industry (Section 2.1.2).

Instead of creating thick, metallic masters, it is also possible to only transfer the evaporated thin film with a process called template stripping. This process relies on curing a polymer such as PDMS on top of the coated template and subsequently peeling it (Figure 22 (b)) [181]. When properly choosing the materials, the metal film will release from the template and only adhere to the polymer. The stripped metal surface is much smoother than a typical metal/air interface created through direct evaporation [182], which helps minimizing scattering and electrical losses. The metal films are unfortunately susceptible to rupture in the peeling process and therefore not yet suited for up−scalable production. Ablation of the template and the restriction to specific material combinations are other concerns. In principle though, the process could become roll−to−roll compatible, which makes it an interesting future candidate for high−throughput fabrication of high−quality plasmonic surfaces. In this thesis, template stripping was however only used to characterize the metal structures deposited on the stretchable polyurethane. Ormocer was thereby used to remove the metal from the elastomer, which allows the subsequent breaking and SEM measurement of the cross section.

(a)

(b)
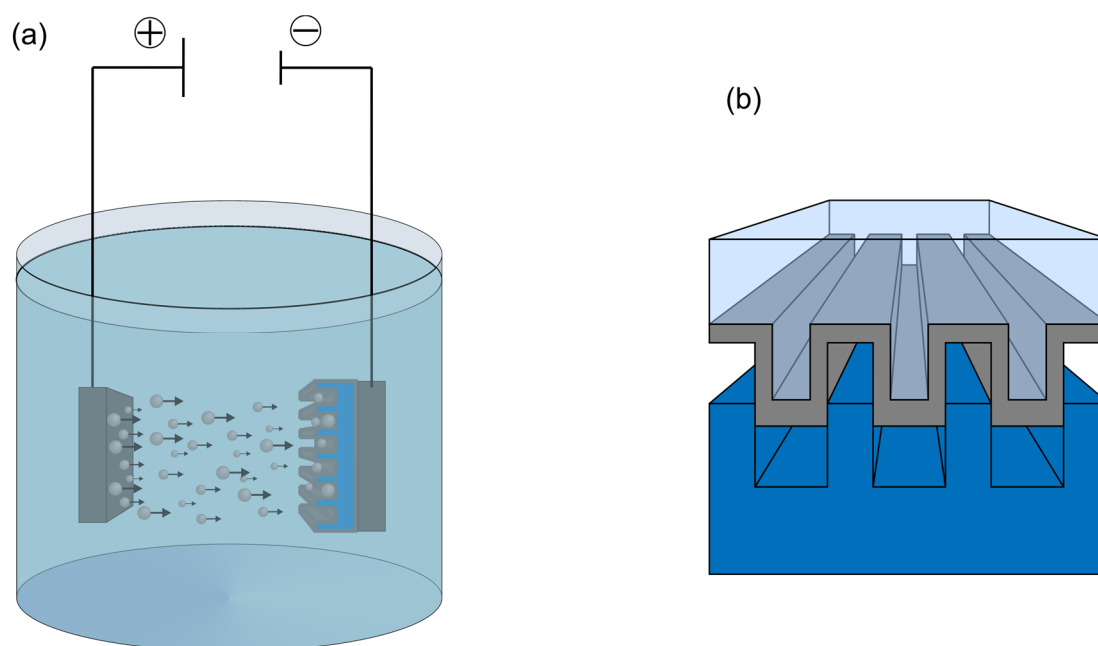
Figure 22. Transfer of nanostructures into metals: (a) the electroplating process involves the electrolytic deposition of metal ions on a template, whereas (b) template stripping relies on the adhesion/release of metal films.

Two of the most popular replication processes for patterning polymers are hot embossing and UV embossing. Hot embossing is, simply spoken, the act of pressing a hot tool into a molten piece of plastic (Figure 23 (a)). More technically, a polymer is heated above its glass transition temperature T_G and subsequently embossed with a heated master by applying a high pressure. After cooling the parts below T_G, they are separated and the cycle can be repeated on a new substrate. There are however plenty of parameters to consider for optimizing the process; anything from material choices over surface treatment down to temperature or force settings can significantly influence the final product properties and the replication fidelity. Typical polymers used for hot embossing include Polycarbonate (PC), Polymethylmethacrylate (PMMA), Polytetrafluoroethylene (PTFE) or Polyethylene terephthalate (PET). In this thesis, elastomeric Polyurethane (PU) and Polycarbonate (PC) were used. PC is flexible, wear-resistant and has a high T_G, which enables evaporation without compromising the grating. PU on the other hand can be elongated by more than 400% before breaking and is therefore ideal for applications in strain sensing (5.3).
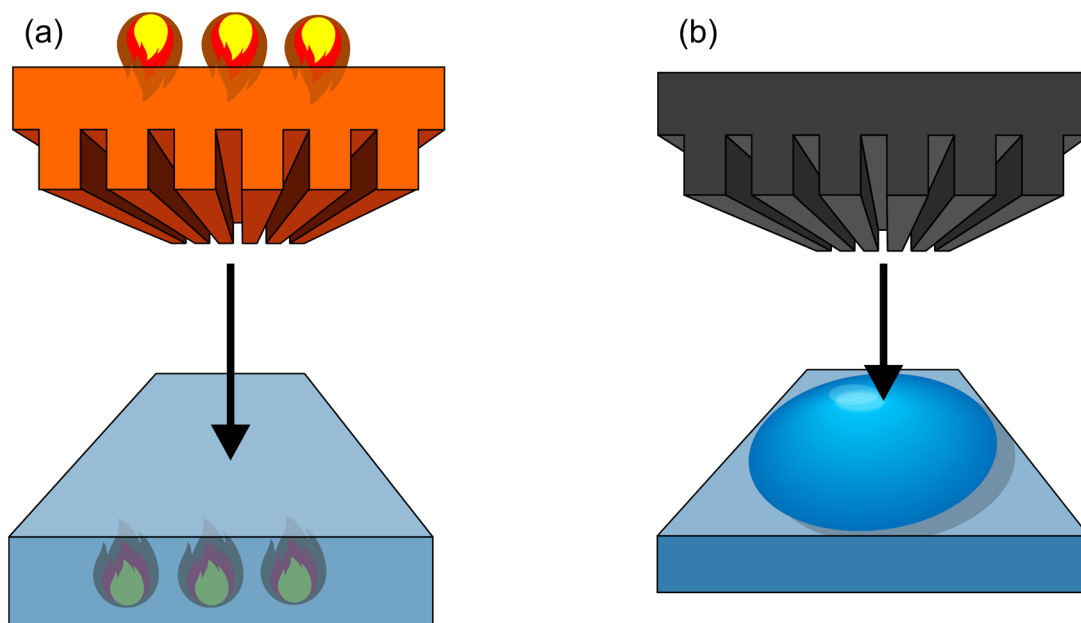
Figure 23. (a) Hot embossing process, where a hot tool (orange) is pressed into a molten polymer sheet (blue) and (b) the UV casting process, which relies on the patterning of a UV curable resin (blue droplet).

UV embossing (also called UV casting or UV imprinting) is similar to hot embossing. Instead of forming molten plastic, here, a liquid mixture of polymer precursors is shaped with the mold (Figure 23 (b)). UV light is then used to cure the polymer before removing the mold. UV casting hence relies on UV linkable monomers, which are more difficult to formulate and therefore also more expensive than thermoformable plastics. Yet, there is a large choice of commercially available UV curable materials like epoxies, polyurethanes, PDMS or Ormocers. For the present thesis, Ormocers are chosen when a rigid and heat resistant material is required. Otherwise, various fluorinated polymers are used due to their hydrophobicity and low viscosity, which is convenient for liquid handling and demolding. PDMS also has great physical properties in its cured state (flexible, stretchable, hydrophobic), but bears an increased risk of contaminating work spaces and vacuum chambers with uncured precursors. In this thesis, PDMS was therefore only used for covering processed devices and protecting them from wear. Note that it is also possible to use (printed) masks to combine UV embossing with photolithography (Figure 24). This technique allows macroscopically shaping the nanostructured areas and was used in this thesis for highlighting color effects. A drawback of UV curable materials is that they tend to remain absorptive at short wavelengths also after curing.

In terms of tool materials, UV casting offers more freedom than hot embossing, since the pressure and temperature the template needs to withstand is much lower (ambient conditions). Besides nickel shims and silicon/glass, UV embossing can therefore also utilize polymers as templates. Favorable properties like flexibility (e.g. PDMS) or anti–adhesion (e.g. PTFE), which would otherwise require a specific coating, can therefore be intrinsic to the embossing masters. For the same reason, it is also much easier to pattern fragile substrates like glass with UV curable resins.
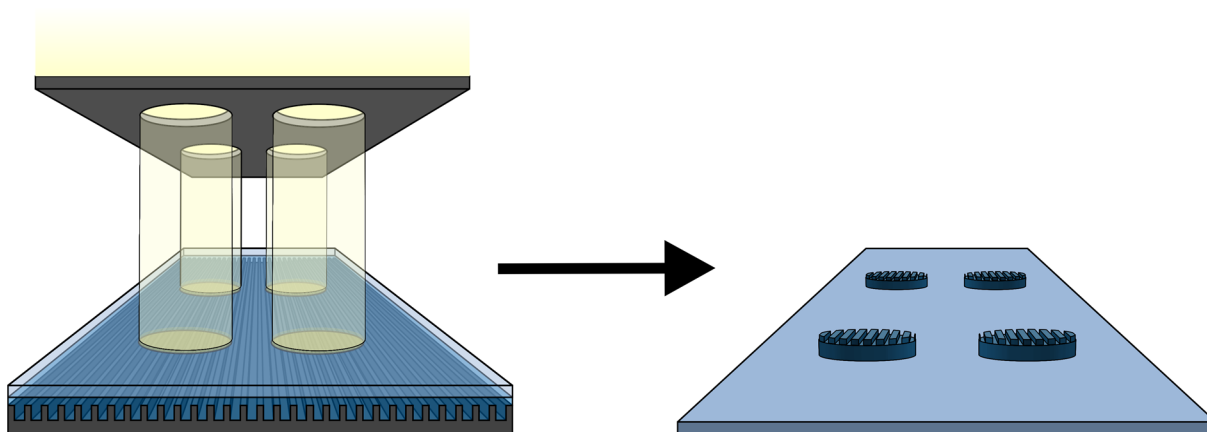
Figure 24. The combined UV embossing/photolithographic process is shown, where the resin is exposed through a mask to shape the nanostructures on a macroscopic level.

A general problem with these replication processes is demolding, which is especially problematic for high aspect ratio structures (structures that are much higher than wide, aspect ratio=height/width). Such features exhibit strongly increased adhesive forces and leave behind fragile structures that are either prone to breaking when removing the mold or, for example in the case of soft materials like PDMS, tend to collapse. To a certain extent, application of an anti–adhesive layer to the template can provide amendment to the former problem, but this technique is only reluctantly used on an industrial production level. I therefore limited myself to structures with aspect ratios below 2 in the present thesis, which should be applicable to roll–to–roll procedures.

3.1.4   Up–scaling the processes

Two important processes for large–scale reproduction of nanostructures are step–and–repeat replication and roll–to–roll manufacturing. Step–and–repeat replication is applied for the patterning of large substrates through multiple replications with the same master. The step–and–repeat process is often performed by subsequent hot or UV embossing steps. Many reproductions of a freestanding structure can readily be achieved with this procedure; it is however still not possible to assemble structures like e.g. gratings continuously due to the challenging alignment requirements ("stitching effects" are inevitable at the joints). An important application of this technique is the preparation of large area templates for roll–to–roll replication masters (e.g. with electroplating, previous section).
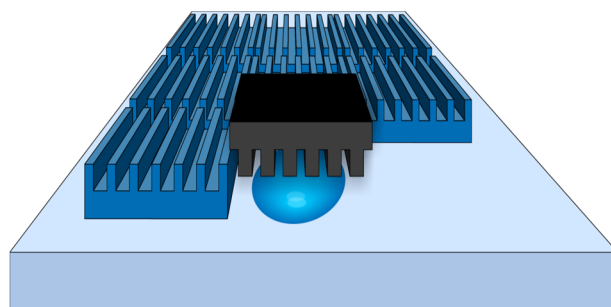
Figure 25. Drawing of the Step–and–repeat replication process.

Roll–to–roll manufacturing can also either be based on hot embossing (Figure 26 (a)) [183] or UV/heat curing (Figure 26 (b)) [184]. In contrast to the lab–scale counterpart, the replication here takes place on the curved surface of a roll. This curved surface can either be structured

directly or a shim can be tightly wrapped around the roll. The second option can lead to some problems like e.g. discontinuous patterning, but is significantly less expensive. For hot emboss-embossing, such shims are usually made of nickel, for UV roll–to–roll processes PTFE and ETFE are becoming increasingly popular for their anti–adhesive properties [185].
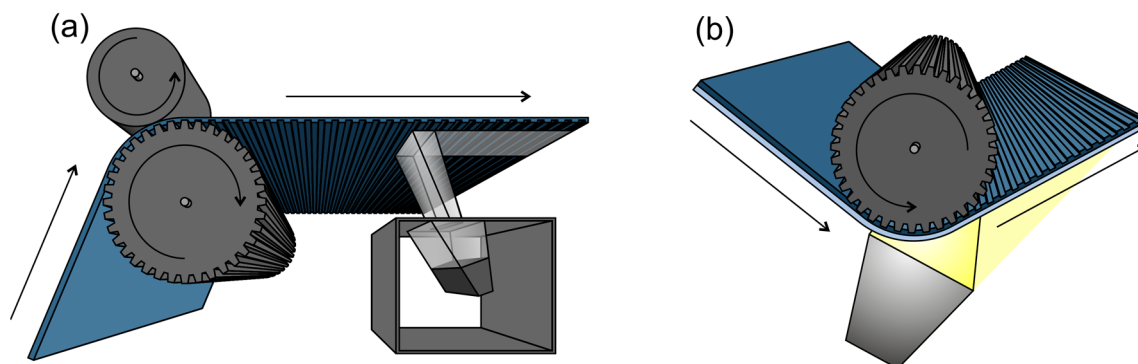
Figure 26. (a) Illustrations of the roll–to–roll hot embossing and evaporation as well as (b) UV casting procedures.

Physical vapor deposition is also a roll–to–roll suitable process [184]. Figure 26 (a) shows how an oblique evaporation process could schematically look like: A source is shielded with a baffle and the relative positions of shield, crucible and foil then determine at which angle the evaporated material is deposited. Oblique deposition has not been very popular for roll–to–roll processes recently, but was successfully applied in the magnet–band industry decades ago [186]; the present lab approach should therefore be compatible with mass production techniques. Note that stencil evaporation, which is the deposition of material through a hole mask, is in contrast expensive and also not suitable for roll–to–roll production due to clogging [187]. It is therefore intricate to achieve areas with different metal thicknesses or evaporation angles on a single object. For this reason, constant metallization parameters were used for the individual devices fabricated or proposed in the present thesis.

A final very important type of replication process is injection molding. This process utilizes a mold (usually steel, but nickel inserts are also common) into which molten material can be injected at high pressures. After cooling the molten mass and solidifying it, the mold is opened and the replicated part ejected. Injection molding is a high–throughput technique that is capable of structuring materials in 3D with sub–micron resolution [188]. Injection molding unfortunately cannot be directly combined with controlled material deposition techniques like e.g. evaporation.

3.2 Spectrophotometry

3.2.1 Spectrally resolved T1 measurement

A custom measurement setup was built to spectrally resolve the measured diffraction efficiencies. Recall that all non–zero orders are dispersive, meaning that each wavelength is diffracted at a different angle. Additionally, some of those angles can be larger than the total internal reflection angle (TIR) for the medium the ray is diffracted into. In the common case of a surface grating on a glass or polymer slab, all the wavelengths larger than the grating period ($\lambda > \Lambda$) are reflected at the back side of the sample and cannot be measured in a simple manner (compare to Section 2.1.1. and equation [2–2]).

One possible solution mentioned in literature is the use of lasers with different wavelengths, which can be coupled out with a triangular prism [36], [189]. Once the monochromatic beam is outcoupled, its intensity can even be measured with a simple photodiode. By comparing it to the initial beam intensity, the portion diffracted into the according order can be calculated. This method however only yields a few measurement points and not a complete spectrum. For this reason, I used an adapted version of the setup, which is capable of working under white light illumination. A half cylindrical lens with a radius approximately equal to its own thickness plus the one of the sample was bonded to the backside of the substrate using index matching fluid (Newport Corporation, F–IMF–105). The lens was fixed in vertical position and the grating was then oriented with its lines parallel to the cylinder axis. This allows all the orders to impinge perpendicularly onto the surface of the lens (see Figure 27 (a)).
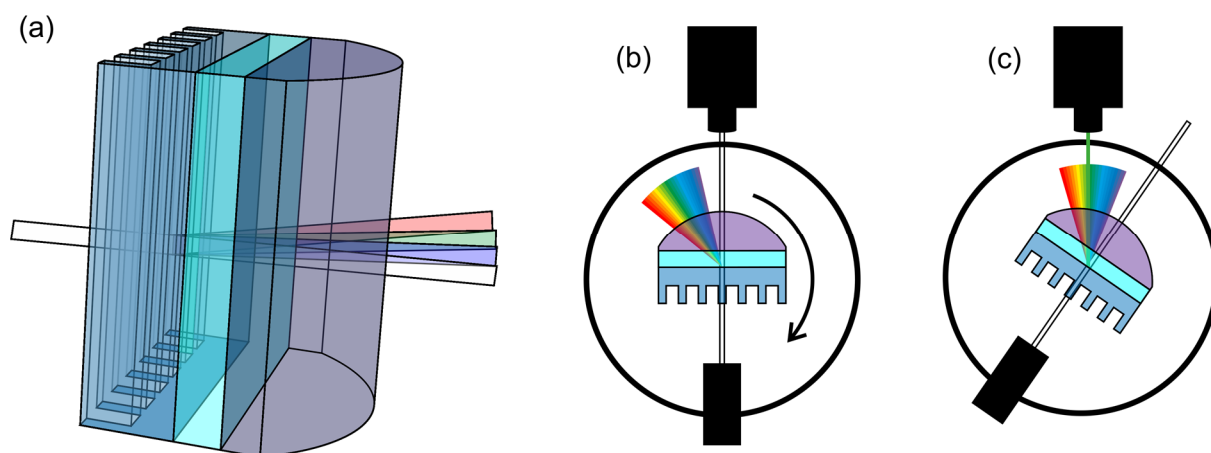
Figure 27. (a) Scheme showing the use of a cylindrical lens for extraction of the diffracted orders, (b) the complete measurement setup and its rotation for (c) measuring the diffracted orders.

This coupling arrangement minimizes reflections as well as angle distortions, but leads to (de–) focusing of the beam due to the lens. The distance between sample and detector should therefore be small, which also helps mitigate losses due to the diffraction dispersion. Further, the use of a spectroradiometer (PR–705 Spectrascan®) with integrated optics helps collecting as much of the diffracted light as possible. The assembled measurement setup is depicted in Figure 27 (b): the parts shown in Figure 27 (a) were mounted on a rotating plate together with a white light source (DH–2000 tungsten lamp, Ocean Optics). The spectroradiometer was fixed next to the plate and initially faced the light source perpendicularly. The aligned setup was then calibrated on a non–patterned part of the sample by moving the substrate with respect to the (clamped) half–cylinder. In this way it was possible to take the defocusing effect into account for the calibration. For measuring the diffracted orders, the grating was shifted back into the beam and the plate was rotated in steps of 2° while the intensity of the diffracted light was measured by the spectroradiometer. Each of the measured spectra showed a distinct peak at the position of the positively interfering wavelength for the according angle (grey curves in Figure 28; each peak was recorded at a different angle). The positions of the peaks match the calculations from equation [2–1] for all the angles, supporting the validity of this approach. For the discussion of the results, only the peak maxima are considered and plotted to improve the clarity of the graphs (the crosses in Figure 37 e.g. correspond to the maxima of the curves in Figure 28)
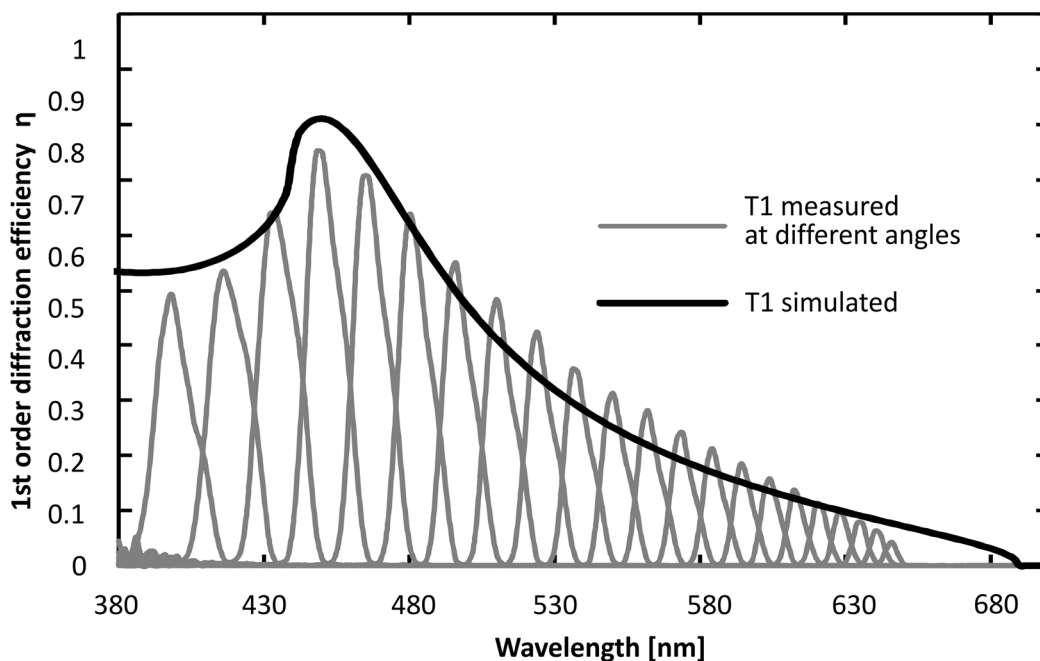
Figure 28. Simulated and measured first order diffraction efficiencies.

3.2.2 Zero order measurements

Zero order transmission was measured in a Lambda 9 spectrophotometer at angles varying between 0° and 80° incidence. A custom holder, adjustable in steps of 10°, was used for this purpose. The same instrument was also used for measurement of specular reflection at a minimum angle of 6°. For measurement of the stretchable polymer, the same instrument was used. Since the substrate is flexible, the (strained) device had to be stabilized by applying a glass slide to its back side. Ormocer was used for reversible attachment and no residues were left on the Polyurethane after peeling the glass slide.

3.3 Structure determination

3.3.1 Atomic force microscopy (AFM)

AFM is a very convenient technique for characterizing originated or replicated gratings. Period and depth of the grating can be determined within minutes by scanning a few lines. Imaging of larger areas (≈ 10 µm) would require a slow scanning speed in AFM and was hence either performed with an optical microscope or SEM, depending on the feature sizes. Other general drawbacks of AFM are its inability to measure below the surface and the dependence on a tip, which makes it impossible to measure steep features (and also distorts the grating profile due to tip convolution).

The present Park XE–70 AFM was used in non–contact mode. The instrument allows measuring on wafer size samples. High aspect ratio tips had to be used in order to reach the bottom of the grating trenches.

3.3.2 Scanning electron microscopy (SEM)

Scanning electron microscopy was mainly used to characterize evaporated thin films or the grating profile. Those parameters are not available to AFM, which otherwise is a much faster and non–invasive method to determine structure parameters. Samples for SEM were fabricated

using UV embossing on glass substrates. They could subsequently be broken to access the grating cross section. The substrates had to be sputtered with 10 nm of gold to ensure conductivity. They were finally imaged in a Hitachi S–4100 SEM. Layers of different materials could hereby be identified and characterized.

3.3.3   Metal thickness measurement

Accuracy of the metal thickness was verified with a KLA Tencor P–10 profilometer on a flat part of the samples. This value was then also used for building the simulation models, keeping in mind that, for oblique deposition, only a fraction of the evaporated material D actually reaches the sample (proportional to $\cos(\alpha)$).

3.4   Simulations

3.4.1   Rigorous coupled wave analysis (RCWA)

Rigorous coupled wave analysis is based on the rigorous solution of Maxwell's equations in periodic media and has been developed by Moharam and Gaylord in the 1980s [190]. When considering an arbitrarily shaped surface grating, three regions are distinguished: The incident medium (called superstrate), the grating region, and the substrate. Permittivity functions are subsequently defined for all the regions: For substrate and superstrate, they simply correspond to the intrinsic properties of the according materials, whereas the permittivity in the grating region, $\varepsilon_2(x, z)$, is position dependent. For practical reasons, the grating region is often sliced perpendicularly to the z–direction, which creates layers that only show a variation in permittivity along the x–direction (Figure 29). The resulting permittivity is usually approximated by a Fourier series, since strata consisting of individual blocks are conveniently used for modelling gratings:

$$\varepsilon_2 = \sum_{h=-\infty}^{\infty} \varepsilon_h \exp\left[i\, h \frac{2\pi}{\Lambda} x\right], \qquad\qquad [3\text{–}1]$$

where ε_h are the Fourier coefficients and Λ is the grating period. Note that this expansion is only applicable to periodic media, which also restricts the RCWA formalism to such structures.

The electric field in each region is a superposition of transmitted and reflected plane waves. For the superstrate region, we have to consider the incoming radiation as well as the sum of the reflected orders:

$$E_1 = \exp[-i(\beta_0 x + \xi_{10} z)] + \sum_{m}^{N} R_m \exp[-i(\beta_m x + \xi_{lm} z)], \qquad [3\text{–}2]$$

where i is the imaginary number, $\beta_m = k_1 \sin(\theta) - mK \sin(\phi)$ and $\xi_{lm}^2 = k_l^2 - \beta_m^2$ with $k_l = 2\pi \varepsilon_l^{1/2}/\lambda$ (l is the region index, 1 for the superstrate, 2 for the grating region, 3 for the substrate), m is the diffraction order, K is the grating vector, θ is the polar angle of incidence and ϕ is the angle of tilt of the modulated permittivity within the grating region with respect to the interfaces. R_m are the reflection intensities of the individual orders, which will be some of the results of the calculations. Note that ϕ is not relevant for the structures used in this thesis, since

the considered grating ridges are arranged perpendicularly to the substrates. For the grating region, the equivalent equation reads:

$$E_2 = \sum_m^N S_m(z)\exp[-i(\beta_m x + \xi_{2m} z)] \, ,$$ [3–3]

where $S_m(z)$ is the position dependent, normalized field amplitude for the mth order wave and $\xi_{2m} = k_2 \cos(\theta') - mK \cos(\phi)$ with θ' being the angle of incidence after refraction at the interface between medium 1 and medium 2.

The wave equation:

$$\nabla^2 E_l + \left(\frac{2\pi}{\lambda}\right)^2 \varepsilon_l(x,z) E_l = 0$$ [3–4]

then has to be solved in all three regions $l = 1, 2, 3$ with continuous boundary conditions at the interfaces. The solutions to the resulting coupled–wave equations are not discussed here but can be found in the original articles [190], [191] as well as recent reviews [192].

In practice, the number of diffraction orders m as well as Fourier orders h (in the permittivity function) have to be limited, which is one of the main sources of numerical errors. If this truncation is however done well, RCWA based methods are very fast and accurate for diffractive gratings. The method is in principle applicable to any periodic geometry that can be dissected into slices (staircase approximation). The computation time however scales with the number of layers and it is therefore beneficial to use simple models, especially if many parameters are screened. When for example running computations on models like the one shown in Figure 29, a far field spectrum can be calculated within a minute on a typical desktop computer. The major drawbacks of RCWA based methods are their restrictions to periodic structures and far–field observations [193].
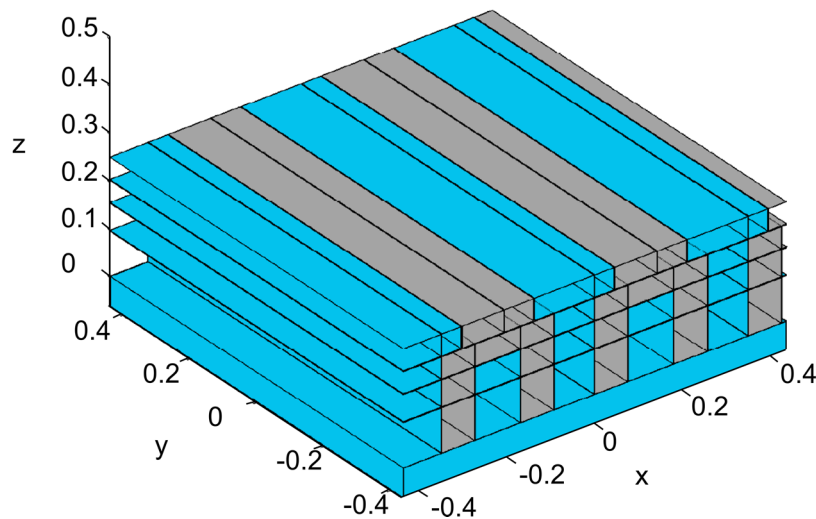
Figure 29. RCWA model of aluminum U–shapes as used in Chapter 5.

For the reported work, RCWA was interfaced with Matlab®, where modeling of the structures and post processing took place. This configuration helped evaluating viable grating parameters in a quick fashion. Angle and wavelength dependence of the calculated optical properties can

also be displayed in color coded maps for reproducing the dispersion of optical features. Finally, colorimetric processing of the resulting spectra is also directly performed in Matlab®.

3.4.2   Surface integral equation method (SIE)

SIE is based on the evaluation of a dyadic Green's function $\overleftrightarrow{\boldsymbol{G}}$, which describes fields caused by a point source. For illustration, in the case of an electric dipole this would read:

$$\mathbf{E}(\mathbf{r}) = \omega^2 \mu_0 \mu \overleftrightarrow{\boldsymbol{G}}(\mathbf{r}, \mathbf{r}')\mathbf{p}(\mathbf{r}'), \qquad\qquad [3\text{–}5]$$

where $\mathbf{E}(\mathbf{r})$ is the electric field at position $\mathbf{r}$ caused by the dipole $\mathbf{p}$ situated at $\mathbf{r}'$, μ_0 is the vacuum permeability and μ the material permeability [75]. In SIE, the wave equation for homogeneous spaces (which can be derived from Maxwell's equations) has to be considered:

$$\nabla \times \nabla \times \mathbf{E}_n(\mathbf{r}) - k_n^2 \mathbf{E}_n(\mathbf{r}) = i\omega\mu_0\mu\mathbf{j}(\mathbf{r}) , \qquad\qquad [3\text{–}6]$$

where $\mathbf{r}$ is the position vector, which is part of a piecewise homogeneous medium dissected into volumes V_n ($\mathbf{r} \in V_n$), k_n^2 is the wavenumber for waves in the corresponding volume piece n, i is the imaginary number, ω is the angular frequency and $\mathbf{j}(\mathbf{r})$ is the volume current density. Introducing the dyadic Green's function $\overleftrightarrow{\boldsymbol{G}}_n$ yields:

$$\nabla \times \nabla \times \overleftrightarrow{\boldsymbol{G}}_n(\mathbf{r}, \mathbf{r}') - k_n^2 \overleftrightarrow{\boldsymbol{G}}_n(\mathbf{r}, \mathbf{r}') = \overleftrightarrow{\mathbf{1}}\delta(\mathbf{r} - \mathbf{r}') , \qquad\qquad [3\text{–}7]$$

where $\delta(\mathbf{r} - \mathbf{r}')$ is the Dirac delta function. After some transformations, the equation is integrated over the volume V_n. Application of Gauss' theorem then allows the transition from volume current densities to surface current densities along the boundary ∂V_n. From there, the so called electric field integral equation (EFIE) for the limit $\mathbf{r} \to \partial V_n$ can be derived:

$$\left(i\omega\mu_n \int_{\partial V_n} \mathrm{d}S' \overleftrightarrow{\boldsymbol{G}}_\mathbf{n}(\mathbf{r}, \mathbf{r}') \cdot \mathbf{J}_n(\mathbf{r}') \right.$$

$$\left. + \int_{\partial V_n} \mathrm{d}S' \left[\nabla' \times \overleftrightarrow{\boldsymbol{G}}_\mathbf{n}(\mathbf{r}, \mathbf{r}') \right] \cdot \mathbf{M}_n(\mathbf{r}') \right)_{\mathrm{tan}} \qquad\qquad [3\text{–}8]$$

$$= \left(\mathbf{E}_n^{\mathrm{inc}}(\mathbf{r}) \right)_{\mathrm{tan}} , \mathbf{r} \in \partial V_n$$

where $\mathbf{J}_n = -\hat{\mathbf{n}} \times \mathbf{H}$ and $\mathbf{M}_n = -\hat{\mathbf{n}} \times \mathbf{E}$ are the aforementioned surface current densities defined on the boundaries ∂V_n and the subscript "tan" indicates that the tangential components of fields are considered. The same is performed for the magnetic field and finally the equations can be adapted to suit periodic boundary conditions if required. Deriving the entire formalism for solving these surface integral equations would go beyond the scope of this thesis and require extensive mathematical explanations. The reader is referred to textbooks for general discussions on Green's functions [75] or publications for the specific formalism employed in the present simulations, which has been developed in the Nanophotonics and Metrology Laboratory at EPFL [194], [195].

The solutions attained with SIE allow calculation of the electric field at each position in space. This method can therefore be utilized for near–field as well as far–field computations. Comparing the electric fields directly above and below each surface further also allows calculating surface charges via Gauss's law. SIE can handle single as well as periodic structures

and in the latter case, only one unit cell needs to be modeled and periodic boundary conditions are applied. SIE also allows discretization and simulation of arbitrarily shaped objects, without requiring a staircase approximation like RCWA. The surfaces of each object are dissected into triangles with predefined edge lengths, which form the surface boundaries ∂V_n (Figure 30 shows the SIE counterpart to the RCWA model in Figure 29). The surface normal of each facet defines its orientation (purple arrows in Figure 30) and in the present example e.g. all of them point away from the metal structure into the surrounding dielectric. The major drawbacks of SIE are its high demand for computational resources and slow speed: The memory requirements scale with the number of triangles in the model and calculations on the mesh in Figure 30 for example take more than an hour for each wavelength. Note that the triangles cannot assume arbitrary sizes; simulations can yield wrong results if the model is too coarse (especially for plasmonics).
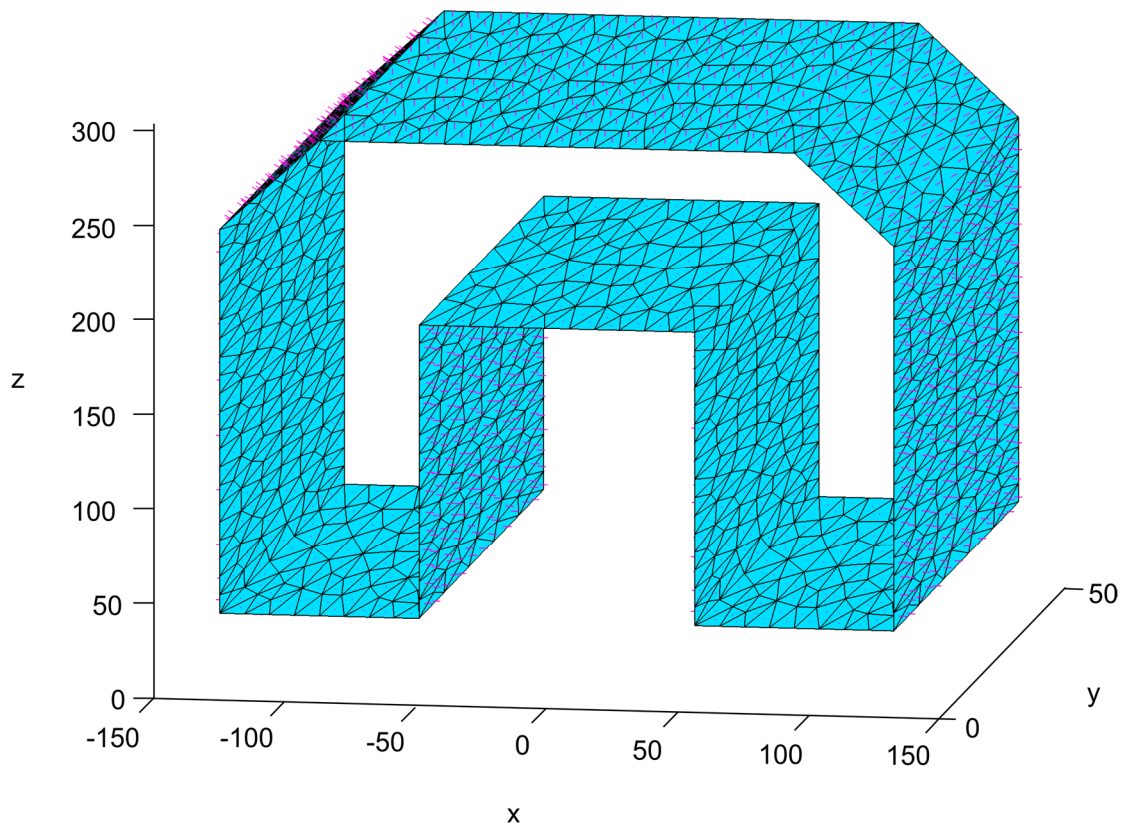
Figure 30. Example of a mesh used for SIE computations.

For the SIE program used in this thesis, the three dimensional models of the structures have been defined in python, but meshing programs like e.g. Gmsh would be viable alternatives. Electric fields were calculated either close to the structures (near–fields) or at a vertical distance of 50 μm (far–field). For far–field calculations, an additional averaging over several points in space was necessary to prevent anomalies in the diffraction regime of the grating. It is finally worth mentioning that the particular code employed in this thesis is still in development; it is therefore less user–friendly than the commercial RCWA program, but much easier to customize.

Chapter 4   Asymmetric Diffraction

4.1   State of the art

Grating diffraction is an established field of research that had its apex of academic interest around 10 years ago, with a constant stream of publications from then onwards (Figure 31). This existing knowledge has facilitated the transfer of new technologies to the industry. Innovations in this field however recently focused on optimization rather than radical changes, which mainly include tuning of structures or fabrication parameters to increase the diffraction efficiencies. Most of the asymmetric grating structures have hence also been known for more than a decade and share very similar advantages and drawbacks. I will give a short overview on their principles and properties before presenting the innovative alternative developed and patented during this thesis.
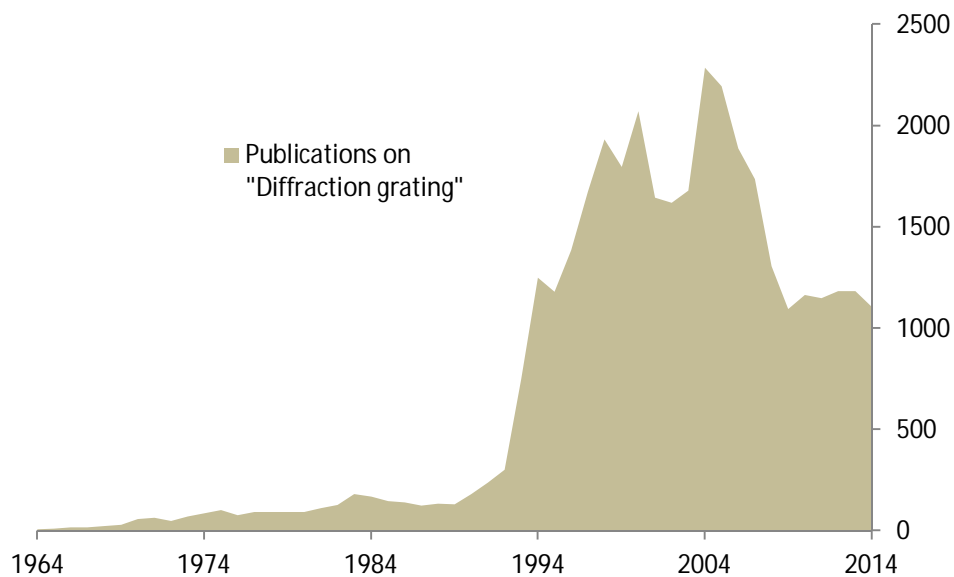
Figure 31. Number of Articles per year found for the keyword "diffraction grating" on Scopus.

As discussed in Section 2.1 it is beneficial to use asymmetric gratings for many practical configurations in applications like e.g. waveguiding, lighting or photovoltaics. The classical blazed grating thereby shows a triangular profile with an inclination angle to the surface normal (Figure 32 (a)). Such gratings can show close to 100% diffraction efficiency in Littrow configuration [196] and are therefore popular in e.g. laser cavities, where this allows for efficient mode filtering [27]. They have however been recognized to suffer from shadowing effects when operated in transmission (including the favorable perpendicular incidence geometry), which severely reduces the achievable efficiency when the grating period becomes comparable to the incident wavelength (e.g. low diffraction orders, steep output angles) [197], [198]. Also, generating sub–micrometer triangular shapes with the desired angles is challenging.

A natural approximation of the triangular lineshape is the multilevel blazed grating visible in Figure 32 (b) [199]. In fact, multilevel blazed gratings can even surpass the efficiency of their continuous counterparts if properly designed, but the fabrication is very challenging: Usually, each level has to be fabricated separately in e.g. a lithographic process and therefore needs to be carefully aligned with the previous level [200]. Further, high aspect ratios and small feature sizes are required [201]. This is especially problematic for replication, which makes this approach ill-suited for high-throughput processes.

Another popular approach is binary blazing (Figure 32 (c)). Here, each period of the grating contains two or more subwavelength features of the same depth. These sub-period features can be treated as an effective medium with varying refractive index. This means that the local refractive index n_{eff} is determined by the refractive indices of the superstrate n_{sup} and the grating material n_{grat} as well as their respective fractions f_{sup} and f_{grat} (where $f_{sup} = 1 - f_{grat}$ and $f_{grat} = dc$). Simple approximations for binary, dielectric elements are polarization dependent and given by [202]:

$$n_{eff}^{TE} = \left[n_{sup}^2 \left(1 - dc \right) + n_{grat}^2 \, dc \right]^{\frac{1}{2}} , \qquad \text{[4–1]}$$

$$n_{eff}^{TM} = \left[\left(1/n_{sup} \right)^2 \left(1 - dc \right) + \left(1/n_{grat} \right)^2 dc \right]^{-1/2} . \qquad \text{[4–2]}$$

By proper design it is therefore possible to create a graded effective medium with a blazed refractive index. Binary blazed gratings can reach efficiencies higher than 95% for polarized light [203]. Originating such structures is easier than fabricating multilevel gratings, but still relies on e-beam lithography [204]. Also, efficient solutions for typical polymers require high aspect ratios [201], which makes replication very challenging. It is worth noting that actual graded index materials can of course also be fabricated with a periodic, asymmetric distribution of refractive indices. The fabrication process however is expensive, cannot generate sharp index changes and yields efficiencies comparable to their surface modulated counterparts [197]. Also, the process is clearly lower throughput than the replication of a surface grating; it is therefore understandable that this approach is limited to special substrates and applications.

Slanted gratings (Figure 32 (d)) compose a final class of asymmetric diffractive elements, which was developed in the 1990s [205], [206] but popularized more recently by Nokia [36]. The lineshape of such gratings is similar to their binary counterparts, but the ridges have oblique sidewalls. Fabrication of slanted gratings hence is also similar to the approach used in this thesis (3.1.1) with two major differences: Etching is performed at an oblique angle and the hard mask in consequence needs to be shallower to prevent shadowing effects. The mask can for example be obtained by etching into a metal layer after patterning the photoresist. Replication is clearly more challenging for slanted gratings due to the inclined surfaces, but possible with sophisticated anti-adhesion treatment. Diffraction efficiencies in excess of 80% were experimentally shown [171].
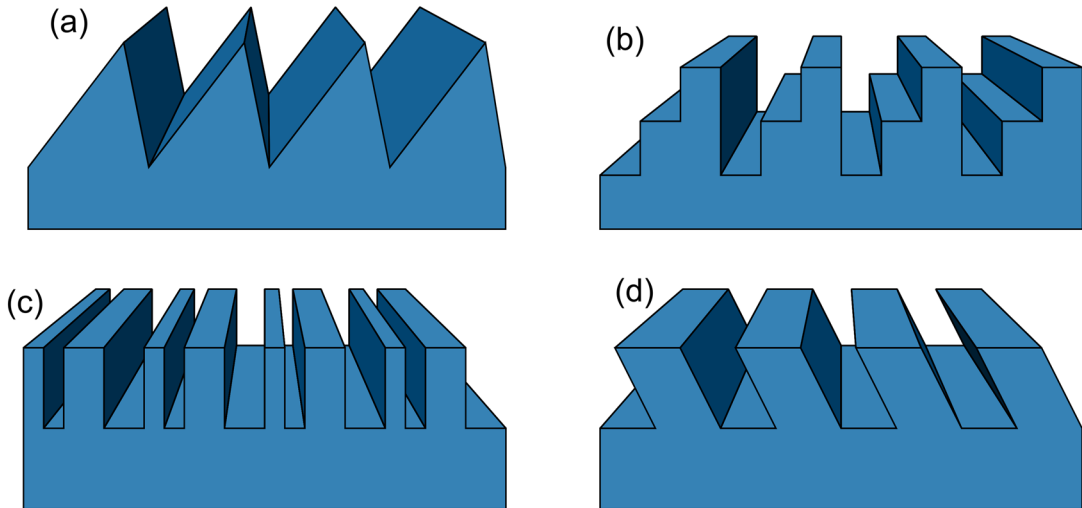
Figure 32. Gratings with (a) triangular, (b) multilevel, (c) subperiod binary and (d) slanted lineshapes.

All of the above approaches are preferably used in conjunction with high refractive index materials since the diffraction efficiency can be increased by enhancing the refractive index difference between the grating material and the covering material [207]. The straightforward approach of directly structuring high refractive index materials like TiO_2, ZnS or silicon however is challenging and relies on photolithographic processes. The evaporation–based approach that I have developed and is presented in the following is therefore much better suited for high–throughput fabrication and has great potential for implementation in many different products that rely on efficient diffraction.

4.2   Asymmetric coatings for efficiency enhancement

4.2.1   Dielectric coating

Due to the challenging replication of the state-of-the-art gratings, I here present a novel approach, which does not require sophisticated grating masters. The results have been published in Optics Letters [208] and formed the basis for the patent application WO2015062641 (A1) [209]. The technique relies on the replication of binary gratings and subsequent angle evaporation with either dielectrics or metals to blaze the grating replica. This simple yet powerful procedure was already used more than 30 years ago to generate structures as small as ≈10 nm [210]. The same method is used here to apply a ZnS coating and achieve non–polarized first diffraction order transmittance (T1) efficiencies at perpendicular incidence close to 70%. All the processes are suitable for mass production and therefore this approach is a flexible alternative to existing procedures for industrial manufacturing of blazed gratings. Since the grating is very simple, it can be replicated by any of the common mass production methods such as hot embossing or injection molding, and is not limited to UV casting. Finally, the structure remains functional even when embedded in the substrate material, which is not the case when using any embossed surface relief gratings (similar to buried high refractive index coatings recently investigated [34]).

Hot embossing and UV casting methods were used with PC and Ormocer® respectively (3.1.3). Subsequently, ZnS is evaporated on the grating at an angle $45° < \alpha < 60°$ with respect to the surface normal (Figure 33 (b)). ZnS was chosen because it has a high, well controlled refractive index and exhibits a good wetting properties on many dielectric substrates. An SEM picture of

the resulting asymmetric structure, produced by self–shadowing of the grating, is shown in Figure 33 (a). Note that the shape of the coating can be tuned by varying the evaporation angle or the distance between sample and source material (3.1.2).

(a)

(b)

(c)

α

TE   TM

(d)   (e)

T1 direction   T1 direction
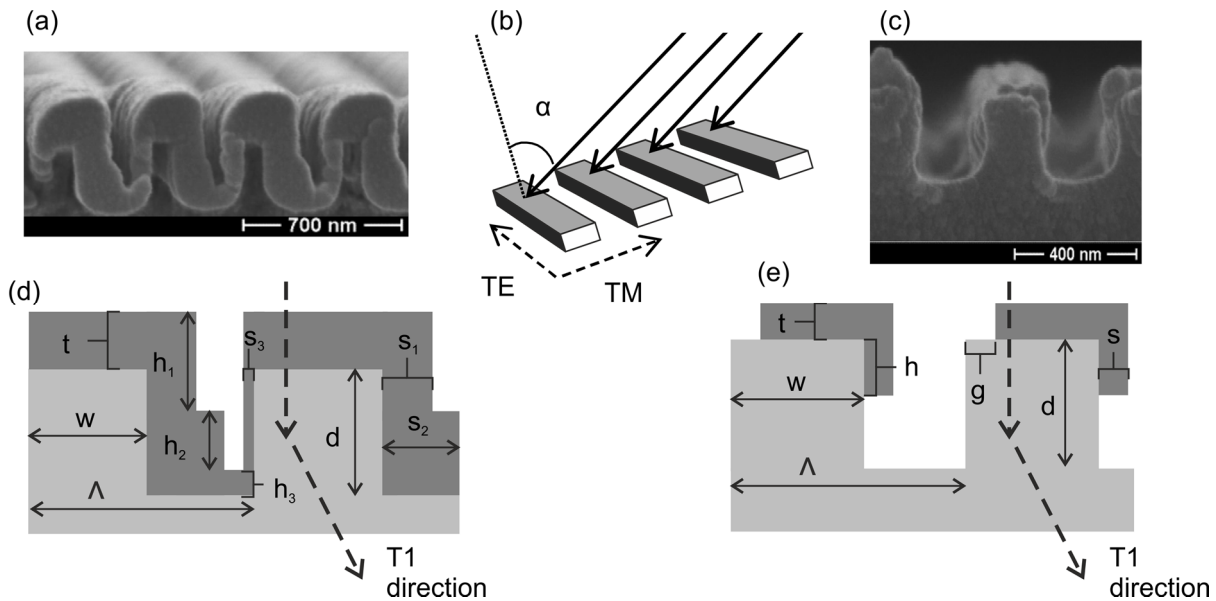
Figure 33. (a) SEM of the fabricated ZnS coated grating, (b) direction and nomenclature of the evaporation angle and the polarizations, (c) SEM picture of the obtained aluminum structure, (d) and (e) show the models and variables used for simulations with ZnS and Al coatings respectively. The dashed arrows indicate the orientation of the first diffraction orders for the two structures.

Choice of the present grating period around 440 nm is optimal for efficient diffraction of the visible spectrum as calculations of the diffraction angles $\theta_m^{T/R}(\lambda)$ using equation [2–1] illustrate. At perpendicular incidence ($\theta_i = 0$), for most of the visible spectrum, only T0, T1 and T–1 exist for the grating under study with a period of $\Lambda = 440$ nm: for $m = \pm 1$ and $n_2 = 1.5$, wavelengths up to $\lambda = 660$ nm are diffracted, whereas the maximum diffraction wavelength for $m = \pm 2$ lies at $\lambda = 330$ nm. Angles for the first reflection diffraction orders $\theta_m^R(\lambda)$ are obtained by choosing $n_2 = 1$, which yields a maximum wavelength of $\lambda = 440$ nm for the same grating. These calculations motivate the choice of $\Lambda = 440$ nm as the preferred grating period: No transmission orders above 1 and no reflection orders apart from 0 exist in the visible, thus allowing for maximum T1. Additionally, at perpendicular incidence, all wavelengths between 440 nm and 660 nm are diffracted to angles larger than the total internal reflection angle, therefore allowing for waveguide coupling of almost the entire visible spectrum.

In order to understand the response of such gratings, numerical simulations have been performed using rigorous coupled–wave analysis (RCWA) based programs [190]. The models used for these simulations are sketched in Figure 33 (d) and (e). Figure 33 (b) additionally shows the definition of polarizations (TE and TM) for a grating in classical mount, which is also commonly used at perpendicular incidence as chosen in the present simulations and experiments. It is worth mentioning that simpler models than one used here yield very similar efficiencies, but the shape of the spectra will look different. The process hence should be very robust with respect to fabrication deviations.

The refractive index was set to 1.5 for the substrate (polymer/glass) and to 1 for the top material (air). Refractive index data for ZnS is obtained from reference [211]. The geometrical parameters are $t = 150$ nm, $w = 0.33\Lambda$, $d = 285$ nm (original depth was 320 nm, the shrinkage

comes from heat transfer during evaporation), $h2 = 0.66t$, $h3 = 0.37t$, $h1 = t + d - h1 - h2$, $s1 = 0.66t$, $s2 = 1.15t$, $s3 = 0.15t$, which is consistent with SEM measurements.
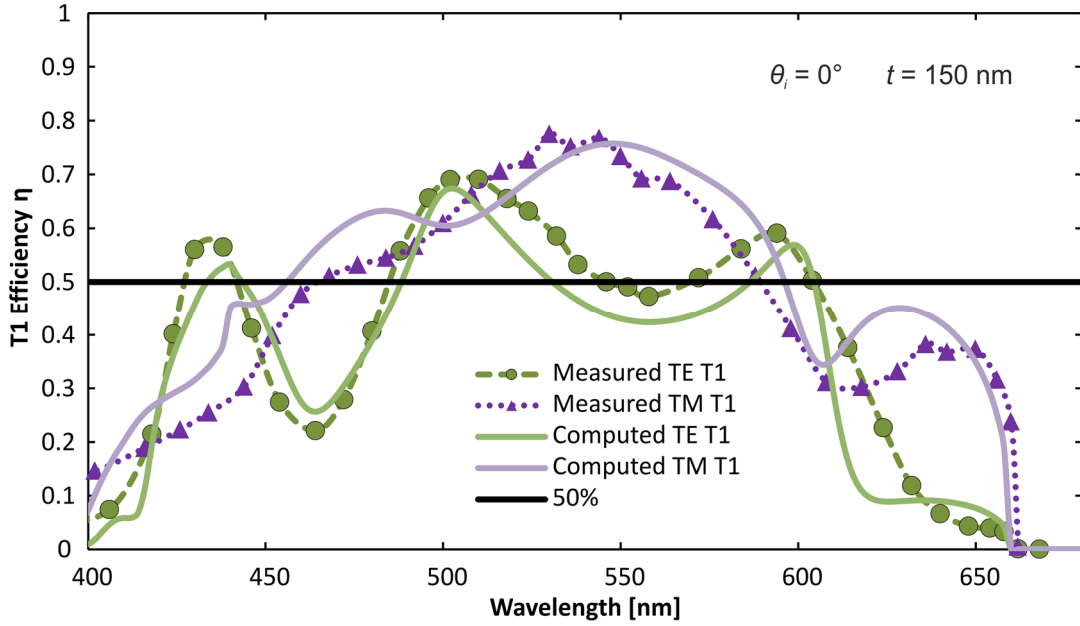

Figure 34. Maxima of the measured 1st order diffraction efficiencies (filled symbols) for both polarizations at perpendicular incidence, together with the corresponding computed data (solid lines). Those results were obtained with the structure shown in Figure 33 (a).

The measurements show first order transmittance efficiencies (T1) of almost 70% (filled symbols in Figure 34, neglecting the ≈4% reflectance off the reference glass) for both polarizations simultaneously at around $\lambda = 510$ nm (green). Note that this is well above the theoretical limit of $T1 < 50\%$ for a symmetric grating at perpendicular incidence, clearly demonstrating the strong enhancement of the T1 efficiency caused by the asymmetric coating. T−1 will not be considered since it is very low by design. The simulation results (solid lines) are plotted with the measurements (filled symbols in Figure 34). The agreement between simulations and measurements is very good for both polarizations.

The effect of the asymmetric coating on the bare binary grating is also visualized in the following series of simulations (Figure 35) that show how T1 efficiencies evolve when increasing the ZnS coating thickness t from 0 nm to 150 nm. A common trend seen for all the gratings and coatings investigated is that by increasing the coating thickness, T1 is first enhanced for TE polarized light (peaking at $\eta = 90\%$ for 60 nm of ZnS in the present case, blue curve in Figure 35 (a)), whereas efficient diffraction of TM polarized light requires thicker coating layers (peaking at $\eta = 80\%$ efficiency for 90 nm of ZnS, green curve in Figure 35 (b)). This finding can be explained by the difference in effective refractive index for the two polarizations as described in Section 4.1 (equations [4−1] and [4−2]). It is also consistent with the general design rule $d + t = \lambda/(n - 1)$ for 2π phase shift modulators as e.g. used for binary blazed gratings [207]. For $t = 90$ nm, $d = 285$ nm and $n = 2.4$ we e.g. receive $\lambda = 525$ nm, which is close to the maximum of the green curve in Figure 35 (a). It is also well understood that, in 1D gratings, the effective refractive index is lower for TM polarized light than TE polarized light (compare to Section 4.1), which explains the discrepancy between the two maxima.

The simulations also show that by increasing the ZnS thickness, spectral features of T1 not only increase in intensity before diminishing again, but additional peaks appear in the blue portion of

the spectrum and then red–shift until they reach wavelengths that are evanescent ($\theta_m^T(\lambda)$ in equation [2–1] becomes 90°, which occurs at $\lambda = 660$ nm for the grating considered here). Since the peaks for TE and TM polarized light are not spectrally aligned, intersections of the two curves provide the wavelengths for unpolarized operation. To this end, Figure 35 (d) shows the absolute value of the T1 intensity difference between both polarizations, which should be as low as possible in order to keep the coupled light unpolarized. For green light, where the human eye is the most sensitive, the 150 nm ZnS coating fulfills this requirement best (black line in Figure 35 (d)). Therefore, although in the relevant wavelength range a ZnS coating of 120 nm would provide slightly higher total diffraction efficiency (data not shown) than 150 nm, the thicker coating was chosen for the present device.
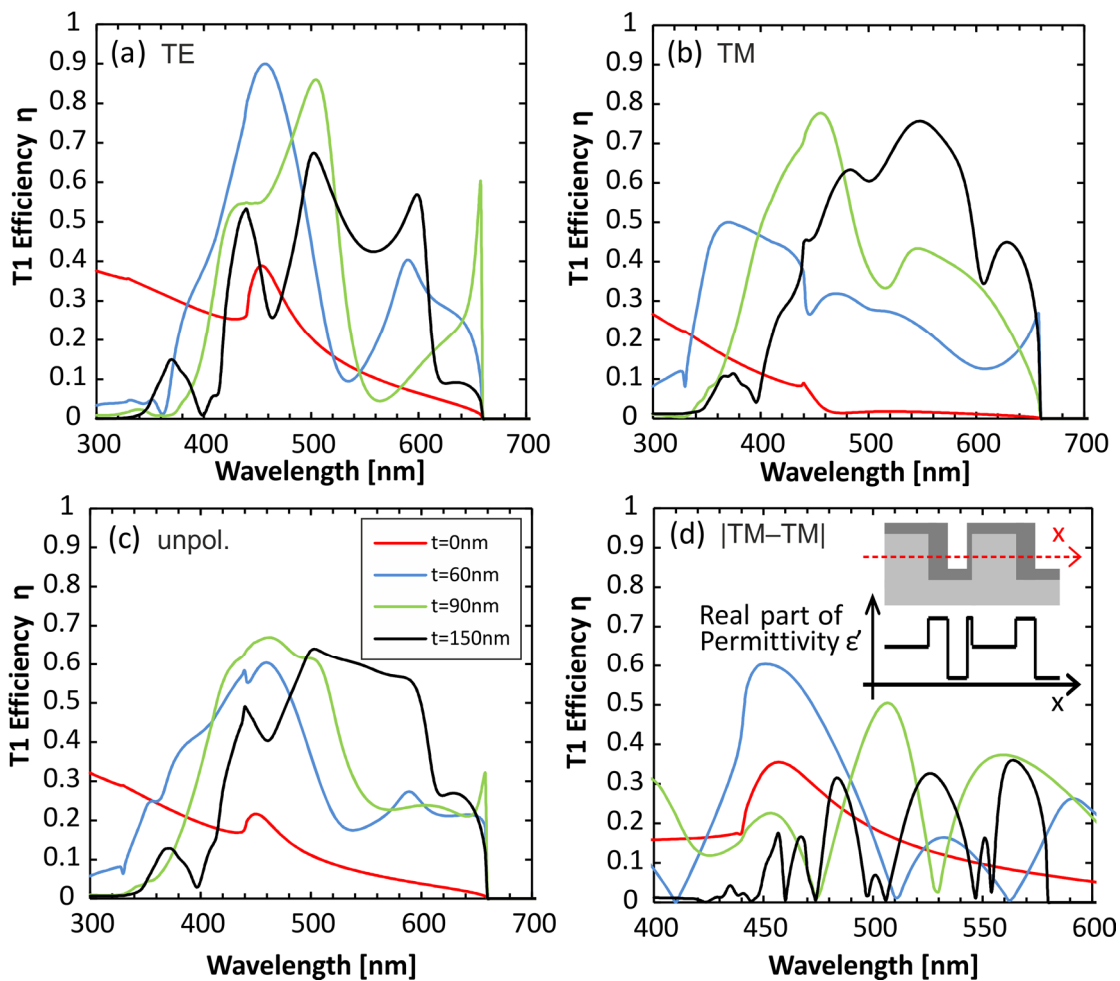

Figure 35. Computed T1 data is plotted for increasing ZnS thicknesses *t* for (a) TE polarized light and (b) TM polarized light. (c) Shows the average of the two and (d) the difference between them. Inset: Schematic representation of the real part of the permittivity (black line) at the lateral position indicated by the red axis in the structure sketched above.

The present structure can be related to multilevel blazed gratings when looking at the cross–section perpendicular to the grating lines. The inset in Figure 35 (d) illustrates qualitatively how the real part of permittivity varies along the x–axis (indicated in red) through the cross–section. The shape of the resulting graph looks similar to the cross–section of a multilevel blazed grating [201], which provides an explanation for the blazed behavior.

The asymmetric dielectric structure can finally also be embedded into e.g. the substrate polymer while still providing diffraction efficiencies in excess of 50% at perpendicular incidence (Figure

36). This property allows protecting the active structure from wear and other environmental influences such as humidity or, in the case of metals, oxidation. Figure 36 also exhibits a broad angle of operation between −5° and 20° angle of incidence within the polymer (−7.5° to 31° in air), which is very convenient when either using non−collimated light sources such as e.g. LEDs or the sun, which changes its position throughout the day/year. Light guiding as well as light harvesting applications can therefore strongly benefit from this technique.
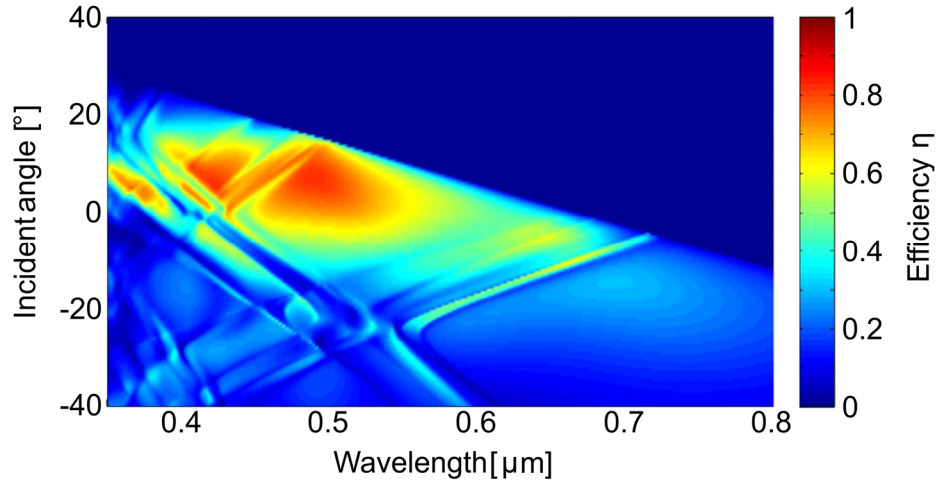

Figure 36. Calculated non−polarized diffraction efficiencies for the ZnS coated structure discussed in Figure 34 when coated with polymer.

4.2.2   Metallic coating

Metallic coatings were also investigated and included the evaporation of 20 nm Al at an angle $\alpha > 60°$ with respect to the surface normal. The resulting structure is shown in Figure 33 (c) and was used for color effects (Section 4.3). For the aluminum structures, the design parameters are the grating depth d, the period Λ, the structure width w, the evaporation angle α with respect to the surface normal and evaporated metal thickness D (as set on the evaporator). The effective metal thicknesses on the top, respectively on the sidewall of the grating, t and s in Figure 33(e), are related to D and α through simple geometrical considerations: $t = D \cos(\alpha)$ and $s = D \sin(\alpha)$. At the same time, the metallization depth h on the sidewall of the grating is determined by the width w of the grating lines, the period Λ and the evaporation angle α using the relation $h = (\Lambda - w)/\tan(\alpha)$. A similar geometrical approach was also used by Ye *et al.*, although they did not correct the metal thicknesses for the evaporation angle in their work [212]. A final feature (also visible in the SEM picture in Figure 33 (c)) is a small uncovered part on the top of the grating. The corresponding dimension is set to 0.03 Λ, which is consistent with the SEM images. The width w was measured to be 0.3 Λ, corresponding to a duty cycle of $dc = 0.3$. The refractive index data for aluminum from reference [213] was used for the simulations.

Metals like silver, gold or aluminum have refractive indices between 0.1 and 1.5 in the visible, but exhibit high absorption coefficients k. This results in a strongly negative real part of the permittivity $\varepsilon' = n^2 - k^2$ and therefore also in a high difference between the substrate and the metal permittivities. This difference is much higher for metals ($\varepsilon' \approx -35$, resulting in a difference of $\Delta\varepsilon' \approx -37$ in the case of aluminum [213]) than for high refractive index materials such as ZnS ($\varepsilon' \approx 6.75$, resulting in a difference of $\Delta\varepsilon' \approx 4.5$). Very thin metal coatings (5−20 nm) can already strongly enhance T1 efficiencies: Figure 37 illustrates how T1 efficiencies in excess of 70% can

be achieved for TE polarized light when using angle evaporation of 20 nm aluminum. Simulations using the model shown in Figure 33 (e) based on the SEM image Figure 33 (c) were performed to verify this finding (solid line in Figure 37).
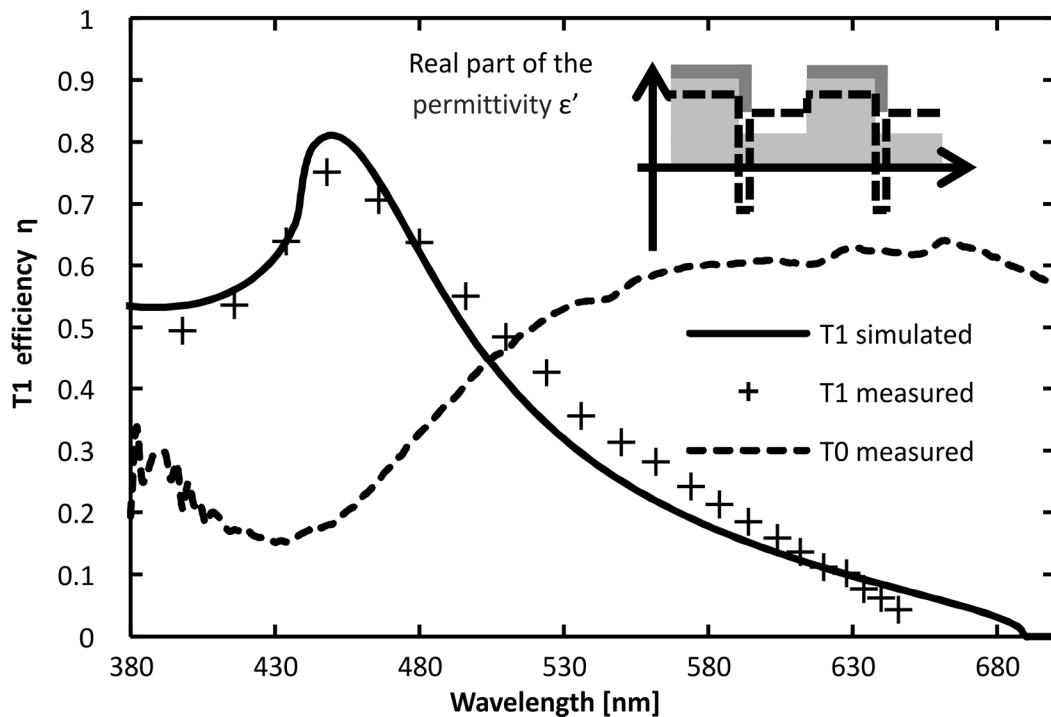
Figure 37. Experimental T1 efficiencies η (crosses) measured for perpendicularly incident TE polarized light at the individual angles plotted together with the computed data (black solid line) and zero order transmittance (dashed line). The graph exhibits efficiencies in excess of 70% for the metallized grating shown in the SEM image of the inset. The inset also depicts the real part of the permittivity along the cross–section of such a structure.

Additional simulations were performed in search of an explanation for the observed diffraction efficiency enhancement through metallization. I substituted the refractive index of the Al coating with an artificial material with a constant complex index of refraction of $n = 1$ (matching the superstrate's index) and $k = 5.4$ and could reproduce the strong enhancement of T1 also for the artificial material. This observation suggests that the parameter to consider when tuning coatings for increasing diffraction efficiencies is indeed the real part of permittivity and not the refractive index n. This makes a lot of sense, since it is the boundary conditions associated with Maxwell's equations that dictate how the electromagnetic field behaves at the different material's interfaces and these boundary conditions rely on the permittivity, not the refractive index. The inset in Figure 37 illustrates qualitatively how the permittivity of the structure changes along the metallized grating's cross–section, which is again very similar to the cross–section of a multilevel blazed grating. The same explanation previously used for dielectric coatings therefore also holds for the enhanced T1 efficiency observed for metallized gratings. Thicker metal coatings on the other hand appear to strongly enhance reflection into a single higher order (computed data not shown). For TM polarized light and properly chosen parameters, the present structure might also be capable of enhancing one of the evanescent modes to launch surface plasmons into a specific direction (similar to already investigated asymmetric metal gratings [214], [215]). The use of asymmetric metallization for efficient diffraction could pave the way to new applications that require electrical contacts. However, a general drawback of using metals for light diffraction is the inherent absorption, (as evident from the non–zero imaginary part of the permittivity ε'').

4.3   Color effects

Periodic structures and especially gratings are standard components for security features such as holograms or DIDs as discussed in Section 2.1.2. However, these known security features all work in reflection, which is required by the products they were designed to protect. Transmission has been a rare configuration in the past, but will become more and more important with the recent introduction of polymer banknotes in several countries. Further, instruments like e.g. smart phones or other display-based devices currently lack an efficient form of brand protection. Transmission based optical effects should therefore be of increasing interest in the near future. Working in transmission however does not only mean addressing different devices, physical properties can also be fundamentally different: The concept of reciprocity of optical paths for example does not impose the same restrictions on the effects available. A flat, reflection based feature has to have identical colors upon in–plane rotation by 180°, which is clearly not the case for transmissive objects. This not only enhances the design space available, but also enables completely different effects, which can be very surprising for consumers and attract them to the product. In the following, two optical effects which can only occur in transmission and are suited for roll–to–roll fabrication (typically encountered in the security industry) will be presented.

To a certain extent, the color effects reported here can be related to the reflective DID effect described earlier [45]. In DIDs, visible light is diffracted to very steep angles. This light hence is not present in the zero order reflection visible to the observer. The color effects described in the following share this property with DIDs: Efficient diffraction "removes" certain wavelengths from the observed zero order transmission spectrum, which leads to a visible color. On the other hand, there are some key differences between the two effects: The present structures work in transmission and are asymmetric upon rotation by 180° instead of 90°. Further, when using a non–collimated light source, it is possible to recombine the zero order with first order colors and create unexpected optical effects. It is for example possible to produce a color effect with four different, orientation-dependent appearances, which could be of great interest for security applications. The utilization of a flexible substrate on the other hand enables creation of a colored, floating image. This eye–catching effect could find applications not only in security, but for example also in decoration or marketing in combination with light emitting devices such as mobile phones and tablets.

Since the color effects reported in the present work not only rely on zero order transmittance (T0) but also ±1st orders transmittances (T1/T−1), I would like to revisit equation [2−1]. As asymmetric gratings are considered, the sign of the incident angle θ_i is important and must be chosen as shown in Figure 38 (b), following grating standards, as defined for example in [216]. Throughout the rest of this section, the color code shown on this image will be kept for T0, but not for the ±1st order. Indeed, the problem when labeling the diffraction orders according to the general convention is that optical paths linked through reciprocity do not hold the same name when coming from either side of the grating surface. It was shown in the previous section that T1 as labeled in Figure 38 (b) shows a very high efficiency (holds for all the relevant angles of incidence, data not shown). On the other hand, the opposite is true for T−1, which is well below 10% at any angle and wavelength. The reciprocal rays are of course diffracted with the same efficiency, but the naming of their order should be switched. Throughout the rest of this section, I will therefore refer to the orders as the "high efficiency order", $T1_{hi}$, and the "low efficiency order", $T1_{low}$, as depicted in Figure 38 (c).
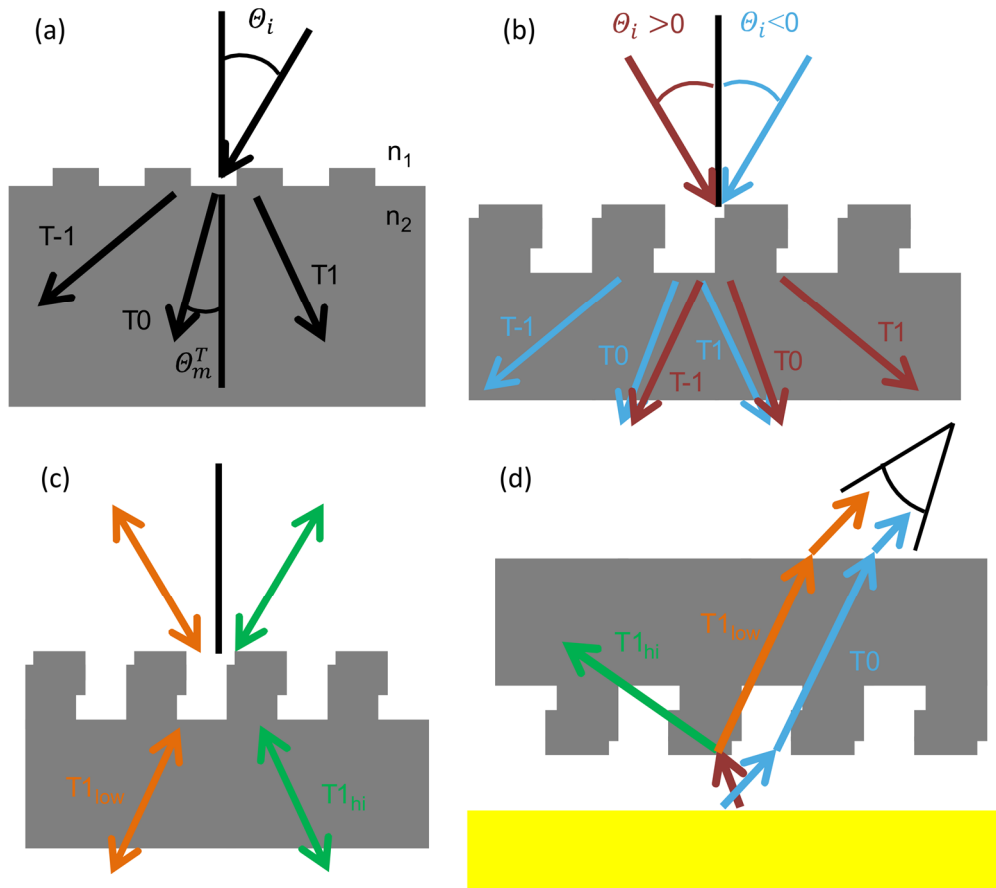
Figure 38. (a) Schematically shows the propagation directions of 0 and ±1st diffracted orders inside a medium with $n_2 > n_1$ after having passed an arbitrary grating interface, (b) illustrates the choice of sign and color code for the incident angle with respect to the metallization. The resulting diffracted orders and how they combine are also shown. (c) Depicts the reciprocity of the diffracted orders and their labeling based on the transmitted intensities (d) Visualizes how T−1 and T0, coming from different parts of an extended light source, can form a mixed color as visible to the observer.

One important feature already becomes visible in Figure 38 (b): T0 stemming from light e.g. incident at negative angles ($\theta_i < 0$, blue arrows) can be refracted into the same angle as light diffracted from positive angles ($\theta_i > 0$, red arrows T−1). This is an important mechanism when considering extended light sources like e.g. a display or other flat panel light sources that radiate into a large solid angle. To illustrate this fact, let us consider a numerical example for green light (530 nm) and a grating with a $\Lambda = 440$ nm period. We further assume that we want green T−1 light to become visible at e.g. $\theta_{-1}^T = -40°$ after passing the sample together with the T0 light, as sketched in Figure 38 (d). Snell's law indicates that the refracted T0 light will travel at an angle of approx. −25° inside the glass. Considering a ray coming from the air side (red arrow in Figure 38 (d)), we set $n_1 = 1$, $n_2 = 1.5$, $\Lambda = 440$ nm, $\lambda = 530$ nm and $m = -1$. Equation [2–1] yields $\theta_{-1}^T = -25°$ for an angle of incidence $\theta_i \approx 35°$, which is what we searched for. The same can be done for any other wavelength in order to find all the incoming light that is diffracted to $\theta_{-1}^T = -40°$ (alternatively, we could of course have considered the reciprocal ray incident at $\theta_i = -40°$ from the back side). At an angle of observation of $\theta_m^T = -40°$, the T0 light is therefore visible simultaneously with light impinging onto the grating surface at different angles (and hence coming from different parts of the light source) that is diffracted into T−1. Figure 39 illustrates the effect of higher order diffraction on the color as visible on an actual sample: When the substrate is far enough away from the light source, the angles of incidence θ_i are limited to

negative values and no light is diffracted towards the spectator. The visible color is purely T0 and appears blue in the present example. By moving the sample above the light source (from left to right in Figure 39), $\theta_i > 0$ can be achieved and T0 will mix with T$_{hi}$, which results in a greyish color.
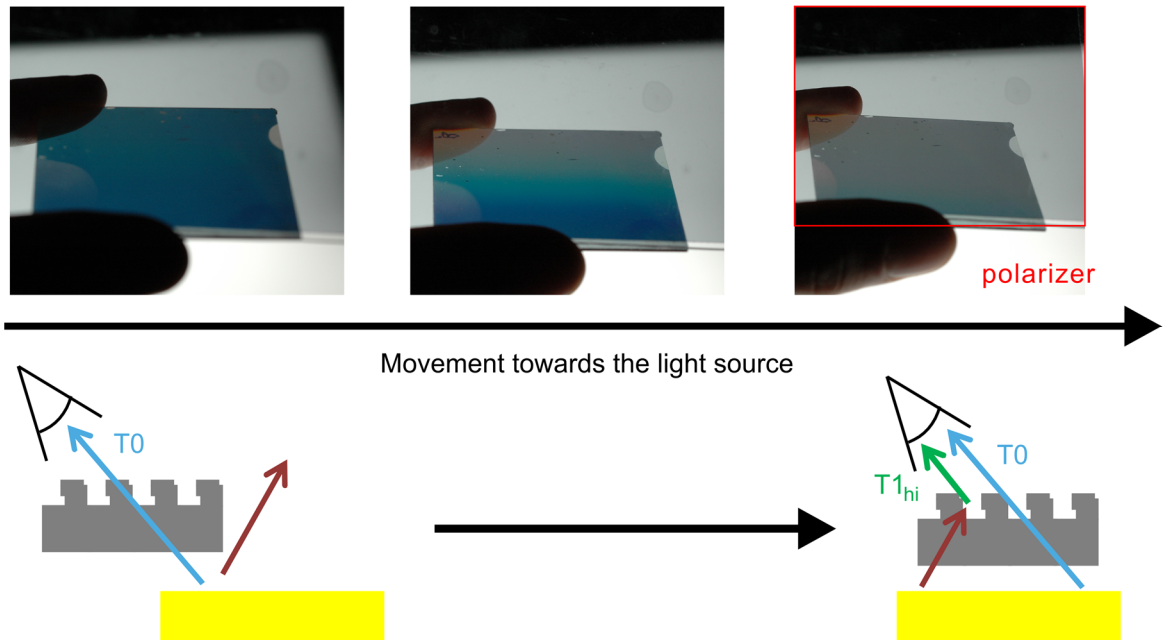
Figure 39. Illustration of the effect of T1 on the visible color: Moving the structure above the light source allows for T1 to appear and change the visible color from blue to grey.

The best known transmission color effects reported in literature are zero order transmission effects, which will be considered first for the present structures. Since, we are interested in color effects that are asymmetric with respect to rotation or tilt of the structure, we require seeing color effects at an angle. For this purpose, a grating with a $\Lambda = 440$ nm period and $t = 250$ nm depth was evaporated with $D = 20$ nm Al at an angle $\alpha > 60°$ and subsequently spectrally characterized for both polarizations (Figure 33 (b) illustrates the evaporation procedure as well as the definition of polarizations) at angles between −60° and 60° (Figure 40).

The spectra show several distinct features for both polarizations. They lead to strong color differences between them, which are visible to the naked eye (see inset photos in Figure 40). The spectral features of TM polarized light are mainly located outside of the visible wavelength range (resulting in a greyish color) as can be seen in Figure 40 (a), whereas the opposite is true for TE polarized light, Figure 40 (b). The difference between positive and negative angles is very strong for TE polarized light, with e.g. a drop from around 55% of green/orange light transmittance at 20° to around 5% at −40°. Figure 40 (c) illustrates this further: by dividing the transmittance spectra recorded at $+\theta_0^T$ by those recorded at $-\theta_0^T$, the resulting "asymmetry ratio" reaches a value of 9 for visible wavelengths. Hence, the structure is 9 times more transparent for certain wavelengths when looking at it from positive angles than from the corresponding negative angles.
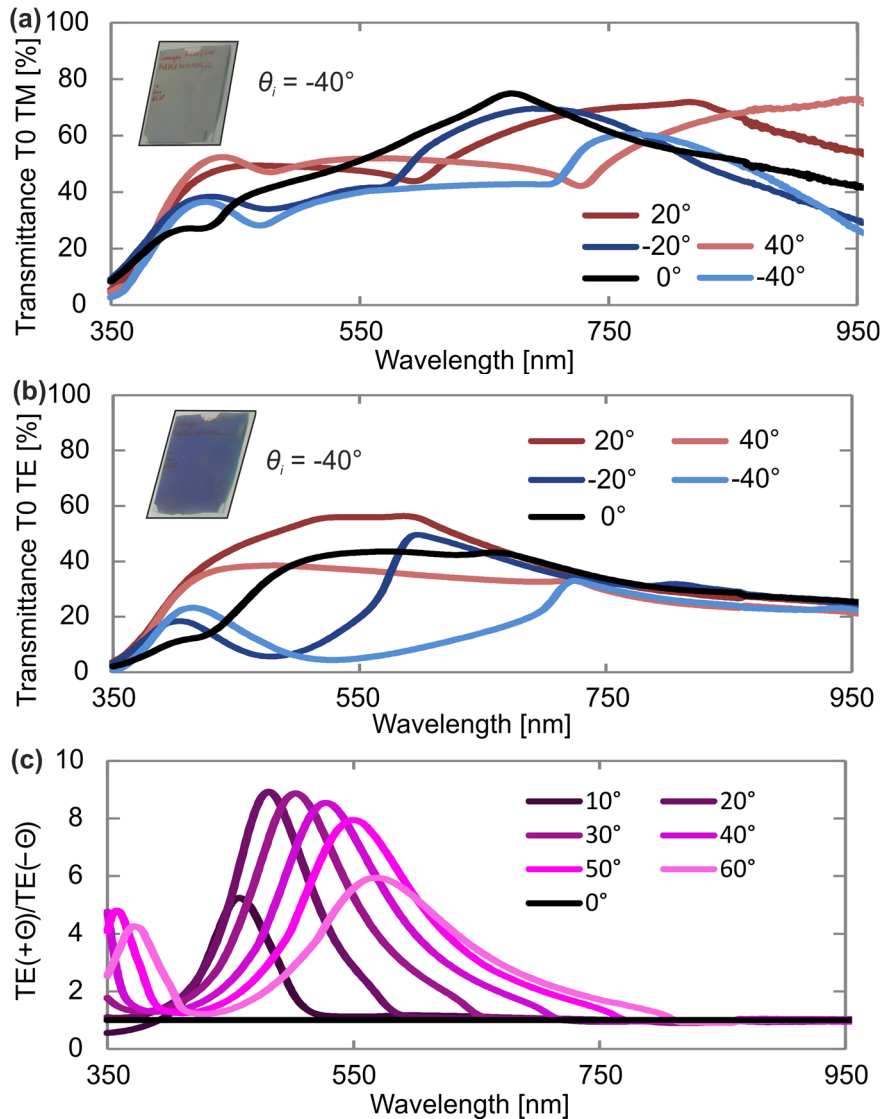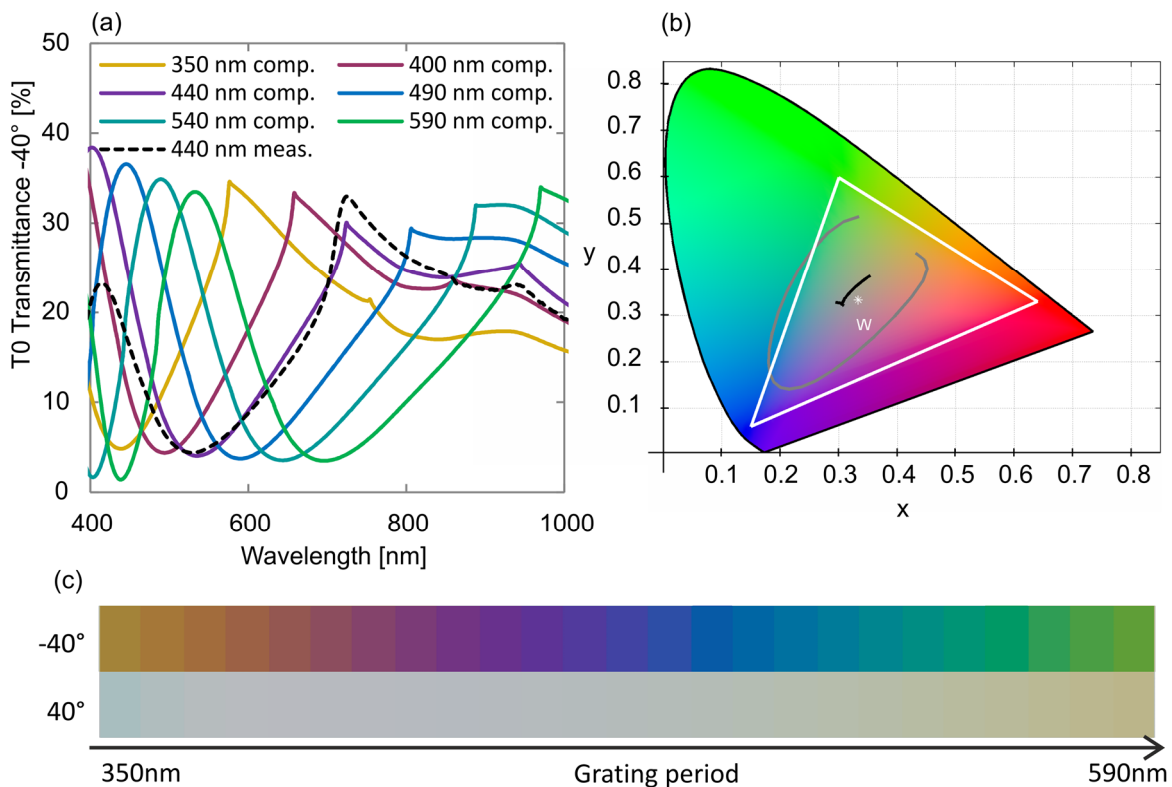
Figure 40. Measured zero order transmittance spectra of (a) TM polarized light and (b) TE polarized light are measured on a 440 nm period grating evaporated with Al at $\alpha > 60°$. The insets show photos of the measured sample under accordingly polarized white light illumination and an angle of $\theta^T = -40°$. The "asymmetry ratio" shown on graph (c) is defined by the transmittance of TE polarized light at $+\theta_i$ divided by the transmittance of TE polarized light at $-\theta_i$ for each wavelength.

It might appear obvious by simple geometrical considerations that more light is blocked/absorbed when the ray is incident onto the metallized side ($\theta_i < 0$) of the structure; however, this is not the correct explanation for this asymmetric response. As mentioned, this kind of grating shows a very high T1 diffraction efficiency at any angle, reaching a peak at the wavelength around the Wood–Rayleigh anomaly, which is at $\lambda = \Lambda = 440$ nm for the sample under study at perpendicular air incidence. When tilting the grating, the T1 peak moves either into the UV (for $\theta_i > 0$) or into the visible (for $\theta_i < 0$). The large dip in T0 at negative angles is caused by exactly this redistribution of light into the higher order mode. Also visible in the TE spectra is the increasing reflection at steeper angles, also reducing the transmittance for positive and negative angles (due to reciprocity). Towards the infrared part of the spectrum, the metallized grating starts to behave like a wire grid polarizer, resulting in high TE reflectance and high TM transmittance. It is finally worth mentioning that for TE polarized light, which shows much stronger coloring in the present study, no surface plasmon resonances are excited [217].

Color effects are rarely reported for this polarization [163] although they could be combined with plasmonic resonances in the same structure and hence form strongly polarization depend-dependent colors.

Numerical simulations were performed for TE polarized light using the geometry shown in Figure 33 (e). The simulated T0 data (violet line in Figure 41 (a)) fit the measurements (dashed line) very well for the 440 nm period sample illuminated at $\theta_i = -40°$. The only exception is found at wavelengths below 470 nm, where the UV–curable polymer starts to absorb.

By increasing period and depth of the base grating by the same factor, the T0 maxima situated at around $\lambda = 420$ nm and $\lambda = 730$ nm for the $\Lambda = 440$ nm period grating can be shifted to longer or shorter wavelengths, while the shape and height of the peaks are almost preserved. The resulting RGB colors under daylight illumination (D65) computed for $\pm 40°$ angle of view are shown in Figure 41 (c). With this palette of colors available it is straightforward to create colorful images at $\theta_i < 0$ that are hardly visible at $\theta_i > 0$ (only grey/brownish colors are observed in that latter case). Note that only TE polarized zero order transmittance is considered. This corresponds either to illumination with a very distant or collimated light source (such as e.g. the sunlight) or the configuration in Figure 38 (d), where $T1_{low}$ can be neglected. It also requires the addition of a simple polarization filter, which is commercially available in large quantities at low prices.


Figure 41. (a) Computed zero order transmittances at $-40°$ TE polarized incidence are shown for gratings with different periods (colored lines). The measured 440 nm period grating (dashed line) served as a basis and was equally scaled in period and depth for the series. Metallization parameters such as evaporation angle and thickness are kept constant for the simulations. The resulting colors for $\theta_i = \pm 40°$ incidence of TE polarized daylight are calculated for periods between 350 nm and 590 nm and represented in (b) a *xyY* color plot (grey: $-40°$, black: 40° angle of view) and (c) RGB colors.

It is worth emphasizing that the metallization parameters (thickness and evaporation angle) are the same for all the simulations in Figure 41 (the metal height on the sidewall h was scaled according to the period). It is therefore possible to receive all of the above colors on one sample by using a single replication step (using a master consisting of gratings with different periods and depths) followed by one single evaporation step.

In order to illustrate how the achieved zero order colors compare to other systems, the computed xy data for $\theta_i = -40°$ (grey) as well as $\theta_i = 40°$ angle of incidence (black) is plotted in the chromaticity diagram (Figure 41 (b)). All the colors enclosed by those curves are available for fabrication (e.g. through pixelation). We can immediately confirm that a variety of colors are perceivable at $\theta_i = -40°$ angle of view but only a narrow range is available at 40°. By comparing the simulated colors at −40° to the sRGB gamut (colors e.g. available to standard LCD screen, white triangle in Figure 41 (b)) we see that the blue and green color availability is close to or even better than sRGB, but strong red hues are problematic. By releasing some constraints (like e.g. constant evaporation parameters), further improvements should be possible, but such refinements go beyond the scope of the present thesis.

It is now experimentally shown, how a single evaporation can create two completely different colors on the same sample by patterning gratings with $\Lambda = 440\ nm$ and 350 nm periods into a "CSEM" shape and subsequently evaporating them with 20 nm Al at an angle $\alpha > 60°$. The two gratings are predicted to show purple and orange colors, respectively, in zero order transmission at −40° angle of view which is confirmed by experiments. As established earlier, T0 accounts for the color visible in the orientation shown in Figure 38 (d) and the top left photo in Figure 42 corresponds to this exact orientation. Rotating or flipping the device as indicated by the arrows will result in a well visible color change, leading to 4 different, orientation-dependent appearances. This switching happens due to the previously discussed mixing of T0 with either $T1_{hi}$ or $T1_{low}$ as sketched in Figure 42. The high, asymmetric diffraction efficiency serves here the double purpose of removing light from T0 as well as becoming directly visible to the observer in two of the possible configurations.
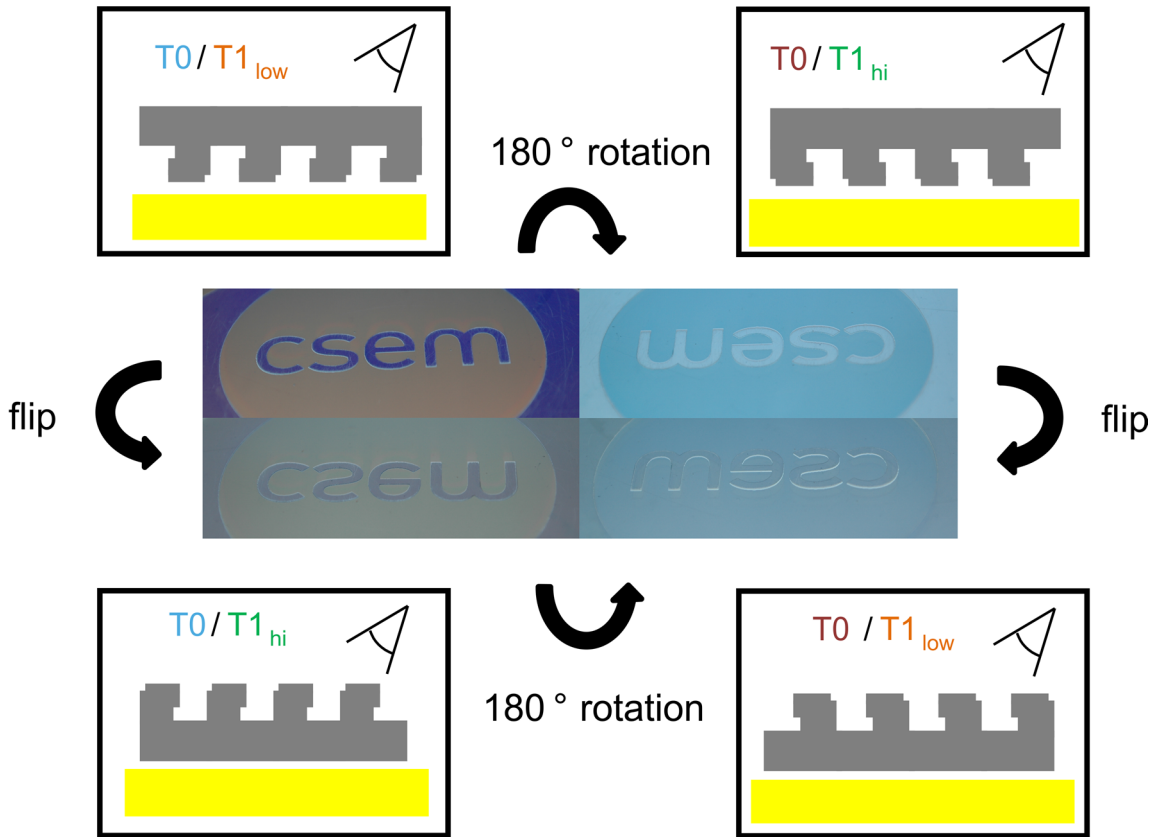
Figure 42. TE polarized photographs of a sample containing a 440 nm (letters) and a 350 nm period grating (surrounding circle) are shown together with sketches illustrating the orientation they were recorded at. By flipping or rotating the sample, different mixtures of zero (T0 at $\pm\theta_i$) and higher transmission orders ($T_{hi/low}$) are obtained.

It is worth noting that the simulated colors for a 40° angle of view match the bottom right image where T0 is mixed with $T1_{low}$. The contrast between the two gratings is very low, as expected, and the CSEM logo is almost invisible apart from the white outline, which stems from the height difference between the two gratings and could be avoided by using a more sophisticated grating master. This kind of structure would therefore be very well suited for security applications, for example in bank notes.

Let us finally note that the colors are also similar and well visible under non–polarized illumination, although they are less saturated due to the addition of mostly uncolored TM polarized light. The addition of a commercial polarizer foil does not greatly increase the costs of the device and could also serve as a protective layer.

4.3.1 Floating Image Effect

Until now, only gratings in close contact with the light source were considered, which led to a mixing of T0 and T±1. By using a mask on the light source and moving the grating far enough away from the light source, the directly transmitted rays can be separated from the diffracted ones as depicted in Figure 43 (a) and (d). In the present experiments, a commercial smart phone displaying a white CSEM logo was used as a masked light source and the four dots were left uncovered in all photos for comparison. A floating image will then appear at the position of the grating surface and the directly transmitted picture will stay visible at the old position. By choosing a flexible substrate for the grating, such as Polycarbonate, it is also possible to create curved floating images, Figure 43 (b), (c) and (e). The use of such a substrate also nicely evi-

dences the transition from the mixing regime to the floating image regime, which corresponds to the continuous change from the letters "c" to "m" in these photos. It is important to mention that the structure needs to be oriented such that $T1_{hi}$ is diffracted towards the observer. Figure 43 illustrates the two possible orientations: in panel (a) the grating faces the observer, which shows stronger colors; whereas in panel (d) the grating is on the side of the light source, leading to a higher overall transmittance (compare Figure 43 (b) to (e)). Colors are even partially tunable by adjusting the angle of view, as illustrated by the three pictures in Figure 43 (c). Grating or evaporation parameters can also easily be tuned to generate a variety of color combinations. Finally, the color of both images is strong enough to even be visible in ambient light (Figure 43 (b)), only the reflected orders may disturb the visibility. By choosing a stronger light source than the mobile phone used for Figure 43, visibility of the two images can also easily be further improved. Under dimmed illumination, reflections are excluded and the colored shapes are always perfectly visible.
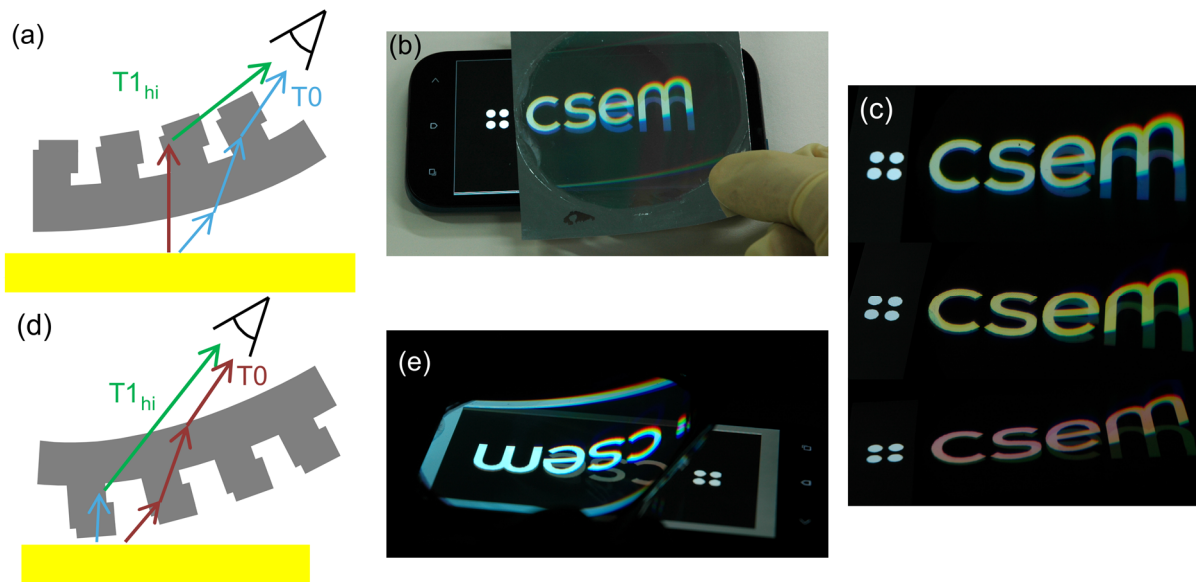
Figure 43. (a) Sketch illustrating how a floating image becomes apparent for $\theta < 0°$, the configuration used for photos (b) and (c). (d) Depicts the same for the $\theta > 0°$ case and photo (e). Note that (b) reveals the setup used for taking all of the photos and proves appearance of the floating image even in ambient light. The sample used is a hot embossed, flexible Polycarbonate grating of 560 nm period, evaporated with Al at $\alpha > 45°$.

The presented optical effects would be very well suited for incorporation into the increasingly popular polymeric banknotes. The transparent parts of these banknotes could easily be patterned with the proposed structures, as they already contain holograms which are based on a very similar fabrication process. Another potential application of this effect could be brand protection or simply decoration of mobile phones and tablets. Since the light emitting layer of the phone is already covered by glass with a certain thickness, only a small additional spacing is required in order to achieve a floating image. It would therefore be possible to incorporate the structure into the device wrapping (when sealing it at the factory) for brand protection or mount it in on showcase (e.g. for presentation in a store). Another convenient property of many mobile phones is that they already emit partially polarized light, which enhances the visual effect through the use of mainly TE polarized light.

4.4   Conclusion

In conclusion, efficient 1st order transmittance coupling was enabled by coating simple, symmetric basic gratings through oblique deposition of a high refractive index material or metal. For a structure optimized for unpolarized light, around 70% of the perpendicularly incoming green light was diffracted into T1 according to the measurements. Standard replication techniques such as hot-embossing and UV casting were used together with physical vapor deposition. An important property of such a structure is that it retains its high efficiency in the presence of a possible cladding layer.

By using metals instead of dielectrics, I demonstrated easily tunable, asymmetric colors. Although diffraction is considered an "old" technology, to the best of my knowledge it was never used for generating combined zero and higher order color effects in transmission. I could showcase several possibilities of doing so, ranging from asymmetric color effects to floating images, which are capable of generating a 3D-like effect. Applications of these optical effects include security or decorative features for bank notes or light emitting devices such as mobile phones. This approach fits also very well with mass-production, since the entire fabrication can be performed in a roll-to-roll process. Even generation of entire, colored images can be performed in a two-step process consisting of one imprint step and one angle evaporation step.

Chapter 5   Fano–Resonances in periodic nanostructures

5.1   State of the art

The interest in plasmonic resonances in metal nanostructure arrays rose rapidly after Ebbesen *et al.* reported on the extraordinary optical transmittance through periodic nanoholes in 1998 [72]. A hot debate on the exact mechanism leading to this phenomenon sparked in the following [218]–[220]. Together with the general excitement about the opportunities plasmonic nanostructures could offer (metamaterials for cloaking and superlensing, nanoparticles for biological applications or near field enhancement in general for photovoltaics), this led to a steep increase in published work in this field (Figure 44).
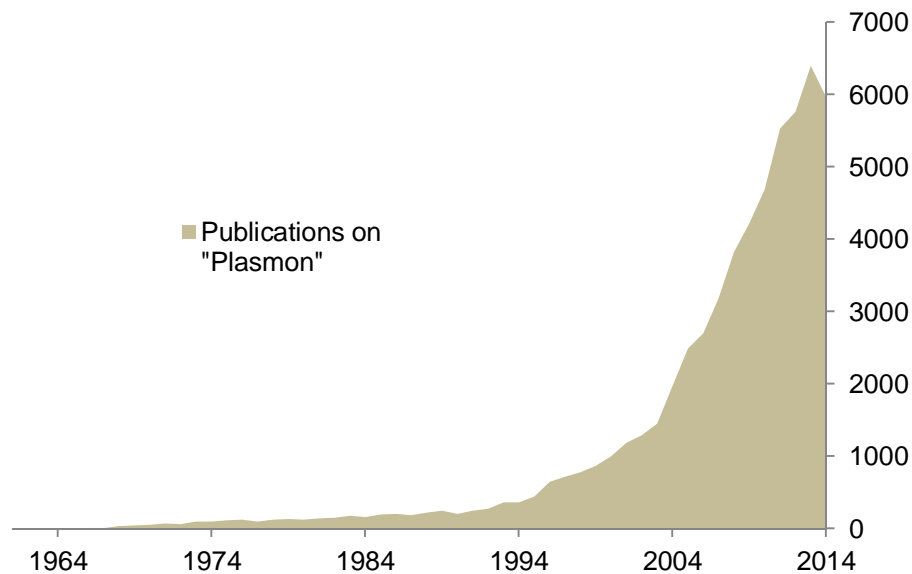
Figure 44. Number of Articles per year found for the keyword "plasmon" on Scopus.

Various different systems and fabrication methods were considered for obtaining plasmonic nanostructures. As reviewed in Section 3.1.1, many of them rely on EBL patterning of subwavelength structures with disk, rod, or triangular shapes. Since it is impossible to cover all of the existing structures and resonances discovered, I will focus on the work performed on metallic 1D gratings. Fano–resonances will then be introduced as a particular kind of interaction between different plasmonic modes.

5.1.1   Plasmons in 1D periodic structures

In order to excite plasmonic resonances in 1D gratings, the polarization of the incident electric field has to be perpendicular to the grating lines (TM or p–polarized light in classical mount and TE or s–polarized light in conical mount [216]). This configuration provides confinement for the

charges, which is necessary for LSPRs to occur, as well as a suitable orientation of the electric field vector for launching SPPs (compare to Section 2.2.2). Remember that LSPRs are spatially confined to the nanostructure they are excited in, whereas SPPs travel along the surface and dissipate their initial energy in the process. For more detailed descriptions of these modes the reader is referred to Sections 2.2.1 and 2.2.2 respectively. When launching SPPs with a grating instead of a prism, a degree of freedom is added: The excitation wavelength depends on the grating period and can therefore be controlled accurately, which is not possible otherwise. For perpendicular incidence, this wavelength can be calculated by [104]:

$$\lambda_{SPP} = \frac{\Lambda}{m} \sqrt{\left(\frac{\varepsilon_d \ \varepsilon_m}{\varepsilon_d + \varepsilon_m} \right)},$$ [5–1]

where Λ is the grating period, m an integer (the order) and ε_d and ε_m are the permittivities of the dielectric and the metal respectively. Consequently, the tuning of periodic metal structures for efficiently launching SPPs for sensing or waveguiding has received a lot of attention [215], [221]. In that vein it is also important to note that no continuous film is required to support the SPP, they can also propagate in disconnected wires as illustrated in Figure 45. This fact has already been reported before Ebbesen's discovery (e.g. Lochbihler in 1994 [222]). Such SPPs play a key role in the transmission properties of metallic gratings. Enhancement [223] as well as detrimental influence [219] on the transmission efficiency have been reported. The current consensus is that the result strongly depends on the grating parameters (especially the distance between the apertures), as they determine whether the phases of the SPP and the incoming field match at the positions of the apertures [224], [225].
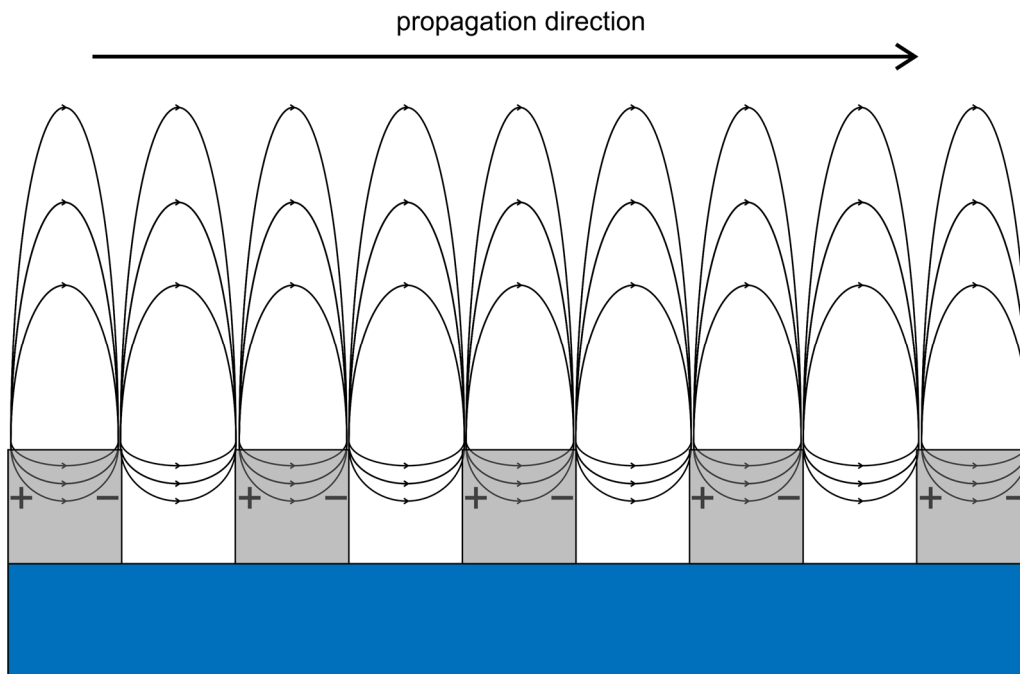
Figure 45. Horizontal surface plasmon polaritons excited in a metallic grating.

A second class of plasmonic resonances typically considered in metallic gratings is the so called vertical SPP, cavity mode (CM) or gap mode. As depicted in Figure 46, these resonances are confined to the sidewalls of the wires and hence are usually considered to be LSPRs. They are reflected at the top and bottom ends of the wire/gap and thereby form a standing wave, which is

why they are also oftentimes referred to as Fabry–Perot modes [226]. It is well understood that they are important to the EOT effect [223] and the optical response of metallic gratings in gen-general. Although they have predominantly been reported for narrow grooves, they are not limited to such slits and various geometries have been investigated in 1D as well as 2D gratings [227], [228].
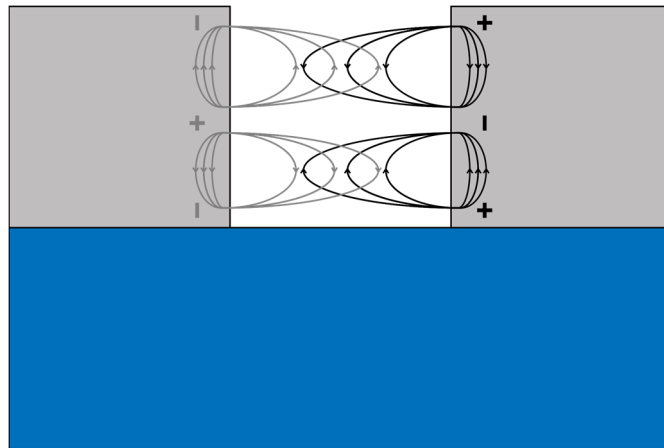
Figure 46. Vertical surface plasmon polariton excited in a metallic grating (also called cavity mode, CM).

More recent descriptions of optical phenomena in metallic gratings also consider dipolar charge distributions that can form at the cavity entry. They can be amplified or even generated by SPPs and radiate into the cavity to excite a CM [225]. Other researchers studied quasi–cylindrical waves and found that they can account for a significant portion of the transmittance enhancement in EOT. They therefore complement the SPP explanation in an important way [229]. Individual wires can also exhibit a particle–like behavior as the electrons are confined in at least one dimension. Various wire shapes and their near–field responses have therefore also been investigated [230]. It is finally worth noting that the near–field enhancement close to the slits or holes can be substantial, which makes these systems attractive for sensing [231], [232], photodetection [233] and photovoltaics [234].

This summary on the phenomena reported on metallic gratings introduced the most important concepts, for a more exhaustive treatment of the subject the reader may e.g. refer to reference [235].

5.1.2   Fano–resonances

The name « Fano–resonance » honors Ugo Fano, who worked on asymmetric lineshapes, which he observed in the inelastic scattering spectra of helium atoms [19]. A general requirement for obtaining Fano–lineshapes is the interaction of a narrow state with a broad continuum of states. This characteristic can also be obtained in plasmonics, where spectrally broad, (often radiative) resonances are designed to interact with sharp (often subradiant) modes [236]. The result is a broad maximum/minimum with an asymmetric, narrow minimum/maximum. Fano–interferences can be observed in transmission as well as reflection. Often, near–field exchange between a dipolar and a higher order, non–radiative mode like e.g. a quadrupole is utilized [237]. More recently, radiative modes have also been shown to hybridize with each other and form superradiant as well as subradiant modes [20]. These hybrid modes can then exhibit typical Fano–lineshapes, provided that they overlap spectrally and oftentimes, the spectral position of the modes can be tuned by controlling geometrical parameters [238].

Another possible constituent of Fano–resonances is the Wood–Rayleigh (WR) anomaly dis-discussed earlier [239]. Popular Fano–resonant plasmonic systems include split–rings [240], [241], dolmen structures [237], [242], few–particle clusters [243], and gratings [244]–[246].

Analytical models for Fano–resonances in plasmonic systems have e.g. been developed by Gallinet *et al.* [247] and can give valuable insights into the underlying mechanisms. The frequency dependent reflectance $R_b(\omega)$ of a plasmonic nanostructure can be described by the following Lorentz function:

$$R_b(\omega) = \frac{a^2}{\left(\dfrac{\omega^2 - \omega_s^2}{(W_s + \omega_s)^2 - \omega_s^2}\right)^2 + 1}\,, \qquad [5\text{--}2]$$

where a is the maximal amplitude, ω_s the resonance frequency and W_s the spectral width. The lineshape of a Fano–resonant system $\sigma(\omega)$, consisting of a bright and an additional dark mode, is given by:

$$\sigma(\omega) = \frac{\left(\dfrac{\omega^2 - \omega_a^2}{(W_a + \omega_a)^2 - \omega_a^2} + q\right)^2 + b}{\left(\dfrac{\omega^2 - \omega_a^2}{(W_a + \omega_a)^2 - \omega_a^2}\right)^2 + 1}\,, \qquad [5\text{--}3]$$

where ω_a is the center frequency, W_a the spectral width, q the asymmetry parameter and b the damping parameter. The total reflectance $R(\omega)$ of the Fano–resonant system can then be calculated with:

$$R(\omega) = R_b(\omega)\sigma(\omega). \qquad [5\text{--}4]$$

Examples with the parameters $a = 1$, $\omega_s = 1.2$, $W_s = 0.1$, $\omega_a = 1.1$, $W_a = 0.03$, $q = -0.2$, $b = 0$ for the pure Lorentzian (dashed line) as well as the Fano–resonance (solid line) are given in Figure 47. Varying the parameters allows visualization of the influence they have on the resonance and helps designing plasmonic structures. For example, proper arrangement of the resonance frequencies is crucial as well as minimizing losses. For the latter, the parameter b can e.g. be deduced from fitting measured data and can help finding optimal structures [1].
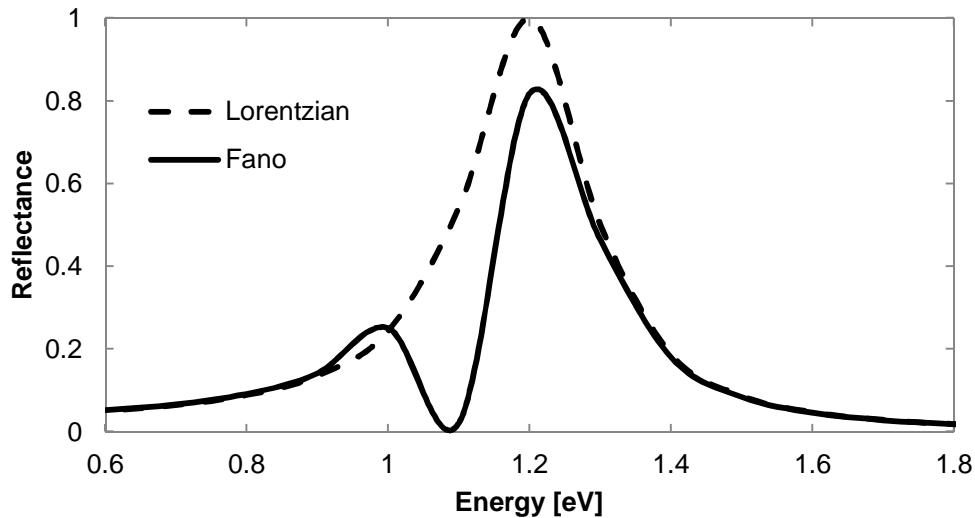
Figure 47. Comparison of a Lorentzian to a Fano lineshape.

The Fano–lineshape exhibits much sharper spectral features than the undisturbed plasmonic resonance and is therefore preferred for applications like sensing [248] or optical switching [249]. The asymmetric lineshape shows a steeper slope than the typically prevalent Lorentzian curve, which results in a stronger signal change when e.g. the resonance position is shifted in response to a stimulus. Color effects can on the other hand also profit from Fano–interferences as the spectrally sharp response leads to more saturated colors [22].

The possibility of achieving strong near–field interactions and sharp spectral features simultaneously motivates the application of plasmonic Fano–resonances for colorimetric/visual sensing. The combination of optical effects with sensing is a promising field of research, as it allows easy detection of potentially complex processes. In this vein, Yanik *et al.* [23] e.g. achieved detection of a biomolecular monolayer on a hole array with the naked eye. Visual strain or pressure sensing with so called "plasmon rulers" has also been proposed by several researchers [21], [250], [251], but no industrially viable fabrication approach has emerged yet. CSEM (and in particular the Integrated Sensing group where this thesis was performed) has recently been active in colorimetric (gas) sensing [245], [252] and possesses the facilities for up–scalable production, which makes large–area strain sensing a very attractive option to explore. Such sensors would be completely passive and could be read out at a distance, which is for example very attractive for applications in civil engineering [253].

To that end, a particular class of nanowires having the shape of a split–ring resonator (referred to as U–shape in the following) will be explored theoretically as well as experimentally. In the past decade, such nanowires have been used for investigating EOT effects in gold gratings [254] or for Surface Enhanced Raman Scattering (SERS) [132]. Several theoretical studies have also investigated the role of WR anomalies, various surface plasmon polaritons (SPPs), or CMs in the optical response of U–shaped wires [255]–[258]. It has further been shown that such wires exhibit Fano–resonances, which can be very sensitive to the spacing between the wires [1], [226]. These reports are however based on very short–period gratings with a gold coating, which are not suitable for cost–efficient large area fabrication. The transition to larger structure sizes and aluminum as the plasmonic material would however allow transferring this technology to low–cost, high–throughput production with e.g. roll–to–roll manufacturing [184], [259]. It requires investigation of the distinct plasmonic modes in this altered structure though, which will be done in the next section of this chapter. For that purpose, gold and aluminum

wires will be treated side by side and monitoring the main differences between the materials will help elucidating the dynamics between the modes. Near–fields and charges are investigated in detail to corroborate the findings. Production line compatible ways for tuning the resonance position and shape on the fly are presented experimentally and compared to theoretical models. The resulting structure not only shows a distinct color, but is also sensitive to the surrounding medium and the spacing between neighboring wires. All of these insights are finally combined to create a strain sensor, which responds to elongation with a well visible color change.

5.2   Fano–resonances in U–shaped wires

For investigation of the resonances present in U–shaped nanowires suited for industrial production, a UV–embossing process in Ormocer® (Micro Resist Technology GmbH) was used together with shadow evaporation. A binary grating of $\Lambda = 350$ nm period, $d = 200$ nm depth and $w = 0.3\,\Lambda$ (see Figure 48 (d)) is replicated on a 3 inch edge length, square glass. Aluminum or gold was evaporated from both sides of the grating at the same angle α with respect to the surface normal (perpendicular to the grating lines (Figure 48 (b)) to form U–shaped wires (SEM image, Figure 48(c)). The evaporation angle was varied between $\alpha = 52°$ and $\alpha = 68°$. The evaporated material thickness as set on the machine (D) was varied between $D = 35$ nm and $D = 95$nm for each side (this is the value referred to throughout the chapter). The structure is subsequently embedded in a polymer matrix to protect it from wear. This also simplifies the investigated resonant system, since the refractive indices of the substrate and the superstrate are matched.

The simulation model for RCWA calculations is shown in Figure 48 (d). The refractive index of the surrounding medium (incident as well as substrate) was assumed to be 1.5, data for aluminum were taken from reference [213] and the optical constants for gold were adapted from reference [260]. The geometrical parameters are: $\Lambda = 350$ nm and $w = 0.3\,\Lambda$. The thickness of the evaporated Al was measured on the sample and used as an estimate for t (reduced by 5–10 nm due to the native oxide layer). The thickness on the sidewalls can then be calculated by $s = D \sin(\alpha)$ through geometrical considerations. From the thickness as set on the evaporator, t can also be calculated with $t = \cos(\alpha)\,D$. For the height of the sidewall coating h, an approximate value can be obtained with $h = \tan(\alpha)\,(\Lambda - w)$. One has to keep in mind that this value is quite accurate for the evaporation from the first side, but during the second evaporation, the already deposited metal will increase the shadowing effect and therefore cause h to be shorter on this side. This effect was accounted for by decreasing h compared to the above calculation by 5–15 nm (depending of the metallization thickness) but keeping the structure symmetric for simplicity. The SEM image in Figure 48 (c) finally also shows rounded corners, which inspired the missing corner pieces of width $s/2$ and height $t/2$ for the RCWA simulations.

The model for surface integral equation (SIE) simulations contained slanted facets instead of the missing corner piece, which is a more accurate representation of reality but not available with RCWA (which requires layered media as an input). The simulations are in close agreement for both methods.
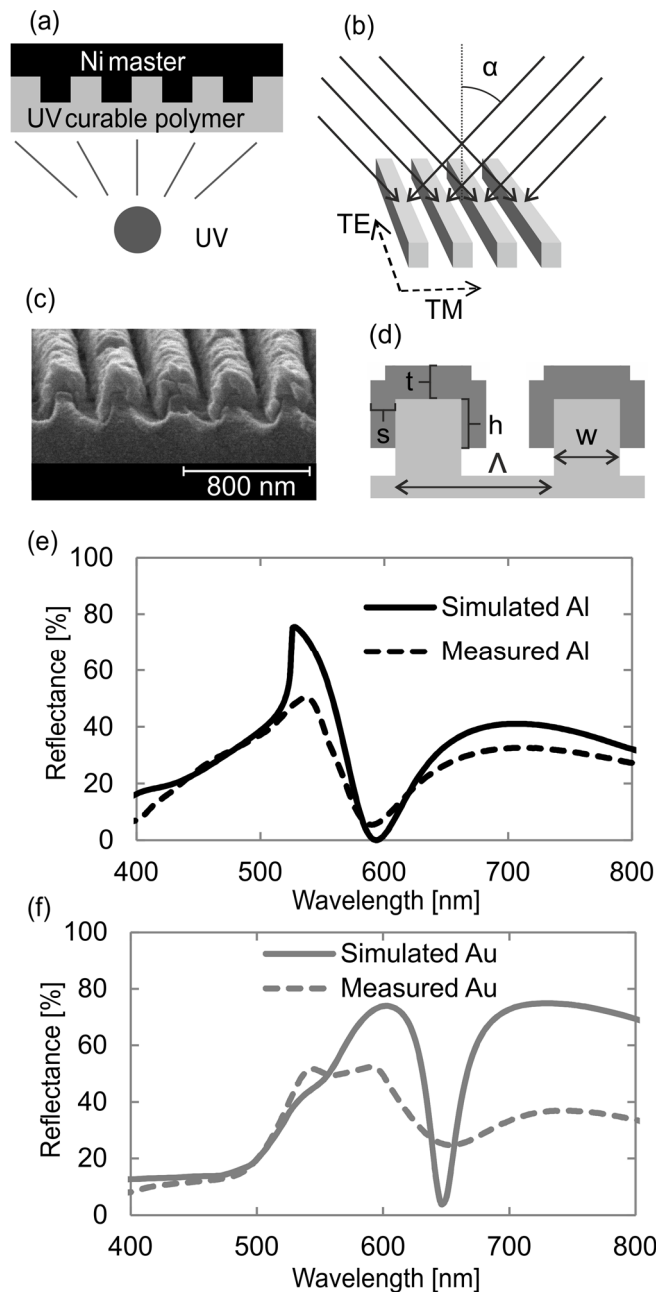
Figure 48. The fabrication procedure consisting of (a) UV embossing and (b) double evaporation of metal at an angle α is shown together with (c) a SEM picture of the resulting nanostructures (aluminum) and (d) the corresponding model used for RCWA simulations. The resulting, measured spectra for TM polarized light are plotted for (e) aluminum and (f) gold, together with the according computations.

In order to obtain a Fano shaped resonance, at least one superradiant ("bright") mode has to be combined with one subradiant ("dark") mode. The former can for example be a radiative plasmonic resonance such as an oscillating dipole. The latter needs to have non–radiative properties, which motivates resonators supporting quadrupolar charge distributions as popular choices. As recently described by Lovera *et al.* [20], both of these modes can also occur when two bright resonances are hybridized. Typically, dipolar in–plane modes are utilized for this purpose since they are obtained in rod or disk shaped structures. Here, the modes of choice are a propagating surface plasmon polariton (SPP) and a localized plasmonic mode. The SPP is excited on the top surface of the metal grating (horizontal SPP). The localized mode is excited by resonating surface plasmons at the sidewalls of the metal structure (vertical SPPs, also called

gap or cavity modes [226], [261]). Vertical SPPs have been the subject of extensive studies often linked to the EOT effect described by Ebbesen *et al.* in 2D hole arrays [72]. It is worth noting that in one dimensional gratings, different transmission mechanisms can occur and e.g. no coupling between the SPPs modes on the top and bottom surfaces is required [223], [227]. In contrast to the majority of research in this area, the present structure is aimed at creating a strong response in reflection instead of transmission, which is especially advantageous for visual applications under ambient lighting.

Transverse magnetic (TM) polarized reflection spectra of the fabricated aluminum nanowires reveal a pronounced Fano-resonance, which is red–shifted and more damped for gold (90 nm of metal evaporated at α=56°, dashed lines in Figure 48 (e) and (f)). When we compare the spectra to computations (solid lines) performed on the model from Figure 48 (d) with parameters deduced from the SEM image, we obtain very good spectral alignment for the different features. The fabricated aluminum structure also shows a very strong spectral modulation, whereas the resonance is attenuated and broadened for the gold wires. This can most likely be linked to the increased absorption of gold at visible wavelengths, which is amplified by the presence of fabrication imperfections. Imperfections and absorption reduce in turn the modulation of the Fano–resonance and broaden the features. Because of this attenuation, the WR anomaly around $\lambda = 525$ nm is also more visible in the measurement than in the simulation, where it only appears as a shoulder [238]. Due to the thermal evaporation process, both materials can also suffer from altered optical properties when compared to bulk values found in the literature; the corresponding defects (e.g. granularity and roughness) could be possibly improved [176].

In order to explain the involved modes, I start with gold, which is the most explored plasmonic material and particularly popular for biosensing applications. Figure 49 shows the far–field spectra of such U–shaped nanowires, together with near–fields and charge maps at specific spectral positions. The short wavelength end of the observed Fano–resonance (Position 1, around $\lambda = 600$ nm) is in the vicinity of the WR anomaly, whose spectral position is determined by $\lambda = (n_2 - n_1 \sin \theta_i) \Lambda/m$, where n_1 is the refractive index of the incident medium, n_2 is the refractive index of the substrate, θ_i is the incident angle of the irradiated light, Λ is the grating period and m is the diffraction order. For the vanishing first order in a $\Lambda = 350$ nm grating, we have $n_1 = n_2 = 1.5$, $\theta_i = 0$ and $m = 1$ and we obtain $\lambda = 525$ nm (the refractive index of substrate and superstrate are identical). Hence, the near–field at position 1 shows no higher order diffraction and is dominated by the propagating SPP excited on the incident side of the structure as evidenced by the near–field. The electric field inside the cavity is very low and long lobes with high field intensity extend towards the incident direction of the light, which is the signature of a propagating mode at the surface of the grating. Strong charges are also present on the top part of the wire, forming a radiating dipole in each structure. This results in a high reflectivity, which is a well–known feature of metallic gratings for wavelengths close to the WR anomaly [262], [263].
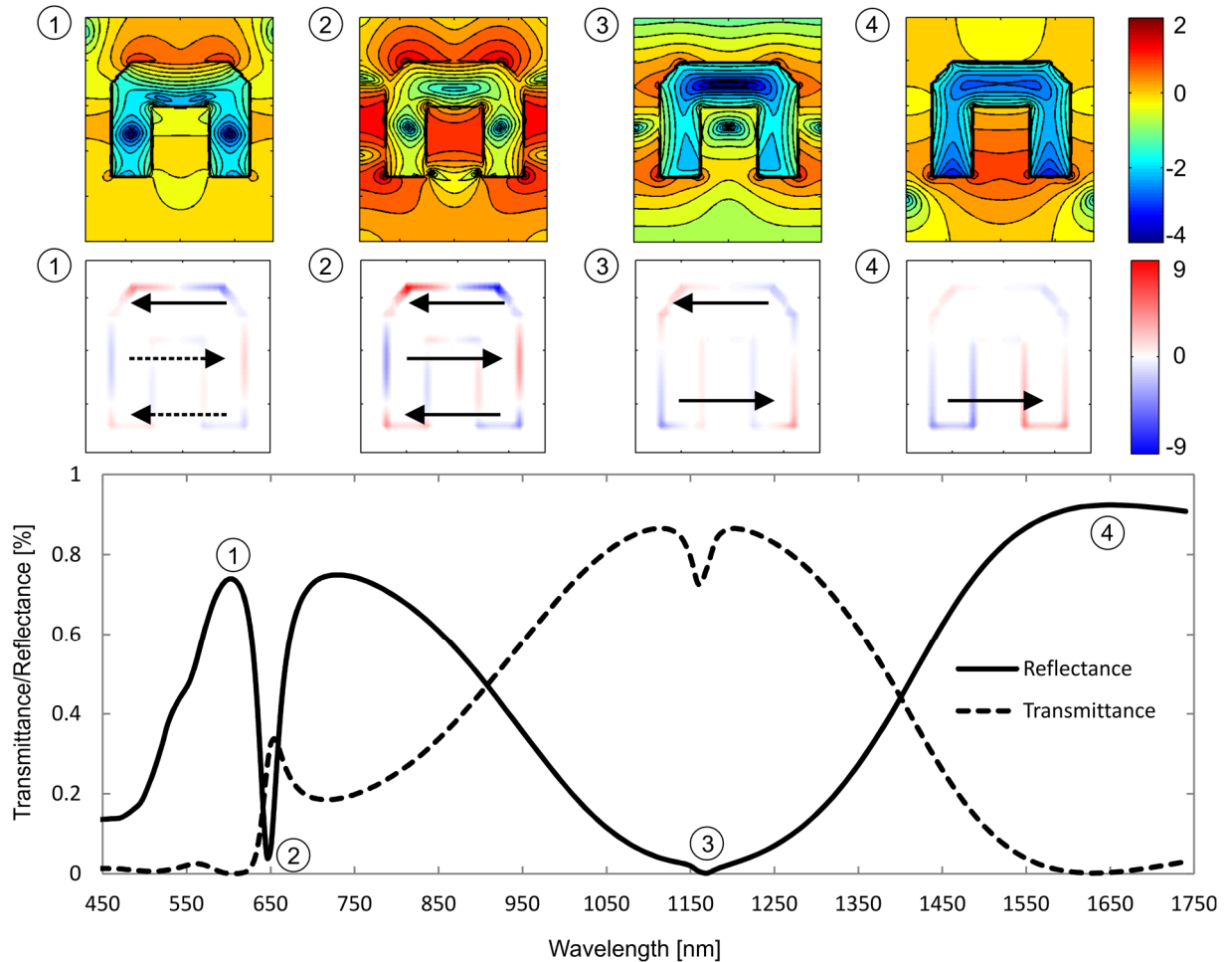
Figure 49. SIE simulations of the reflected (solid line) and transmitted (dashed line) far–field (bottom) are shown together with the computed near–fields (top) and charge distributions (middle) at selected spectral positions for $D = 90$ nm gold on each side of the grating (350 nm period, 200 nm depth, $w = 0.3$).

At the reflectance minimum of the Fano–resonance (Position 2, around $\lambda = 650$ nm), the near–field shows similar lobes on the top surface, indicating the continued presence of the horizontal SPP. In contrast to position 1, additional field maxima exist now at the cavity center and its far end, which are likely caused by vertical SPP modes (no SPP is visible on the back side). This coupled mode has the highest field enhancement of all four spectral positions and exhibits a hexapolar distribution of charges in the structure. Absorbance is maximal at Position 2 (besides wavelengths below 550 nm, where gold intrinsically absorbs), which is a typical feature of subradiant modes. Towards the infrared region of the Fano–resonance, the horizontal SPP vanishes gradually. The infrared portion of the spectrum contains the quadrupolar (Position 3, $\lambda = 1170$ nm) and dipolar (Position 4, $\lambda = 1650$ nm) localized plasmon modes. These are the two lower order LSPR modes with two maxima and a single maximum between the structures respectively. The quadrupolar mode shows enhanced absorption and the dipolar mode is strongly radiating, as is expected from such charge distributions. The charges are weaker for theses modes, which accounts for the decreased losses (absorbance) when compared to the hexapolar mode
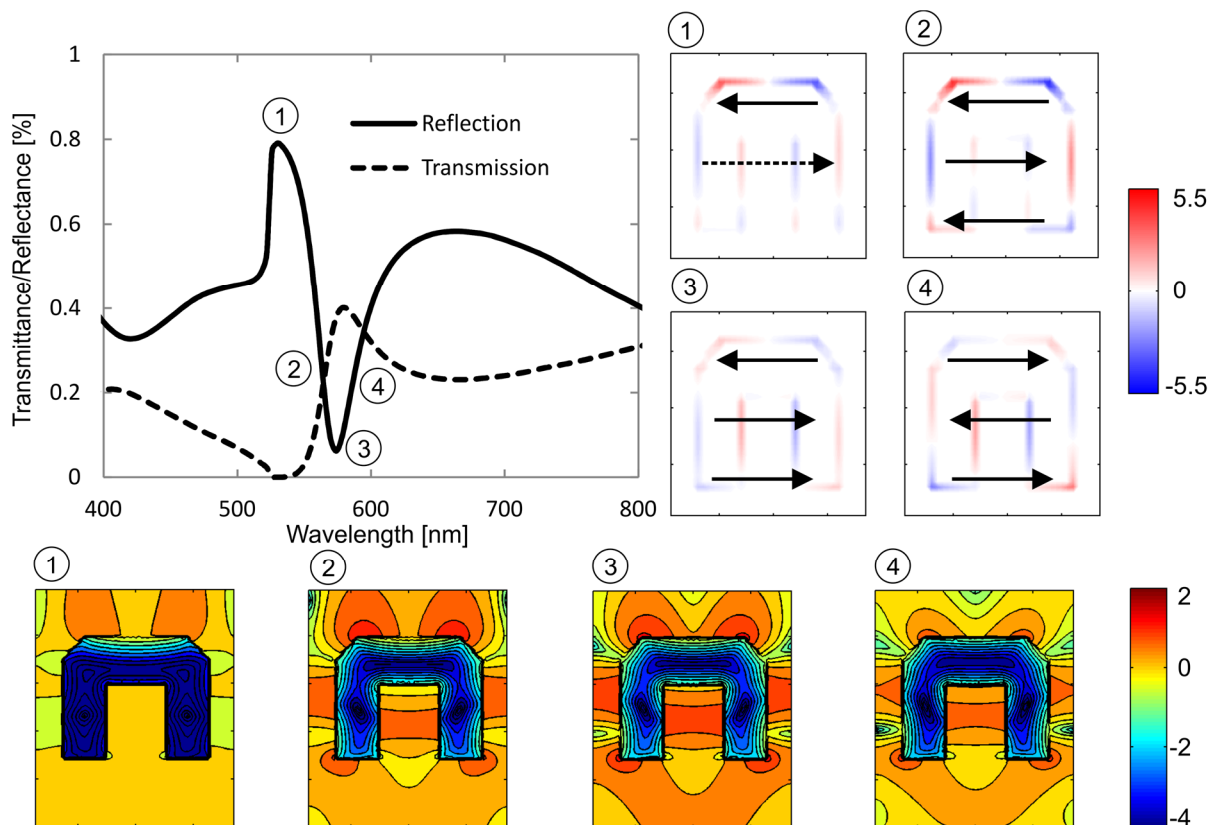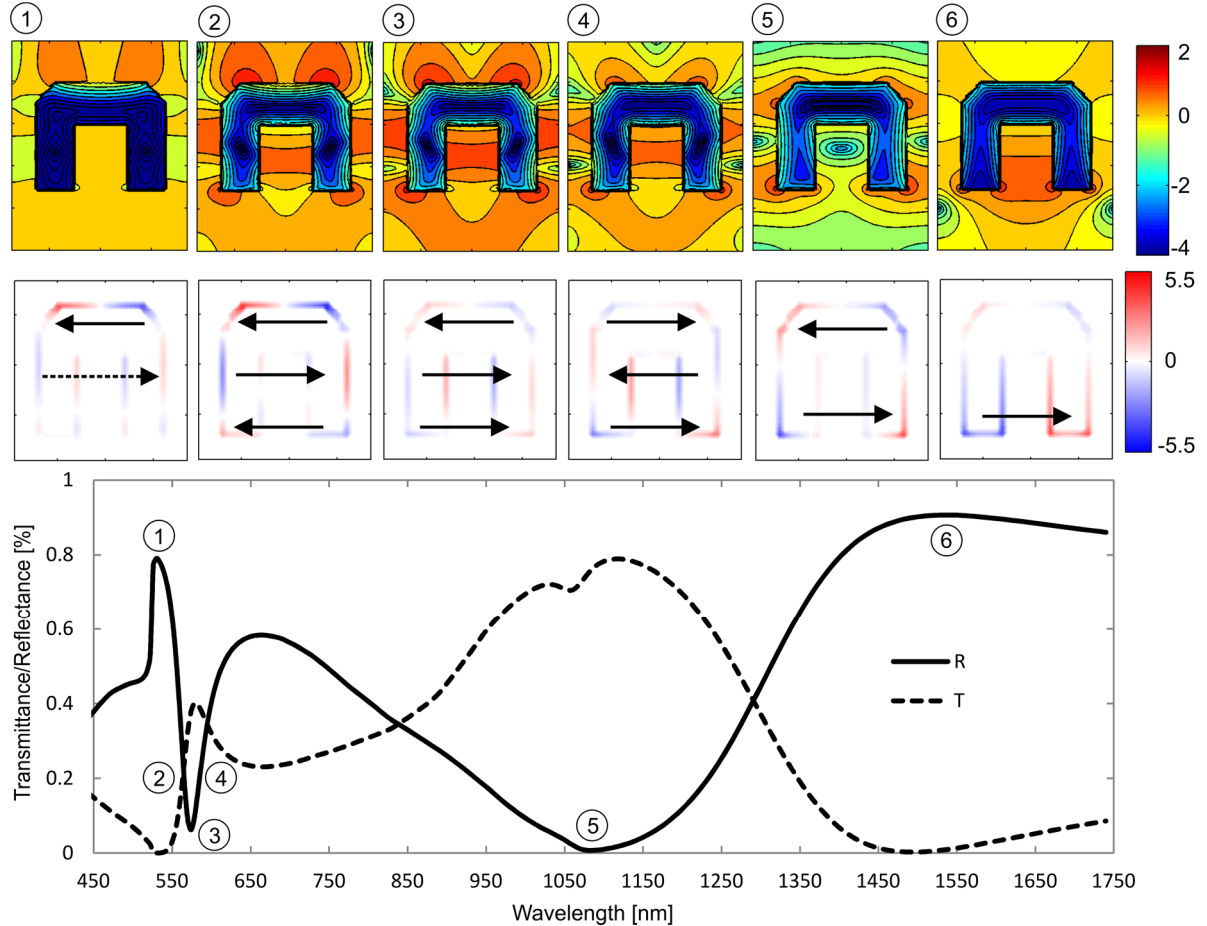
Figure 50. SIE simulations of the reflected (solid line) and transmitted (dashed line) far–fields (top left) are shown together with the computed charge distributions (top right) and near–fields (bottom) at selected spectral positions for $D = 90$ nm aluminum on each side of the grating (350 nm period, 200 nm depth, w=0.3).

Switching from gold to aluminum allows plasmonic resonances to access the green, blue and even ultraviolet wavelengths, which makes it a much better choice for visual applications. Changing to aluminum also causes all the plasmonic modes to shift towards lower wavelengths (by around 70 nm, compare Figure 48 (e) to (f)) since the excitation of plasmonic resonances requires a higher energy in aluminum. As a result, the Fano–resonance is moved further towards the WR anomaly since the position of the WR anomaly only depends on the grating parameters and is independent of the plasma frequency of the metal. At wavelengths below the WR anomaly, a part of the incident light is redistributed into higher diffraction orders, which in turn leads to lower specular reflectance. A feature of this spectral proximity of the Fano–resonance to the WR anomaly is therefore a significant lowering of the peak's full width at half maximum. Choosing the period such that the WR anomaly lies at the lower wavelength end of the Fano–resonance is a straightforward way to take advantage of such spectral features. They are especially favorable for sensing since a small spectral shift of the peak leads to a strong intensity response at the initial peak wavelength.

On the other hand, the comprehension of the modes becomes more complicated when the evaporated material is aluminum and the plasmonic resonances overlap with the WR anomaly (Figure 50). Yet, we can use the different observations made for gold although the hexapolar charge distribution cannot be found at the resonance minimum (Position 3) but is shifted to the short wavelength slope (Position 2). Besides the diminishing horizontal SPP (long lobes at the incident interface become flatter with increasing wavelength), no significant near–field variations are visible when comparing the three positions around the resonance minimum. In

contrast, the charge distribution is substantially altered: The hexapole found at Position 2 first experiences a switch of the charge distribution at the bottom end of the sidewalls (Position 3) before all of the charges appear inverted when looking at the long wavelength slope of the reso-resonance (Position 4). Similar phenomena have been observed close to Fano–resonances in other systems [20], [264] and can be related to a classical oscillator driven off–resonance: If the input frequency is low, the resonator will oscillate in phase with the incoming field but for frequencies above the resonance frequency of the oscillator, they will be 180° out of phase.

Figure 51. SIE simulations of the reflected (solid line) and transmitted (dashed line) far–fields (bottom) are shown together with the computed near–fields (top) and charge distributions (middle) at selected spectral positions for $D = 90$ nm aluminum on each side of the grating.

The spectrum of the aluminum structure in the infrared is also very close to the gold counterpart apart from the shift towards shorter wavelengths. The quadrupolar distribution can be retrieved at around $\lambda \approx 1070$ nm (Position 5) and the radiative dipolar mode is found at $\lambda \approx 1500$ nm. The near–fields and charge distributions are very similar for both materials.

It is worth mentioning that charges are only rarely simulated in metallic gratings. As presented above, they can provide valuable insights into the nature of the resonance at hand and the exact mode of interaction between the incident field and the resonator. In the present Al grating we see for example that the hexapolar mode is attenuated and switches sign at the minimum, which influences the sensitivity of the resonator towards its surrounding. The investigation of charges can therefore contribute greatly to the understanding of plasmonic systems and help tailoring them for specific needs.
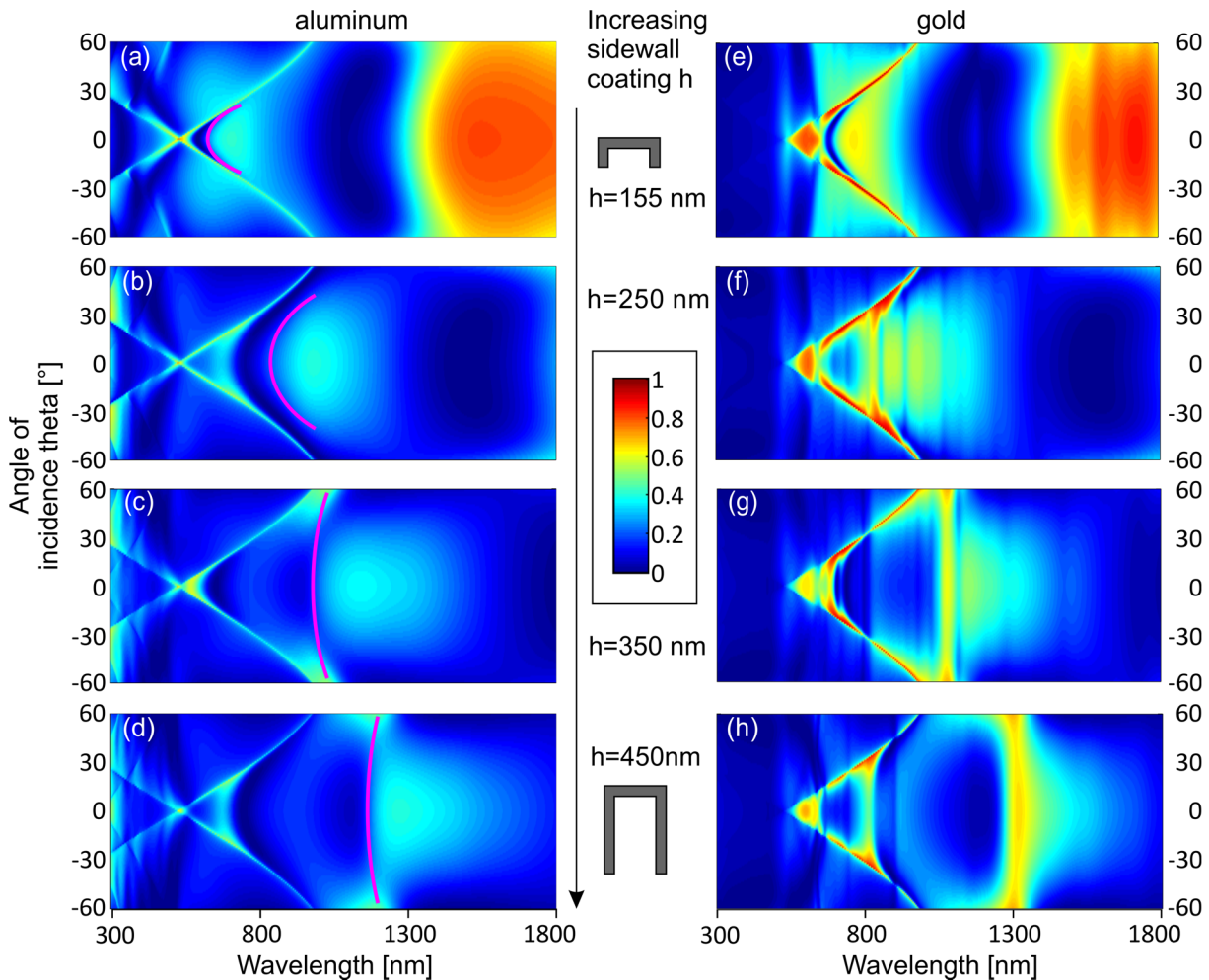
Figure 52. Computed reflectances (intensities in color map) for TM polarized light are shown for wavelengths between 300 nm and 1800 nm and angles of incidence from –60° to 60° (inside the medium). The sidewall length is varied between (a) $h = 155$ nm and (d) $h = 450$ nm in aluminum (left) as well as gold wires (right, (e) $h = 155$ nm and (h) $h = 450$ nm).

At increasing angles of incidence θ in classical grating mount (angle between incident light and surface normal; the plane of incidence is perpendicular to the grating lines), the WR anomaly and the propagating SPP redshift and lead to the disappearance of the Fano–resonance (Figure 52 (a), 155 nm). On the other hand, a reflectance peak remains around $\lambda = 600$ nm at high incidence angles, corresponding to the localized hexapolar mode. For this incidence angle, the resonance is decoupled from the SPP and its original dispersion can be retrieved. Another way of tuning the resonance away from the WR anomaly is by increasing the sidewall length. Figure 53 (c) verifies the preservation of the hexapolar charge distribution in the case of $h = 450$ nm (Figure 52 (h)) at a wavelength of 1325 nm in absence of the horizontal SPP (no lobes in the near–field, Figure 53 (b)). In general, the angle dependence of the resonance strongly decreases as it is decoupled from the SPP (indicated by the purple line in Figure 52 (a) to (d) for the aluminum case, which serves as a guide to the eye). This is intuitive as – in contrast to thin film interference, where the resonating wavelength depends on the angle of incidence – the present resonance is confined to the wires. Hence, the shape of the wires and their spacing are the main determinant parameters for the resonance position. The angle of incidence on the other hand determines how strong the incident field can couple to this resonance (weaker coupling at increasing angles of incidence is especially visible for aluminum in the darker blue colors in Figure 52). The retrieval of this undisturbed dispersion confirms the proposed localized mode since similar

observations were reported earlier [223], [256]. Also, the sharp, destructive Fano–like interference coming from the SPP is alleviated and the lineshape turns into a broader, less asymmetric resonance (Figure 53). The increased width of the resonance is amplified by the red–shift, which leads to an enhancement of the radiative losses [20], [265]. It is worth pointing out that also the spectral width of the dip is much narrower when it is in the proximity of the WR anomaly. This beneficial effect has been observed earlier and can be attributed to strong coupling between the SPP and the LSPR.
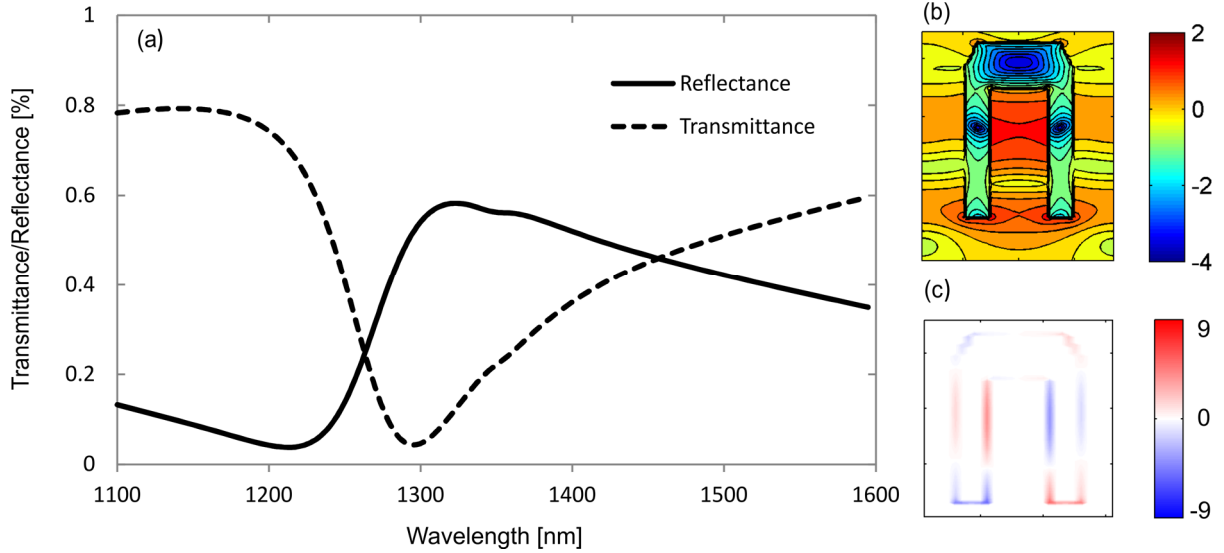
Figure 53. (a) A Part of the spectrum for the 450 nm deep gold structure from Figure 52 is shown together with (b) the near–field and (c) the charge distribution at the reflectance maximum.

In summary, I have shown that the present resonance constitutes of two plasmonic modes, a hexapolar, localized plasmonic mode and a SPP on the incident, flat side of the U–shape. The localized plasmon shows a broad lineshape whose spectral position depends on the height of the sidewalls. When it couples to the SPP, a typical, asymmetric Fano–resonance is observed. The destructive interference from the Wood–Rayleigh anomaly finally further enhances the resonance modulation.

As a side note it is worth mentioning that, in the present example, the groove on the back side of the structure (introduced by the initial dielectric grating) mainly leads to enhanced transmittance when compared to solid metal wires (see Figure 54). A minor shift of the quadrupolar mode could also be observed (minimum around $\lambda = 1000$ nm). Research on similar structures however showed that strongly enhanced absorption may result from the introduction of grooves [255], [257]. Fully exploring this effect would go beyond the scope of this thesis, but proper tuning of the parameters also led to very high absorbance values (above 95%) in my simulations. In the context of this thesis, the simpler fabrication technique is the main reason for using U–shaped instead of solid wires.
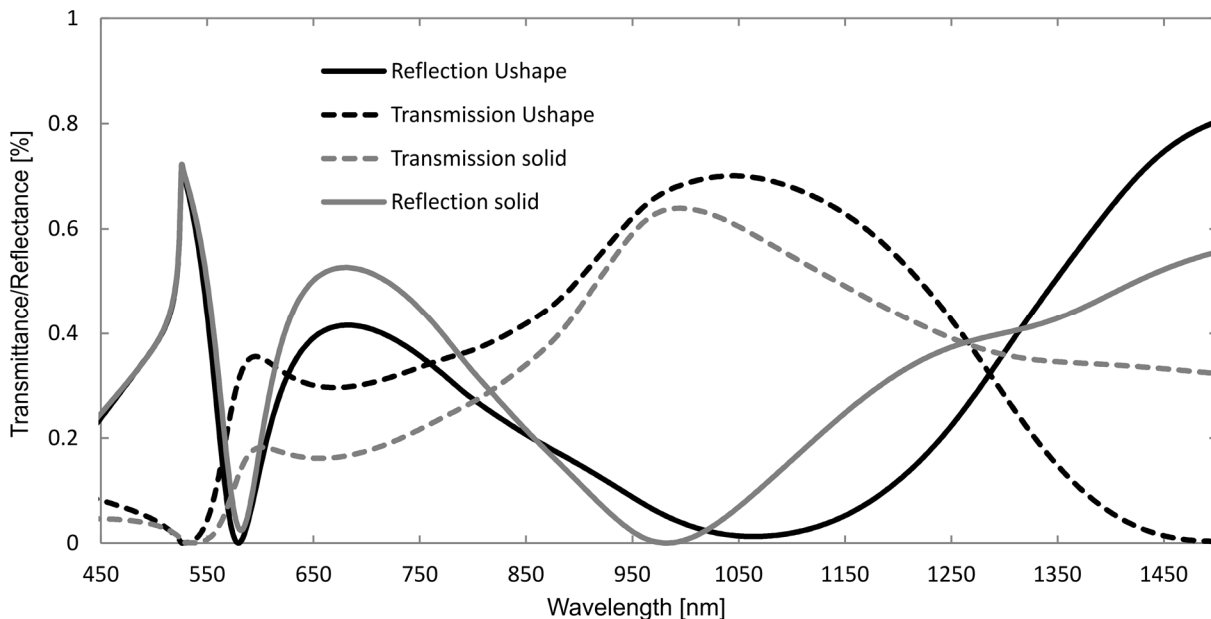
Figure 54. Comparison of the optical properties of U–shaped wires and solid aluminum wires (missing the backside groove).

Since the resonance wavelength of the hexapole depends on the sidewall height h, it is possible to tune its spectral position by adjusting the evaporation angle. The steeper the angle α is, the shorter the coatings on the grating sidewalls become, hence leading to shorter U–shapes after encapsulation. Figure 55 (a) shows how such an adjustment of α affects the spectrum: The maximum caused by the WR anomaly stays at around $\lambda = 525$ nm as expected, since it only depends on the grating period and not the wire parameters. On the other hand, the minimum can be shifted from around $\lambda = 550$ nm for $\alpha = 64°$ to above $\lambda = 600$ nm for $\alpha = 52°$. If the evaporation angle becomes too flat, the minimum shifts into the WR anomaly and vanishes.

The shape of the resonance can also be tuned by changing the thickness of the evaporated metal (Figure 55 (b)). First, increasing the evaporated metal thickness increases the height of the wires due to the additional material deposited on the grating ridge. It is therefore not surprising that the hexapolar mode shifts towards longer wavelengths for a thicker metallization. In addition to this effect, tuning the metal thickness allows controlling the height of the reflection maximum close to the WR anomaly. It is clearly visible that the peak is strongly attenuated for a thinner metallization. When considering that SPPs on the top surface of the structure are an important constituent of this feature (no SPPs can be excited on the back side due to the sidewalls [254]), we can relate the present structure to plasmonic waveguides: short-range SPPs, which are comparable to the present SPPs, can experience stronger confinement and hence higher losses when propagating on thinner metal films [266]. In our case, we expect this mechanism to increase the non–radiative losses stronger than the radiative ones, which results in a lower reflectance.
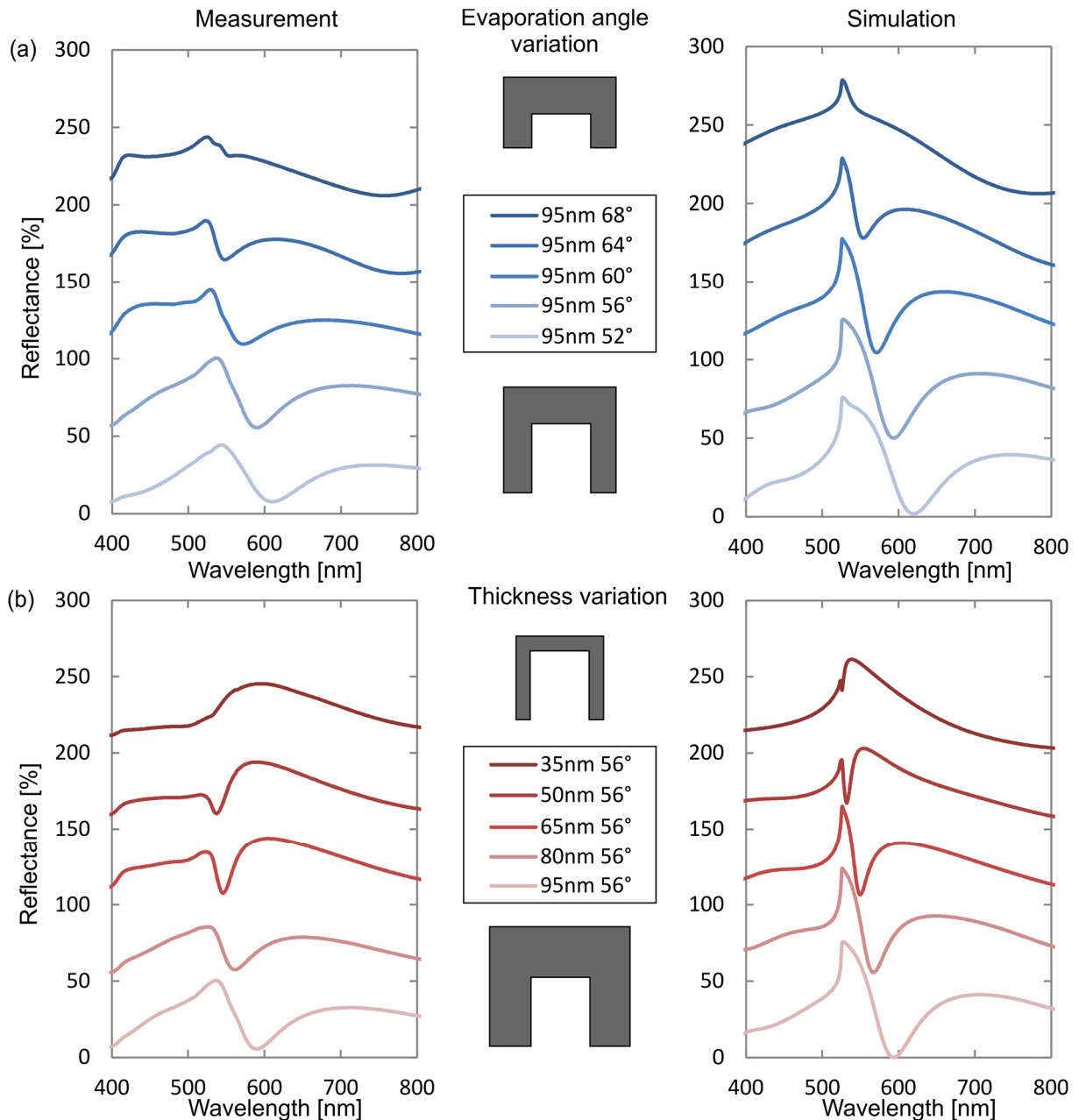
Figure 55. Measured (left) and computed (right) spectra for Al structures evaporated (a) at different angles (blue) and (b) with various thicknesses (red). The curves are shifted by 50%.

Both parameters are readily adjustable in lab–scale evaporators, but also in a roll–to–roll production line these adjustments can be done on the fly. Usually, the embossed structure needs to be adapted in order to shift the resonance, which requires exchanging the embossing master. For such an exchange, the machine of course needs to be halted. Since this is not necessary with the proposed technique, the added flexibility is very valuable for industrial production. Measurements and simulations with rigorous coupled wave analysis (RCWA [190]) show good agreement for all the cases investigated in this work (left and right column in Figure 55). The RCWA method allows significant reduction of the computation time when compared to surface integral equation method, which is essential when screening through suitable parameters for production. It is worth noting that for thicker metal layers or flatter angles α, the shape of the metal structures can change significantly and the use of more sophisticated models might become necessary.
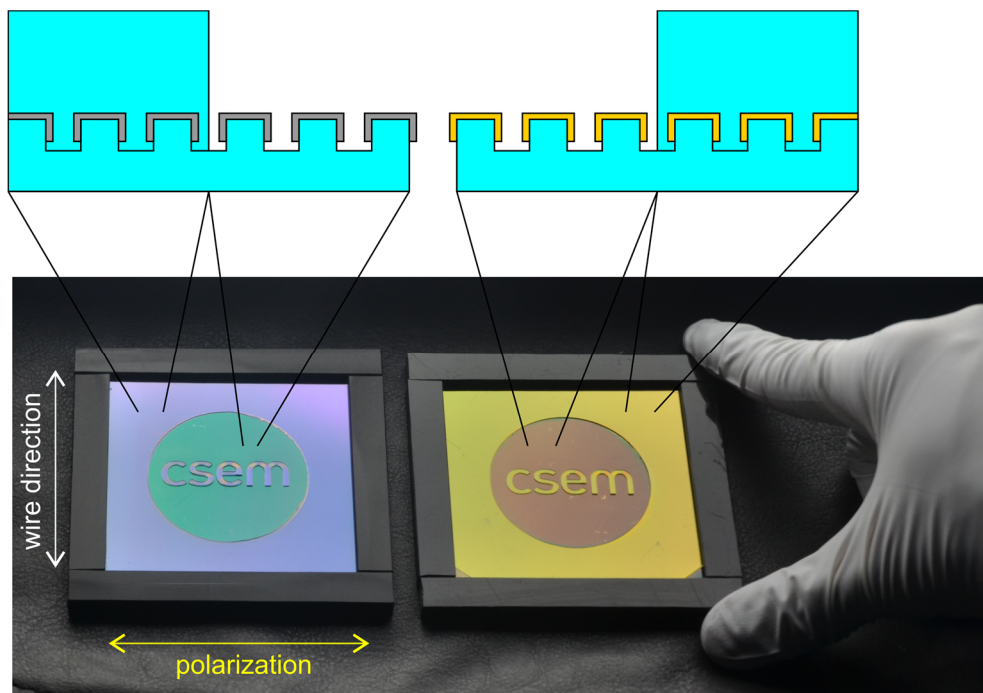
Figure 56. Photograph of aluminum (left) and gold (right) evaporated samples sharing the same parameters otherwise. The image also shows the contrast between embedded (border and letters) and air interfaced parts (circular area) of the structure, when viewed through a polarizer.

The choice of materials is a final way of tuning the resonance. The difference between structures fabricated with either of the two metals is even evident to the naked eye as illustrated by the photo (taken through a polarizer oriented perpendicular to the grating lines) in Figure 56: The embedded aluminum wires (left) show a strong purple color at an angle of view of around 45°, whereas the gold evaporated grating (right) is yellow. A strong contrast is also visible between encapsulated regions of the samples (Letters and border) and the areas interfacing air (central round shape, compare with sketches). Strong spectral responses are therefore also expected for polymer coatings with different refractive indices or refractive index changes in a sensing layer. This motivates the use of the reported structure for optical sensing on large surfaces (maybe even for visual applications) or structural colors, which can handily be controlled by properly choosing the polymer coating.

5.3   Strain sensor

As mentioned in Section 2.2.4, sensing has been one of the most important applications of plasmonics in the past decades. The strong near–field enhancement plasmon resonances provide allows for detection of small concentrations of an analyte in biological or chemical applications [122]. Since Fano–resonances, as a particular class of plasmonic resonances, show sharp spectral features, they are therefore popular for sensing and color effects. They were even reported to have the ability of making mono–layers of protein molecules visible to the naked eye [23]. Near–field interactions in periodic plasmonic structures on the other hand are very sensitive to the distance between the resonators [1]. This property has sparked interest in using plasmonic resonances for measuring translation on the nano–scale [21] and hence also in strain sensing [267]. Most current strain sensors are either based on electrical mechanisms [268], Fiber Bragg gratings [269] or photonic crystal fibers [270]. Whereas these approaches can be extremely sensitive, they do not allow for a direct visual readout and require either optical or electrical connects. Colorimetric sensors can solve both of these issues: they allow for remote

sensing (e.g. using a spectroradiometer), which is a very important property in civil engineering or healthcare [253], [271], and can even generate a visual response. Photonic crystals [272]–[274], high–contrast metastructures [250] as well as plasmonic resonances [251], [275], [276] were recently shown to enable such a colorimetric response to strain. Fabrication of these structures unfortunately often relies on lithographic processes or the self–assembly of nanoparticles, which are not eligible for high–throughput processes.

In the following, I will show how the U–shaped nanowires reported in the previous section can be fabricated on a stretchable substrate. Upon application of a force perpendicular to the grating lines, the spacing between the nanowires will increase as verified with SEM measurements. This displacement causes the WR anomaly to red–shift, overlap with the Fano–resonance and lead to a strong damping of the amplitude. The reflected color as visible to the naked eye switches from purple to green in the process. No deteriorations of the spectral response are observed even after several strain cycles. Finally, all the fabrication processes are suitable to roll–to–roll fabrication and this report could therefore pave the way for inexpensive, large–area strain sensing. Note that read–out in specular reflection as proposed here is preferred over transmission [21] or absorption [251], especially in the context of remote sensing or strain monitoring on nontransparent objects like e.g. buildings.

Polyurethane was hot embossed with a nickel shim of $\Lambda = 350$ nm period and $w = 0.3 \, \Lambda$ ridge width (Figure 57 (a)). The replica was subsequently evaporated with $D = 95$ nm of aluminum at an angle $\alpha = 55°$ with respect to the surface normal from each side of the grating (Figure 57 (b)). A high evaporation rate was used (more than 3 nm/s) in order to ensure adequate optical properties and minimize the heat transfer to the substrate [176]. The resulting nanowires were finally covered with Polydimethylsiloxane (PDMS, Sylgard® 184, Dow Corning Corp., mixing ratio of 10:1 between precursor and curing agent).
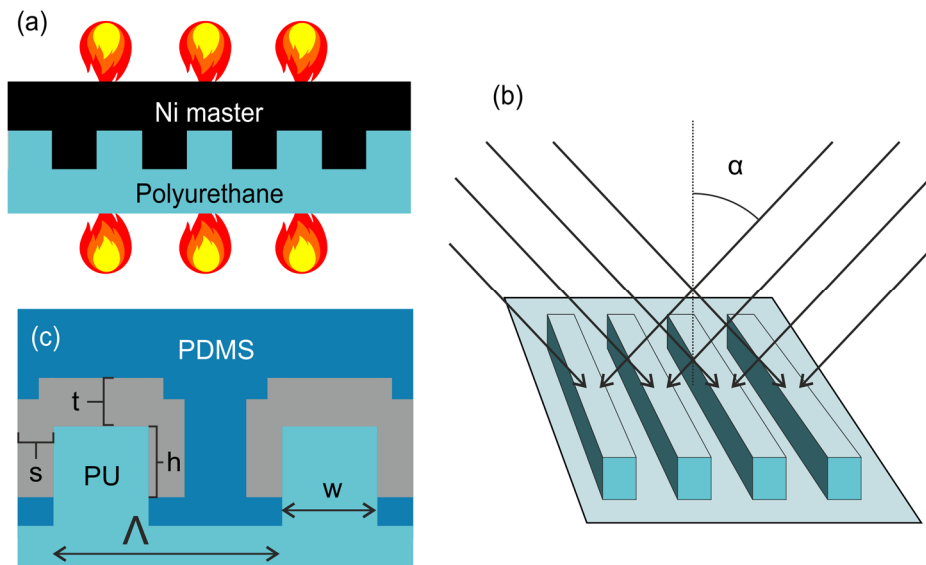
Figure 57. The fabrication process consists of (a) hot embossing of Polyurethane and (b) oblique deposition of aluminum at an angle α. (c) Shows the resulting structure after embedding with PDMS and indicates the relevant parameters for simulations.

The relevant parameters for RCWA simulations are given in Figure 57 (c) and are essentially the same as in the previous section with an evaporated thickness of 95 nm. The only difference is the substantially lower refractive index of PDMS, which hence was approximated by $n_{PDMS} = 1.41$ for the incident medium. The geometry for reflection measurements is depicted in

Figure 58 (a): The light impinges at an angle β with respect to the surface normal, the plane of incidence is oriented parallel to the nanowires and the polarization perpendicular to them (con-(conical mount, TE polarized light). The embedded nanostructures were spectrally characterized (Perkin Elmer Lambda 9) at $\beta = 6°$. The more realistic observation geometry for actual applications is $\beta = 45°$ and this angle was hence used for simulations (corresponding to $\approx 30°$ inside the PDMS) as well as for visual examination of the sensor. Cylindrical poles were used to clamp the sensor and ensure homogeneous stress distribution; the stretch direction was perpendicular to the wires (Figure 58 (a)). Since the specimen had to be placed upside down on a tripod in the spectrophotometer at hand, the strained sensor was mechanically stabilized by reversibly gluing (Ormocer) a glass slide to the back of the substrate. The resonance shapes were found to closely agree with similar measurements performed on a F20 spectrophotometric setup (Filmmetrics Inc.), which validates the present approach.

The spectral features in measurements and simulations align well (compare the dashed line to the solid line in Figure 58 (b)), but the reflectance is significantly lower in measurements. Corrugations and bending caused by the flexible substrate can have a strong influence on the measured reflection besides typical fabrication imperfections. Nonetheless, a peak reflectance of $\approx 30\%$ is achieved with negligible noise, which is a very good value. Note that the mismatch between the refractive indices of the substrate and superstrate creates an additional WR anomaly, which is visible in the form of a shoulder in measurements and simulations (Figure 58 (b), WR anomalies around 500 nm and 525 nm). Comparison to alternatives is however difficult since most reports resort to arbitrary units or relative values. Also, reflective stress sensing is surprisingly uncommon, despite its high potential for remote read–out.
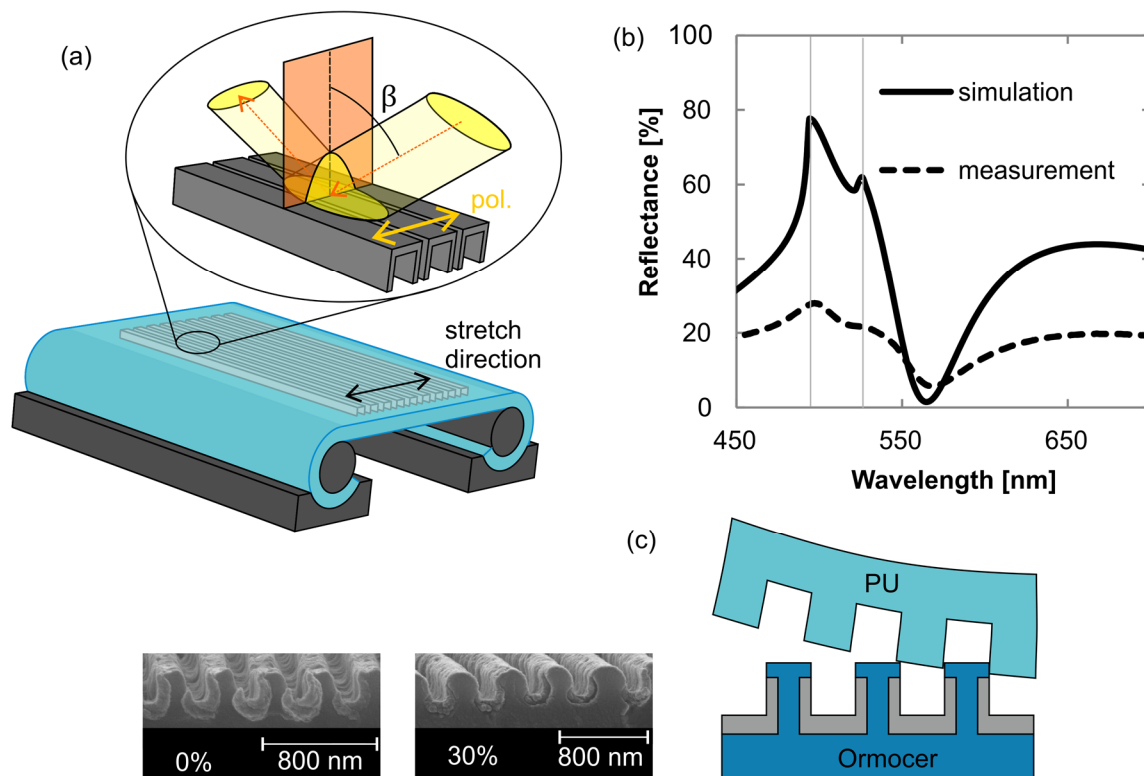
Figure 58. (a) Depicts the experimental stretch setup together with the optical characterization geometry, (b) compares measurements (dashed) to simulations (solid) in the relaxed state and (c) shows SEM measurements of the relaxed (0%) and stretched (30%) nanostructures, as well as the template stripping process utilized for attaining them.

In order to assess the response of the structure to strain on a microscopic scale, a cross–section of the sample is required. PU can unfortunately not be broken and no direct technique for inves-investigating the cross–section of the wires exists; I therefore used the template stripping process sketched in Figure 58 (c) to enable such measurements. Instead of PDMS, UV curable Ormocer (Micro Resist Technology GmbH) was poured onto the uncovered wires and after exposure, the Ormocer including the nanostructures could easily be peeled. This process works in the relaxed (0%) as well as the stretched state (30%) of the substrate. Analysis of the peeled structure reveals that the elongation of the grating period is almost equal to the elongation of the substrate: an expansion from 350 nm to $\approx$ 445 nm is measured in the SEM pictures in Figure 58 (c), which is close to the expected 455 nm. The images also reveal that the metal wires re-main stable and only the spacing between them is expanded. It is clear that no stretching of the wires could be expected due to the around two orders of magnitude higher Young's modulus of aluminum in comparison to the ones of PU and PDMS. The fact that no fractures are visible in this view however verifies the toughness of the evaporated metal.

It is worth noting that the polymer contracts in the direction perpendicular to the elongation (Poisson effect). The impact this effect has on the nanowires becomes evident when comparing the initial state of the sensor (Figure 59 (a)) to the 17% stretched version (Figure 59 (b)): The strain will cause the wires to meander, but no ruptures are observed. This is also supported by Figure 59 (c), which shows the same structure after five stretch cycles of 17%. The only difference between Figure 59 (a) and Figure 59 (c) are a slight increase in point defects and marginal residual tilt of small regions. The pictures hence indicate the reversibility of the deformations caused by the applied strain. The optical response of the sensor can therefore be related to the increased inter–wire distance and to a minor extent to the meandering in this regime. For strains up to 20%, this finding motivates the use of ductile metals over brittle high refractive index materials as often used in photonic crystals [277], [278] or high–contrast metastructures [250].
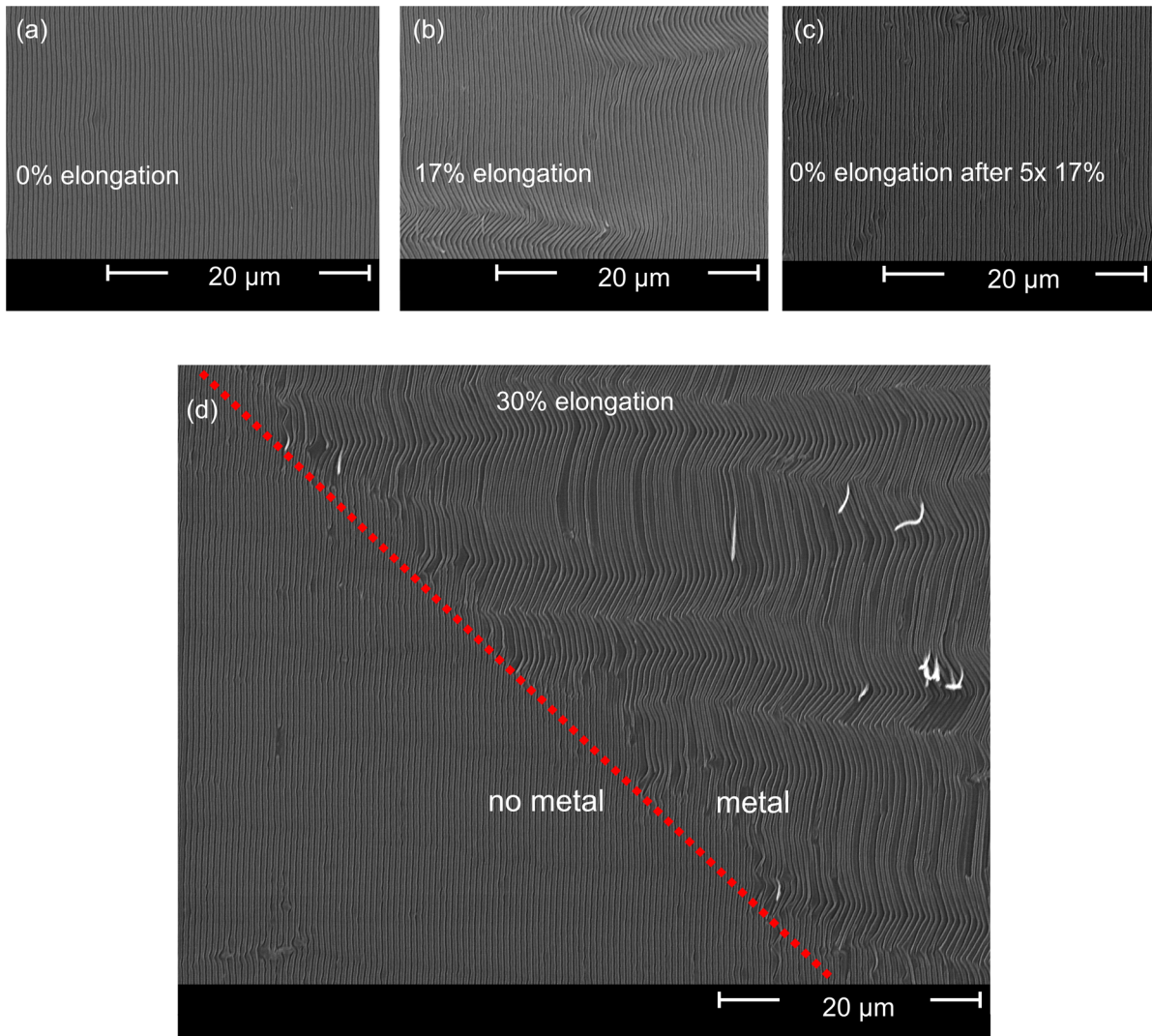
Figure 59. SEM pictures of the template stripped nanowires are presented, (a) shows the freshly fabricated nanowires before strain, (b) at 17% elongation and (c) again at 0% after five stretch cycles of 17%. (d) Compares metallized to non–metallized parts of the sample at 30% elongation.

At 30% elongation or more, in SEM investigations the wires were found to break and peel in addition to the buckling (metallized part in Figure 59 (d)). Note that uncoated gratings did not show the meandering behavior (non metallized part of Figure 59 (d)). It is finally worth mentioning that stretching took place without the PDMS cladding for the SEM measurements, which makes the wires more vulnerable to out–of–plane bending or peeling. The actual sensor is thus mechanically more stable, but a maximal elongation of 20% was chosen to prevent damage.

The optical response of the sensor is shown in Figure 60 (a) (polarization is perpendicular to the wires, curves are spaced by 20%): The relaxed position (purple) shows a well–modulated Fano–resonance. The peak position is thereby fixed by the WR anomaly and the dip, caused by the interaction of an LSPR with the SPP on the incident side, is highly tunable as reported previously. The position of the WR anomaly can be found where the first reflected order vanishes, which means that the diffraction angle $\theta_1^R(\lambda)$ reaches 90°.

In the present case, the grating equation needs to be adapted for conical incidence and the diffraction angle can be calculated with [216]:

$$\theta_m^R(\lambda) = \sin^{-1}\left(\frac{m\lambda}{\Lambda\,cos(\beta)\,n_1(\lambda)}\right),$$ [5–5]

where n_1 is the refractive index of the cover material, Λ the period of the grating, m the diffraction order, β the angle of incidence with respect to the surface normal along the wires and λ the wavelength of the impinging radiation. For $n_1 = 1.41$, $\Lambda = 350\,nm$, $\beta = 6°$ and $m = 1$ a diffraction angle of $\theta_1^R(\lambda) = 90°$ is achieved at $\lambda \approx 490\,nm$. Increasing the grating period by 20% to $\Lambda = 420\,nm$ shifts the anomaly to $\lambda \approx 590\,nm$. This shift can be seen in the measurements as indicated by the black solid line (the total displacement is a bit lower, which is understood since the elongation of the grating period is also slightly below expectations). Additionally, a strong damping of the Fano–amplitude is observed, which is attributed to the increasing spectral proximity of the WR anomaly to the LSPR. This detrimental effect of the WR anomaly is consistent with the findings in the previous section. It is worth mentioning that the coupling of the Fano–resonance to the WR anomaly also causes the Fano–resonance to red–shift upon stretching, but to a much lesser extent than the WR anomaly itself. The reversibility of the stretching process is finally also endorsed by the constant spectrum after several stretch cycles (Figure 60 (a), compare dark blue curve to purple curve).

Two different modes of sensing can be imagined: Tracking of the WR anomaly or evaluation of the resonance damping. The first would be much easier to implement, but probably less sensitive (especially for small strains). The latter could be achieved by fitting the Fano–lineshape given in equation [5–4] to the curve and determining the damping parameter b, as e.g. also proposed in reference [1]. Alternatively, the difference in reflectance between the resonance maximum and minimum could be used for gauging the sensor. As this peak–valley difference already decreases from $\approx 23.9\%$ to $\approx 14.8\%$ for an elongation of 5% (compare purple to violet curve in Figure 60 (a)), the approach can be expected to be very sensitive in this regime.

RCWA simulations are used to verify the previously demonstrated spectral response (Figure 60 (b)) and investigate its capability for visual sensing. For modeling the mechanical response to strain, constant metal structures were assumed to be displaced from each other while increasing the polymer thickness between them (as observed in the SEM measurements). The grating period is linearly scaled in the process as illustrated by the sketches in Figure 60. In this series of simulations (curves are spaced by 40%), a very similar movement of the WR anomaly and damping of the resonance amplitude are retrieved.

An adjustment of the observation geometry is required in order to evaluate the structure for its visual response. A more realistic angle of view of 45° ($\beta = 30°$ in PDMS) was chosen for these simulations (dashed curves in Figure 60 (b)). According to equation [5–5], this change causes the WR anomaly to shift to $\lambda \approx 430\,nm$. The expected movement is clearly visible in the unstrained simulations when comparing the purple curve for $\beta = 6°$ to the rose dashed curve for $\beta = 45°$. It is worth noting that the LSPR shifts by the same amount and the resonance shape is almost perfectly conserved in the process. The sensor can therefore be spectrophotometrically evaluated at a wide angle of incidence β (this is an advantage over the recently popularized opal films, which are strongly angle dependent in any direction due to the Bragg conditions [279]).
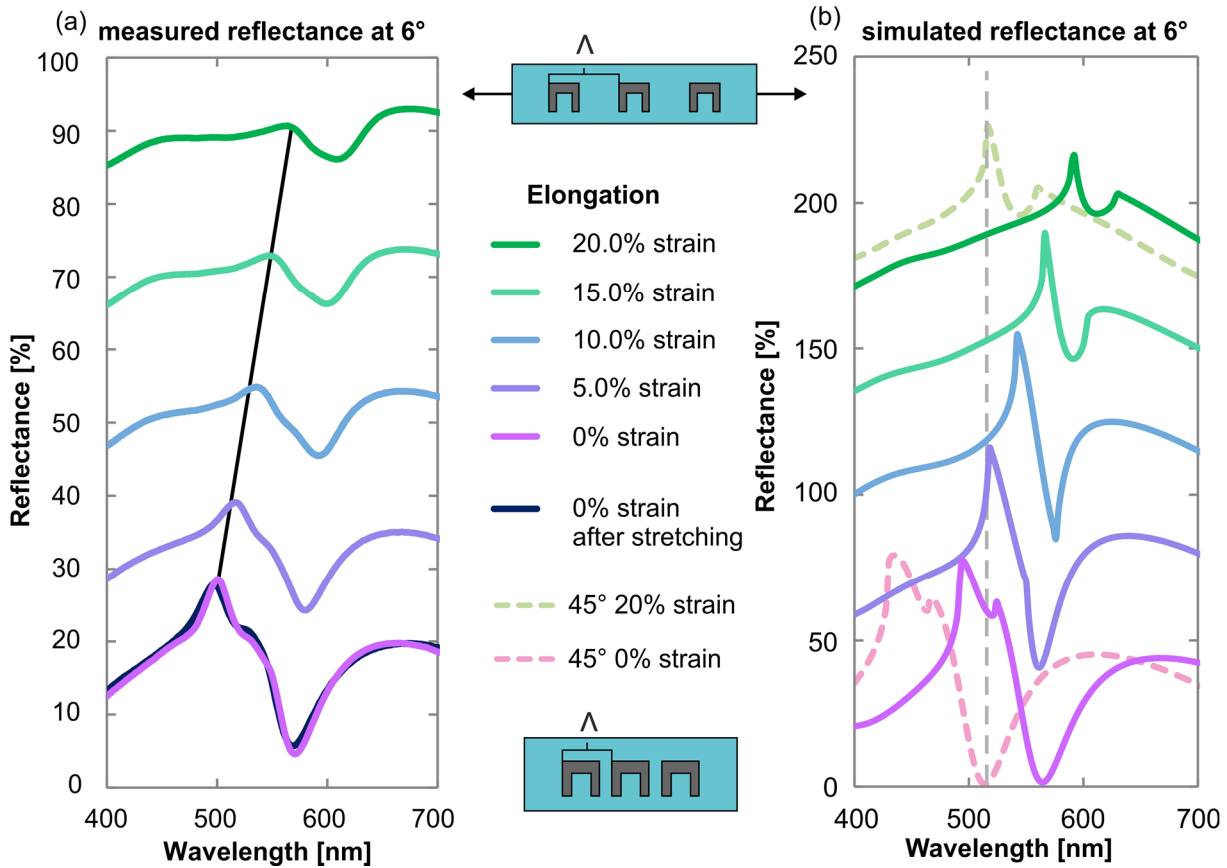
Figure 60. (a) Measured and (b) simulated reflectances at $\beta = 6°$ for elongations between 0% and 20% are shown. The offsets between the individual curves are 20% for the measurements and 40% for the simulations respectively. The black line follows the movement of the peak caused by the WR anomaly upon strain and serves as a guide to the eye. The dashed curves show the simulated reflectances at $\beta = 45°$ for 0% strain (rose) and 20% strain (green). The grey dashed line illustrates the spectral overlap at 520 nm of the minimum for 0% elongation with the maximum at 20% elongation in this case.

Ideally, elongation shifts the WR peak to the position where the Fano–dip initially was, which leads to a maximal response. As shown in the previous section, the position of the resonance minimum can easily be controlled with the evaporation parameters. Proper choice of the grating period (and thereby the position of the WR anomaly as calculated above) then allows the above condition to be met for a wide range of wavelengths and elongations. In the present example, such a behavior was achieved for a viewing angle of $\beta = 45°$, an elongation of ≈17% and a wavelength of ≈520 nm (grey dashed line in Figure 60 (b)). 520 nm corresponds to the color green, which the human eye is the most sensitive to. The sensor is therefore designed to yield the highest perceptual change possible by switching between the complementary colors purple/magenta and green. The actual colors as visible to the human eye (middle row) and as retrieved from the simulated spectra (bottom row) are shown in Figure 61.
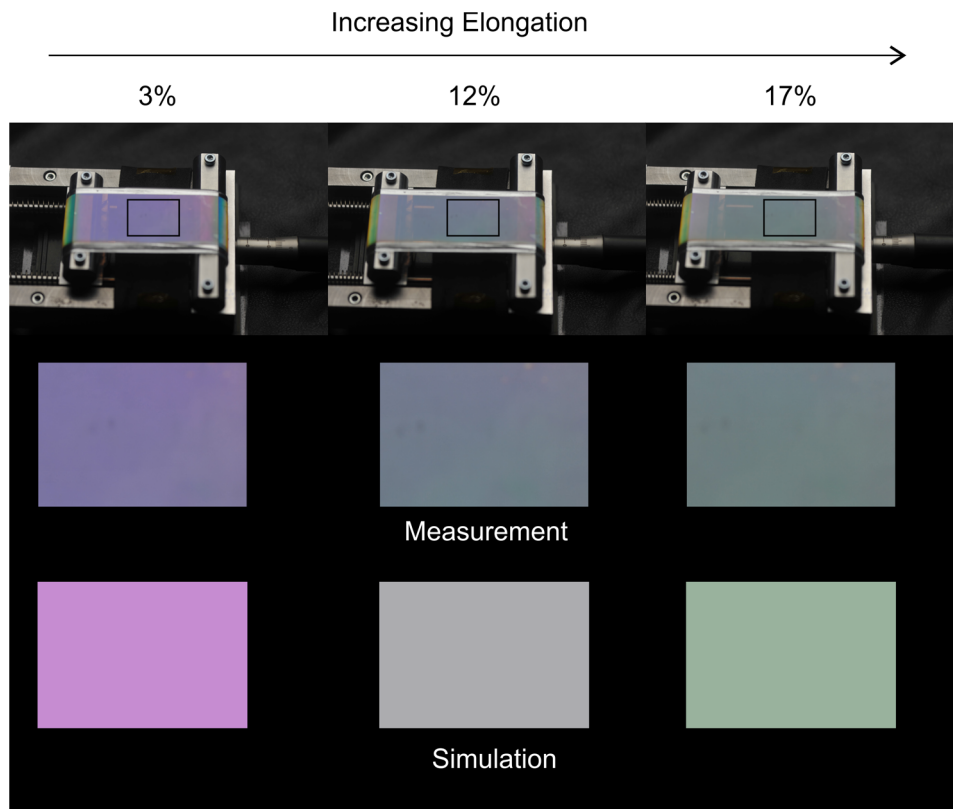
Figure 61. Visible response of the stretch sensor for elongations of up to 17% and their simulated counterparts photographed through a horizontally arranged polarizer at an angle of view $\beta = 45°$.

The aspired switch from purple to green is clearly observed for measurements as well as simulations. The colors in the photograph are slightly less brilliant, yet clearly visible to the naked eye. The fabricated samples are 3 cm by 9 cm in size, cut from a 4″ ($\approx$ 10 cm) round substrate, and the initial distance between the cylinders is around 5,5 cm. The present approach is limited in area only by the embossing master and the evaporation chamber, both of which can easily be up–scaled. Laser interference lithography allows for close to m² size generation of periodic nanostructures in a single exposure [13]. Embossing as well as physical vapor deposition are both roll–to–roll compatible processes [184], which would enable the application of the present structure to almost arbitrarily sized objects.

5.4   Conlusion

In conclusion, in this chapter I have first presented an industry compatible way of fabricating Fano–resonant aluminum and gold nanostructures on large surfaces. Serial patterning like EBL could be avoided by using holographically produced gratings together with oblique metal deposition. By means of far–field as well as near–field and charge calculations, the subradiant mode of the Fano–resonance was determined to be a surface plasmon polariton coupled to a localized plasmon mode. The coupled mode exhibits a hexapolar charge distribution, associated with high electric near–fields and a strongly enhanced absorbance. I was able to tune the resonance position and spectral intensity distribution through the change of easily accessible evaporation parameters. This property makes the present structure very attractive for high–throughput, low–cost production such as roll–to–roll manufacturing. The design of different physical colors through proper choice of the polymer coating is a promising path to investigate. Finally, the steep Fano–lineshape of this structure is appealing for incorporation into sensors, which can be applied to large areas and provide an optical response directly visible

to the naked eye. The following section will show how this idea was put into practice by present-presenting a material that responds to external strain by color change.

In the second part of the chapter, an optical strain sensor based on Fano-resonances in U-shaped nanowires has been presented. Application of strain perpendicular to the wires increases the spacing between the wires and thereby the period of the structure. In combination with buckling of the wires due to the Poisson effect, this deformation led to a steep decrease of the modulation amplitude. The strong response observed for these nanowires is e.g. very attractive for remote strain sensing. Through careful design of the resonance positions, a well visible color switch from purple to green could be achieved. As the present structure is strictly based on up-scalable processes like embossing and evaporation, the reported stretch sensor could be produced with high-throughput processes like e.g. roll-to-roll manufacturing. The reported technique therefore potentially paves the way for colorimetric, large-area strain sensing. The sensor itself requires no power and can be read out remotely, which is e.g. highly desirable for strain monitoring in civil engineering.

Chapter 6   Conclusions

6.1   Summary

In this thesis I presented novel approaches for the fabrication of photonic and plasmonic nanostructures. The reported techniques are up–scalable and bridge the gap between typical lab–scale nanofabrication and industrial production. Binary gratings were replicated into low–cost polymers and subsequently shadow evaporated with either high refractive index dielectrics or metals. Depending on the exact process, the nanostructures were equipped with a variety of exciting properties. ZnS helped boosting the unpolarized diffraction efficiency into the first transmission order by almost an order of magnitude to around 70%. My computations showed that the structure can even be encapsulated in polymer without destroying this effect, which prevents the structure from degrading due to environmental influences. Possible applications include light management for solar cells, backlighting for displays or waveguide coupling.

It was also shown that thin metallic coatings selectively enhance the first order transmittance for TE polarized light at the position of the Wood–Rayleigh anomaly. This wavelength dependent diffraction was used for the creation of orientation dependent color effects. Logos, which switched color when flipping or rotating the substrate by 180° were presented as well as colorful, floating images. These effects could find application in banknote security or brand protection of display devices.

When switching polarization, plasmonic resonances could be excited in the metallized gratings. The particular geometry investigated in this thesis relied on encapsulated horseshoe– or U–shaped nanowires. The periodic arrangement of such structures resulted in nanoscale gaps between them, which were found to support localized plasmon resonances. These LSPRs showed a hexapolar charge distribution and, together with surface plasmon polaritons excited on the grating surface, exhibited a Fano–resonance. The position and the shape of the resonance depend on the sidewall length and the metal thickness of the U–shape, both of which can easily be controlled by tuning the evaporation parameters. The resulting structure appears in brilliant colors and could therefore be of interest for security or decoration applications.

In this thesis, a different family of applications was investigated: Since plasmonic resonances in general and Fano–resonances in particular are famous for their sensitivity to the arrangement of the constituent resonators, the applicability of the presented structures for strain sensing was explored. Polyurethane was embossed and shadow evaporated with aluminum for that purpose. By stretching the substrate perpendicularly to the wires, the Fano resonance was red–shifted and strongly damped. This behavior was shown to be reversible and the same spectra were recovered also after several strain cycles. Through proper tuning of the resonance, it is easily possible to maximize the sensor's response for the desired wavelength and elongation length. The signal can then be read out with a spectrophotometer or even better a spectroradiometer. This finding could hence e.g. pave the way for remote strain sensing for buildings or vehicles.

In this strain sensor study, a maximal colorimetric response was targeted. It was realized by positioning the minimum of the resonance around 520 nm for the relaxed sensor, resulting in a purple appearance. After elongating the structure by 20%, the resonance maximum caused by the Wood–Rayleigh anomaly shifted to the position where the minimum initially was, resulting in a green color. The present switch between the two complementary colors is very well visible to the naked eye. This example therefore illustrates the great potential of the fabrication approach for large–area sensing.

6.2   Outlook

Although the processes used in this thesis are suitable for roll–to–roll fabrication, they could not be tested in such systems. The actual implementation will therefore still require engineering work, be it for optimizing the embossing parameters or adapting the evaporation procedure for moving substrates. Apart from these necessary changes that need to be considered for industrial production, there are also many other avenues to be explored in continuation of this thesis. Embedded asymmetric zinc sulfide coatings were not measured experimentally, but encapsulation should definitely be a priority in the future since it is particularly favorable for outdoor applications like e.g. photovoltaics, lighting or signage. Actual implementation into such objects is also worth investigating, since especially light management for solar cells is a hot topic in research as well as industry.

In a more general sense, I think that fixtures based on embedded, diffractive nanostructures could significantly enhance existing devices. Signs based on waveguiding for example already exist, but currently utilize scattering films instead of gratings for outcoupling. I am convinced that diffractive structures can be more efficient and hence help saving power at comparable production costs. In the same vein, LEDs could also become more efficient through application of a grating layer to extract trapped modes. Equipping lighting devices with functional fixtures is in general very exciting for lighting applications and hence also a promising and vivid field of research (see e.g. the project LASSIE funded by the European Commission [280]).

Display technologies also offer great opportunities for diffractive structures, although I am not convinced that they are the optimal solution for lighting large screens like e.g. TVs. It is in my experience extremely challenging to design diffractive devices for applications relying on white light. The grating dispersion requires careful consideration of all the possible incident and diffracted angle as well as diffraction efficiencies for the different geometries. Another concern is the size of the screen: Most of the light is outcoupled when it reaches the grating for the first time (assuming high efficiencies), which lets the light intensity strongly diminish towards the center of the device. These issues are however not insurmountable for smaller devices and diffractive backlights could find application in smartphones or tablets. An important advantage of gratings however is their partial transparency. See–through displays as for example found in head–up–displays can therefore strongly profit from gratings (patents in this direction have e.g. been filed for military applications by BAE systems [281]). Here, colored light is usually sufficient and diffractive approaches could enable low–cost, lightweight solutions.

It further seems very attractive to apply diffractive structures to solar cells to boost their efficiency. They could even be produced separately from the cells themselves since the diffractive structures only interact via far fields with the semiconductor. The processes in photovoltaic devices are very complex though, and their efficiency cannot simply be approximated by the path length of the impinging light in the semiconductor. Provided that the

necessary modelling and engineering work is invested, I however believe that such an add-on to photovoltaic devices could become a very successful product. Commercial interest should be very high for such a fixture, especially when considering the expected low production costs.

The diffractive color effects presented in this thesis could still be further optimized for the suggested applications. The gratings show first order reflections in specific configurations, which can be disturbing. By minimizing the according efficiency or lowering the grating period, these substrates could be improved. Further, since the presented effects only rely on TE polarized light, controlling the other polarization would allow for advanced designs. Plasmonics lends itself to create colors for TM polarization and the addition of such features could either fortify the effect at hand in unpolarized light or, in contrary, result in strongly polarization dependent colors.

I think that, in contrast to the diffraction based applications, plasmonic substrates have to be directly implemented into final devices and do not lend themselves for extensions of existing applications. In my opinion, the most unique and desirable feature of plasmonic resonances is the capability of concentrating incident radiation to subwavelength volumes; this hence allows for an optical response to nanoscale processes. Although not all of the reported applications (like e.g. color effects) rely on this property, I believe that resonances as the ones demonstrated in the U-shaped nanowires bear the highest potential in the context of sensing applications. Besides the strain sensing capabilities explored in this thesis, other sensing principles could be implemented. Temperature sensing using thermal expansion or humidity sensing using for example hydrogels [282] are promising options to investigate. Biological or chemical sensors as used in laboratories are probably not target applications of these low-cost, aluminum based structures. The possibility of generating a visual response is however very attractive for e.g. evaluating the freshness of food [283]. Mass-producible plasmonic resonators like the ones reported in this thesis seem to be perfect candidates for incorporation in disposable food packaging.

Such concentration of radiation could also be of great interest for photocatalysis or photovoltaics. Implementation of plasmonic nanostructures into these applications is however more challenging, since they need to be introduced during the already complex fabrication process. Also, further optimization of the present structure is required as maximal near-field enhancement was not a primary goal of this thesis. For reference, near-fields were enhanced by around one order of magnitude in comparison to the incident radiation, but improvements should easily be possible. Controlling the resonance with the evaporation process could then prove to be very valuable, since the near-field enhancement is often desired at a distinct spectral position. I think however that research on these U-shaped nanowires could go in many directions from this starting point: The low-cost materials, as well as the tunable, reasonably simple fabrication process, are highly favorable for various applications in academia as well as industry.

A final topic that deserves more attention in the future is the setup I devised for diffraction efficiency measurements. During my PhD time it became evident that the spectrally resolved measurement of diffraction efficiencies is crucial for the proper characterization of gratings. Especially applications in photovoltaics and lighting rely on the undisturbed grating response for properly estimating the effect of the grating. In the reflection case, this information can readily be retrieved with an integrating sphere, but for transmission gratings, reflection and refraction at the rear side of the substrates cause severe distortions. This problem is alleviated

by application of a half-cylindrical lens as reported in this thesis, but the resulting focusing of the outcoupled light is not optimal and needs to be considered in the baseline. Also, variation of the angle of incidence for the impinging light would be desirable for the above applications, which is not available with the described setup. Finally, simplifications in the alignment procedure and data readout would make the setup more accessible for other users. Combination of the present approach with an integrating sphere is also conceivable and maybe even favorable. Close attention however needs to be paid that only the diffracted order of interest is collected.

Bibliography

[1]   B. Gallinet, T. Siegfried, H. Sigg, P. Nordlander, and O. J. F. Martin, "Plasmonic Radiance: Probing Structure at the Angstrom Scale with Visible Light," *Nano Lett.*, vol. 13, no. 2, pp. 497–503, Feb. 2013.

[2]   S. Kinoshita, S. Yoshioka, and K. Kawagoe, "Mechanisms of structural colour in the Morpho butterfly: cooperation of regularity and irregularity in an iridescent scale," *Proc. R. Soc. B-Biol. Sci.*, vol. 269, no. 1499, pp. 1417–1421, Jul. 2002.

[3]   F. Liu, B. Q. Dong, X. H. Liu, Y. M. Zheng, and J. Zi, "Structural color change in longhorn beetles Tmesisternus isabellae," *Opt. Express*, vol. 17, no. 18, p. 16183, Aug. 2009.

[4]   P. Vukusic and J. R. Sambles, "Photonic structures in biology," *Nature*, vol. 424, no. 6950, pp. 852–855, Aug. 2003.

[5]   R. H. Siddique, R. Hünig, A. Faisal, U. Lemmer, and H. Hölscher, "Fabrication of hierarchical photonic nanostructures inspired by Morpho butterflies utilizing laser interference lithography," *Opt. Mater. Express*, vol. 5, no. 5, pp. 996–1005, May 2015.

[6]   *Transactions of the American Philosophical Society.* The Society, 1786.

[7]   "Photographic Map of the Normal Solar Spectrum (made by Professor H. A. ROWLAND)," *Publ. Astron. Soc. Pac.*, vol. 6, p. 55, Jan. 1894.

[8]   G. R. Harrison, E. G. Loewen, and R. S. Wiley, "Echelle gratings: their testing and improvement," *Appl. Opt.*, vol. 15, no. 4, p. 971, Apr. 1976.

[9]   J. Sauvage-Vincent, Y. Jourlin, S. Tonchev, C. Veillas, P. Claude, and O. Parriaux, "Industrial fabrication of an optical security device for document protection using plasmon resonant transmission through a thin corrugated metallic film embedded on a plastic foil," 2012, vol. 8428, p. 84280F–84280F–7.

[10]   R. Caputo, L. De Sio, M. J. J. Jak, E. J. Hornix, D. K. G. de Boer, and H. J. Cornelissen, "Short period holographic structures for backlight display applications," *Opt. Express*, vol. 15, no. 17, p. 10540, 2007.

[11]   T. Järvenpää and V. Aaltonen, "Compact near-to-eye display with integrated gaze tracker," 2008, vol. 7001, pp. 700106–700106–8.

[12]   H. A. Atwater and A. Polman, "Plasmonics for improved photovoltaic devices," *Nat. Mater.*, vol. 9, no. 3, pp. 205–213, Mar. 2010.

[13]   NIL Technology, "Laser Interference Lithography." [Online]. Available: http://www.nilt.com/531/laser-interference-lithography. [Accessed: 26-Jun-2015].

[14]   I. Freestone, N. Meeks, M. Sax, and C. Higgitt, "The Lycurgus Cup - A Roman Nanotechnology," *Gold Bulletin 2007*.

[15]   H. Fischer and O. J. F. Martin, "Engineering the optical response ofplasmonic nanoantennas," *Opt. Express*, vol. 16, no. 12, pp. 9144–9154, Jun. 2008.

[16]   M. I. Stockman, "Nanoplasmonic sensing and detection," *Science*, vol. 348, no. 6232, pp. 287–288, Apr. 2015.

[17]   K. R. Catchpole and A. Polman, "Plasmonic solar cells," *Opt. Express*, vol. 16, no. 26, pp. 21793–21800, Dec. 2008.

[18]   Z. Liu, W. Hou, P. Pavaskar, M. Aykol, and S. B. Cronin, "Plasmon Resonant Enhancement of Photocatalytic Water Splitting Under Visible Illumination," *Nano Lett.*, vol. 11, no. 3, pp. 1111–1116, Mar. 2011.

[19]   U. Fano, "Effects of Configuration Interaction on Intensities and Phase Shifts," *Phys. Rev.*, vol. 124, no. 6, pp. 1866–1878, Dec. 1961.

[20]   A. Lovera, B. Gallinet, P. Nordlander, and O. J. F. Martin, "Mechanisms of Fano Resonances in Coupled Plasmonic Systems," *ACS Nano*, vol. 7, no. 5, pp. 4527–4536, 2013.

[21]   N. Liu, M. Hentschel, T. Weiss, A. P. Alivisatos, and H. Giessen, "Three-Dimensional Plasmon Rulers," *Science*, vol. 332, no. 6036, pp. 1407–1410, Jun. 2011.

[22]   Y. Shen, V. Rinnerbauer, I. Wang, V. Stelmakh, J. D. Joannopoulos, and M. Soljačić, "Structural Colors from Fano Resonances," *ACS Photonics*, vol. 2, no. 1, pp. 27–32, Jan. 2015.

[23]   A. A. Yanik, A. E. Cetin, M. Huang, A. Artar, S. H. Mousavi, A. Khanikaev, J. H. Connor, G. Shvets, and H. Altug, "Seeing protein monolayers with naked eye through plasmonic Fano resonances," *Proc. Natl. Acad. Sci.*, vol. 108, no. 29, pp. 11784–11789, Jul. 2011.

[24]   M. T. Gale, C. Gimkiewicz, S. Obi, M. Schnieper, J. Sochtig, H. Thiele, and S. Westenhofer, "Replication technology for optical microsysterns," *Opt. Lasers Eng.*, vol. 43, no. 3–5, pp. 373–386, May 2005.

[25]   R. W. Wood, "On a Remarkable Case of Uneven Distribution of Light in a Diffraction Grating Spectrum," *Proc. Phys. Soc. Lond.*, vol. 18, no. 1, p. 269, Jun. 1902.

[26]   P. Jacquinot, "The Luminosity of Spectrometers with Prisms, Gratings, or Fabry-Perot Etalons," *J. Opt. Soc. Am.*, vol. 44, no. 10, p. 761, Oct. 1954.

[27]   K. C. Harvey and C. J. Myatt, "External-cavity diode laser using a grazing-incidence diffraction grating," *Opt. Lett.*, vol. 16, no. 12, pp. 910–912, Jun. 1991.

[28]   M. Schwartz and J. Hayes, "A history of transatlantic cables," *IEEE Commun. Mag.*, vol. 46, no. 9, pp. 42–48, Sep. 2008.

[29]   L. Tong, J. Lou, and E. Mazur, "Single-mode guiding properties of subwavelength-diameter silica and silicon wire waveguides," *Opt. Express*, vol. 12, no. 6, pp. 1025–1035, Mar. 2004.

[30]   A. Mekis, J. C. Chen, I. Kurland, S. H. Fan, P. R. Villeneuve, and J. D. Joannopoulos, "High transmission through sharp bends in photonic crystal waveguides," *Phys. Rev. Lett.*, vol. 77, no. 18, pp. 3787–3790, Oct. 1996.

[31]   D. N. Christodoulides, F. Lederer, and Y. Silberberg, "Discretizing light behaviour in linear and nonlinear waveguide lattices," *Nature*, vol. 424, no. 6950, pp. 817–823, Aug. 2003.

[32]   W. Bogaerts, R. Baets, P. Dumon, V. Wiaux, S. Beckx, D. Taillaert, B. Luyssaert, J. Van Campenhout, P. Bienstman, and D. Van Thourhout, "Nanophotonic waveguides in silicon-on-insulator fabricated with CMOS technology," *J. Light. Technol.*, vol. 23, no. 1, pp. 401–412, Jan. 2005.

[33]   A. Cutolo, M. Iodice, P. Spirito, and L. Zeni, "Silicon electro-optic modulator based on a three terminal device integrated in a low-loss single-mode SOI waveguide," *J. Light. Technol.*, vol. 15, no. 3, pp. 505–518, Mar. 1997.

[34]   R. Bruck and R. Hainberger, "Efficient coupling of narrow beams into polyimide waveguides by means of grating couplers with high-index coating," *Appl. Opt.*, vol. 49, no. 10, pp. 1972–1978, Apr. 2010.

[35]   H. Ma, A. K. Y. Jen, and L. R. Dalton, "Polymer-based optical waveguides: Materials, processing, and devices," *Adv. Mater.*, vol. 14, no. 19, pp. 1339–1365, Oct. 2002.

[36]   J. Kimmel and T. Levola, "Mobile display backlight light guide plates based on slanted grating arrays," *J. Photonics Energy*, vol. 2, p. 024501, Mar. 2012.

[37]   "BOS ASIA SDN BHD : The Copper Box, venue for Handball at the 2012 Summer Olympics with Tubular skylight." [Online]. Available: http://bosasiasb.blogspot.ch/2013/04/the-copper-box-venue-for-handball-at-te.html. [Accessed: 11-May-2015].

[38]   M. c. Estevez, M. Alvarez, and L. m. Lechuga, "Integrated optical devices for lab-on-a-chip biosensing applications," *Laser Photonics Rev.*, vol. 6, no. 4, pp. 463–487, Jul. 2012.

[39]   "Lumos2 Tricolour | LED Illuminated Signs | Signbox Ltd." [Online]. Available: https://shop.signbox.co.uk/shop/led-illuminated-signs/lumos-tricolour/. [Accessed: 17-Apr-2015].

[40]   "LUCCON Lichtbeton GmbH." [Online]. Available: http://www.luccon.com/en/. [Accessed: 17-Apr-2015].

[41]   H. Mukawa, K. Akutsu, I. Matsumura, S. Nakano, T. Yoshida, M. Kuwahara, K. Aiki, and M. Ogawa, "8.4: Distinguished Paper: A Full Color Eyewear Display Using Holographic Planar Waveguides," *SID Symp. Dig. Tech. Pap.*, vol. 39, no. 1, pp. 89–92, May 2008.

[42]   N. Zhang, J. Liu, J. Han, X. Li, F. Yang, X. Wang, B. Hu, and Y. Wang, "Improved holographic waveguide display system," *Appl. Opt.*, vol. 54, no. 12, pp. 3645–3649, Apr. 2015.

[43]   R. L. V. Renesse, Ed., *Optical Document Security*, 2nd Revised edition edition. Boston: Artech House Publishers, 1998.

[44]   S. P. McGrew, "Hologram counterfeiting: problems and solutions," presented at the Optical Security and Anticounterfeiting Systems, 1990, vol. 1210, pp. 66–76.

[45]   M. T. Gale, "Diffractive microstructures for security applications," in , *Third International Conference on Holographic Systems, Components and Applications, 1991*, 1991, pp. 205–209.

[46]   R. A. Lee, "Micro-technology for anti- counterfeiting," *Microelectron. Eng.*, vol. 53, no. 1–4, pp. 513–516, Jun. 2000.

[47]   P. W. Leech, R. A. Lee, and T. J. Davis, "Printing via hot embossing of optically variable images in thermoplastic acrylic lacquer," *Microelectron. Eng.*, vol. 83, no. 10, pp. 1961–1965, Oct. 2006.

[48]   R. W. Phillips and R. L. Bonkowski, "Security enhancement of holograms with interference coatings," 2000, vol. 3973, pp. 304–316.

[49]   M. Srinivasarao, "Nano-Optics in the Biological World: Beetles, Butterflies, Birds, and Moths," *Chem. Rev.*, vol. 99, no. 7, pp. 1935–1962, Jul. 1999.

[50]   K. Watanabe, T. Hoshino, K. Kanda, Y. Haruyama, and S. Matsui, "Brilliant blue observation from a Morpho-butterfly-scale quasi-structure," *Jpn. J. Appl. Phys. Part 2-Lett. Express Lett.*, vol. 44, no. 1–7, pp. L48–L50, 2005.

[51]   M. T. Gale, K. Knop, and R. H. Morf, "Zero-order diffractive microstructures for security applications," in *Proc. SPIE 1210*, 1990, vol. 1210, pp. 83–89.

[52]   P. Sheng, A. N. Bloch, and R. S. Stepleman, "Wavelength-selective absorption enhancement in thin-film solar cells," *Appl. Phys. Lett.*, vol. 43, no. 6, pp. 579–581, Sep. 1983.

[53]   C. Battaglia, C.-M. Hsu, K. Soederstroem, J. Escarre, F.-J. Haug, M. Charriere, M. Boccard, M. Despeisse, D. T. L. Alexander, M. Cantoni, Y. Cui, and C. Ballif, "Light Trapping in Solar Cells: Can Periodic Beat Random?," *Acs Nano*, vol. 6, no. 3, pp. 2790–2797, Mar. 2012.

[54]   E. Zimmermann, P. Ehrenreich, T. Pfadler, J. A. Dorman, J. Weickert, and L. Schmidt-Mende, "Erroneous efficiency reports harm organic solar cell research," *Nat. Photonics*, vol. 8, no. 9, pp. 669–672, Sep. 2014.

[55]   E. Yablonovitch, "Statistical ray optics," *J. Opt. Soc. Am.*, vol. 72, no. 7, pp. 899–907, Jul. 1982.

[56]   C. Heine and R. H. Morf, "Submicrometer gratings for solar energy applications," *Appl. Opt.*, vol. 34, no. 14, pp. 2476–2482, May 1995.

[57]   S. Mokkapati and K. R. Catchpole, "Nanophotonic light trapping in solar cells," *J. Appl. Phys.*, vol. 112, no. 10, p. 101101, Nov. 2012.

[58]   M. Kroll, S. Fahr, C. Helgert, C. Rockstuhl, F. Lederer, and T. Pertsch, "Employing dielectric diffractive structures in solar cells – a numerical study," *Phys. Status Solidi A*, vol. 205, no. 12, pp. 2777–2795, Dec. 2008.

[59]   D. M. Callahan, J. N. Munday, and H. A. Atwater, "Solar Cell Light Trapping beyond the Ray Optic Limit," *Nano Lett.*, vol. 12, no. 1, pp. 214–218, Jan. 2012.

[60]   Z. Yu, A. Raman, and S. Fan, "Fundamental limit of nanophotonic light trapping in solar cells," *Proc. Natl. Acad. Sci. U. S. A.*, vol. 107, no. 41, pp. 17491–17496, Oct. 2010.

[61]   F. Priolo, T. Gregorkiewicz, M. Galli, and T. F. Krauss, "Silicon nanostructures for photonics and photovoltaics," *Nat. Nanotechnol.*, vol. 9, no. 1, pp. 19–32, Jan. 2014.

[62]   J. Oh, H.-C. Yuan, and H. M. Branz, "An 18.2%-efficient black-silicon solar cell achieved through control of carrier recombination in nanostructures," *Nat. Nanotechnol.*, vol. 7, no. 11, pp. 743–748, Nov. 2012.

[63]   V. Gate, Y. Jourlin, M. Langlet, F. Vocanson, O. Parriaux, G. Bernaud, C. Veillas, and A. Cazier, "New low-cost high-efficiency solar module: diffracting deflector module," *Proc SPIE*, vol. 8438, p. 84380W, 2012.

[64]   J. Yoon, L. Li, A. V. Semichaevsky, J. H. Ryu, H. T. Johnson, R. G. Nuzzo, and J. A. Rogers, "Flexible concentrator photovoltaics based on microscale silicon solar cells embedded in luminescent waveguides," *Nat. Commun.*, vol. 2, p. 343, Jun. 2011.

[65]   M. J. Currie, J. K. Mapel, T. D. Heidel, S. Goffri, and M. A. Baldo, "High-efficiency organic solar concentrators for photovoltaics," *Science*, vol. 321, no. 5886, pp. 226–228, Jul. 2008.

[66]   M. G. Debije and P. P. C. Verbunt, "Thirty Years of Luminescent Solar Concentrator Research: Solar Energy for the Built Environment," *Adv. Energy Mater.*, vol. 2, no. 1, pp. 12–35, Jan. 2012.

[67]   "PrismSolar." [Online]. Available: http://www.prismsolar.com/products.php. [Accessed: 16-Apr-2015].

[68]   S. Chattopadhyay, Y. F. Huang, Y. J. Jen, A. Ganguly, K. H. Chen, and L. C. Chen, "Antireflecting and photonic nanostructures," *Mater. Sci. Eng. R Rep.*, vol. 69, no. 1–3, pp. 1–35, Jun. 2010.

[69]   S. Koynov, M. S. Brandt, and M. Stutzmann, "Black nonreflecting silicon surfaces for solar cells," *Appl. Phys. Lett.*, vol. 88, no. 20, p. 203107, May 2006.

[70]   H. Savin, P. Repo, G. von Gastrow, P. Ortega, E. Calle, M. Garín, and R. Alcubilla, "Black silicon solar cells with interdigitated back-contacts achieve 22.1% efficiency," *Nat. Nanotechnol.*, vol. advance online publication, May 2015.

[71]   M. L. Brongersma, Y. Cui, and S. Fan, "Light management for photovoltaics using high-index nanostructures," *Nat. Mater.*, vol. 13, no. 5, pp. 451–460, May 2014.

[72]   T. W. Ebbesen, H. J. Lezec, H. F. Ghaemi, T. Thio, and P. A. Wolff, "Extraordinary optical transmission through sub-wavelength hole arrays," *Nature*, vol. 391, no. 6668, pp. 667–669, Feb. 1998.

[73]   J. Homola, S. S. Yee, and G. Gauglitz, "Surface plasmon resonance sensors: review," *Sens. Actuators B-Chem.*, vol. 54, no. 1–2, pp. 3–15, Jan. 1999.

[74]   "British Museum," *British Museum.* [Online]. Available: http://www.britishmuseum.org. [Accessed: 20-Apr-2015].

[75] L. Novotny, *Principles of Nano-Optics.* Cambridge ; New York: Cambridge University Press, 2006.

[76] S. Link and M. A. El-Sayed, "Shape and size dependence of radiative, non-radiative and photothermal properties of gold nanocrystals," *Int. Rev. Phys. Chem.*, vol. 19, no. 3, pp. 409–453, Jul. 2000.

[77] J. P. Kottmann, O. J. F. Martin, D. R. Smith, and S. Schultz, "Plasmon resonances of silver nanowires with a nonregular cross section," *Phys. Rev. B*, vol. 64, no. 23, p. 235402, Nov. 2001.

[78] T. Siegfried, Y. Ekinci, H. H. Solak, O. J. F. Martin, and H. Sigg, "Fabrication of sub-10 nm gap arrays over large areas for plasmonic sensors," *Appl. Phys. Lett.*, vol. 99, no. 26, p. 263302, Dec. 2011.

[79] W. Zhang, L. Huang, C. Santschi, and O. J. F. Martin, "Trapping and Sensing 10 nm Metal Nanoparticles Using Plasmonic Dipole Antennas," *Nano Lett.*, vol. 10, no. 3, pp. 1006–1011, Mar. 2010.

[80] S.-W. Ahn, K.-D. Lee, J.-S. Kim, S. H. Kim, J.-D. Park, S.-H. Lee, and P.-W. Yoon, "Fabrication of a 50 nm half-pitch wire grid polarizer using nanoimprint lithography," *Nanotechnology*, vol. 16, no. 9, pp. 1874–1877, Sep. 2005.

[81] M. W. Knight, N. S. King, L. Liu, H. O. Everitt, P. Nordlander, and N. J. Halas, "Aluminum for Plasmonics," *ACS Nano*, vol. 8, no. 1, pp. 834–840, 2013.

[82] G. H. Chan, J. Zhao, E. M. Hicks, G. C. Schatz, and R. P. Van Duyne, "Plasmonic Properties of Copper Nanoparticles Fabricated by Nanosphere Lithography," *Nano Lett.*, vol. 7, no. 7, pp. 1947–1952, Jul. 2007.

[83] H. Rigneault, J. Capoulade, J. Dintinger, J. Wenger, N. Bonod, E. Popov, T. W. Ebbesen, and P.-F. Lenne, "Enhancement of Single-Molecule Fluorescence Detection in Subwavelength Apertures," *Phys. Rev. Lett.*, vol. 95, no. 11, p. 117401, Sep. 2005.

[84] A. Ono, M. Kikawada, R. Akimoto, W. Inami, and Y. Kawata, "Fluorescence enhancement with deep-ultraviolet surface plasmon excitation," *Opt. Express*, vol. 21, no. 15, pp. 17447–17453, Jul. 2013.

[85] I. Gryczynski, J. Malicka, Z. Gryczynski, K. Nowaczyk, and J. R. Lakowicz, "Ultraviolet Surface Plasmon-Coupled Emission Using Thin Aluminum Films," *Anal. Chem.*, vol. 76, no. 14, pp. 4076–4081, Jul. 2004.

[86] Q. Zhang, G. Li, X. Liu, F. Qian, Y. Li, T. C. Sum, C. M. Lieber, and Q. Xiong, "A room temperature low-threshold ultraviolet plasmonic nanolaser," *Nat. Commun.*, vol. 5, Sep. 2014.

[87] C. Langhammer, M. Schwind, B. Kasemo, and I. Zorić, "Localized Surface Plasmon Resonances in Aluminum Nanodisks," *Nano Lett.*, vol. 8, no. 5, pp. 1461–1471, May 2008.

[88] P. R. West, S. Ishii, G. V. Naik, N. K. Emani, V. M. Shalaev, and A. Boltasseva, "Searching for better plasmonic materials," *Laser Photonics Rev.*, vol. 4, no. 6, pp. 795–808, Nov. 2010.

[89] A. K. Geim and K. S. Novoselov, "The rise of graphene," *Nat. Mater.*, vol. 6, no. 3, pp. 183–191, Mar. 2007.

[90] K. S. Novoselov, A. K. Geim, S. V. Morozov, D. Jiang, Y. Zhang, S. V. Dubonos, I. V. Grigorieva, and A. A. Firsov, "Electric field effect in atomically thin carbon films," *Science*, vol. 306, no. 5696, pp. 666–669, Oct. 2004.

[91] A. N. Grigorenko, M. Polini, and K. S. Novoselov, "Graphene plasmonics," *Nat. Photonics*, vol. 6, no. 11, pp. 749–758, Nov. 2012.

[92] J. Chen, M. Badioli, P. Alonso-González, S. Thongrattanasiri, F. Huth, J. Osmond, M. Spasenović, A. Centeno, A. Pesquera, P. Godignon, A. Zurutuza Elorza, N. Camara, F. J. G. de Abajo, R. Hillenbrand, and F. H. L. Koppens, "Optical nano-imaging of gate-tunable graphene plasmons," *Nature*, vol. 487, no. 7405, pp. 77–81, Jul. 2012.

[93] L. Ju, B. Geng, J. Horng, C. Girit, M. Martin, Z. Hao, H. A. Bechtel, X. Liang, A. Zettl, Y. R. Shen, and F. Wang, "Graphene plasmonics for tunable terahertz metamaterials," *Nat. Nanotechnol.*, vol. 6, no. 10, pp. 630–634, Oct. 2011.

[94] Z. Fang, S. Thongrattanasiri, A. Schlather, Z. Liu, L. Ma, Y. Wang, P. M. Ajayan, P. Nordlander, N. J. Halas, and F. J. García de Abajo, "Gated Tunability and Hybridization of Localized Plasmons in Nanostructured Graphene," *ACS Nano*, vol. 7, no. 3, pp. 2388–2395, Mar. 2013.

[95] J. Christensen, A. Manjavacas, S. Thongrattanasiri, F. H. L. Koppens, and F. J. García de Abajo, "Graphene Plasmon Waveguiding and Hybridization in Individual and Paired Nanoribbons," *ACS Nano*, vol. 6, no. 1, pp. 431–440, Jan. 2012.

[96] S. Kinoshita, S. Yoshioka, and J. Miyazaki, "Physics of structural colors," *Rep. Prog. Phys.*, vol. 71, no. 7, p. 076401, Jul. 2008.

[97] J. Teyssier, S. V. Saenko, D. van der Marel, and M. C. Milinkovitch, "Photonic crystals cause active colour change in chameleons," *Nat. Commun.*, vol. 6, Mar. 2015.

[98] R. W. Phillip and A. F. Bleikolm, "Optical coatings for document security," *Appl. Opt.*, vol. 35, no. 28, pp. 5529–5534, Oct. 1996.

[99] P. K. Jain, X. Huang, I. H. El-Sayed, and M. A. El-Sayed, "Noble Metals on the Nanoscale: Optical and Photothermal Properties and Some Applications in Imaging, Sensing, Biology, and Medicine," *Acc. Chem. Res.*, vol. 41, no. 12, pp. 1578–1586, Dec. 2008.

[100] K. Saito and T. Tatsuma, "Asymmetric Three-Way Plasmonic Color Routers," *Adv. Opt. Mater.*, p. n/a–n/a, Mar. 2015.

[101] M. Xiao, Y. Li, M. C. Allen, D. D. Deheyn, X. Yue, J. Zhao, N. C. Gianneschi, M. D. Shawkey, and A. Dhinojwala, "Bio-Inspired Structural Colors Produced via Self-Assembly of Synthetic Melanin Nanoparticles," *ACS Nano*, May 2015.

[102] H. Lochbihler, "Reflective colored image based on metal–dielectric–metal-coated gratings," *Opt. Lett.*, vol. 38, no. 9, pp. 1398–1400, May 2013.

[103] S. J. Tan, L. Zhang, D. Zhu, X. M. Goh, Y. M. Wang, K. Kumar, C.-W. Qiu, and J. K. W. Yang, "Plasmonic Color Palettes for Photorealistic Printing with Aluminum Nanostructures," *Nano Lett.*, vol. 14, no. 7, pp. 4023–4029, Jul. 2014.

[104] N. Sun, J. Cui, Y. She, L. Lu, J. Zheng, and Z. Ye, "Tunable spectral filters based on metallic nanowire gratings," *Opt. Mater. Express*, vol. 5, no. 4, pp. 912–919, Apr. 2015.

[105] B. Zeng, Y. Gao, and F. J. Bartoli, "Ultrathin Nanostructured Metals for Highly Transmissive Plasmonic Subtractive Color Filters," *Sci. Rep.*, vol. 3, Oct. 2013.

[106] K. Kumar, H. Duan, R. S. Hegde, S. C. W. Koh, J. N. Wei, and J. K. W. Yang, "Printing colour at the optical diffraction limit," *Nat. Nanotechnol.*, vol. 7, no. 9, pp. 557–561, Sep. 2012.

[107] J. S. Clausen, E. Højlund-Nielsen, A. B. Christiansen, S. Yazdi, M. Grajower, H. Taha, U. Levy, A. Kristensen, and N. A. Mortensen, "Plasmonic Metasurfaces for Coloration of Plastic Consumer Products," *Nano Lett.*, vol. 14, no. 8, pp. 4499–4504, Aug. 2014.

[108] Y. Gu, L. Zhang, J. K. W. Yang, S. P. Yeo, and C.-W. Qiu, "Color Generation via Subwavelength Plasmonic Nanostructures," *Nanoscale*, Mar. 2015.

[109] J. Sauvage-Vincent, S. Tonchev, C. Veillas, S. Reynaud, and Y. Jourlin, "Optical security device for document protection using plasmon resonant transmission through a thin corrugated metallic film embedded in a plastic foil," *J. Eur. Opt. Soc.-Rapid Publ.*, vol. 8, p. 13015, 2013.

[110] A. F. Kaplan, T. Xu, and L. J. Guo, "High efficiency resonance-based spectrum filters with tunable transmission bandwidth fabricated using nanoimprint lithography," *Appl. Phys. Lett.*, vol. 99, no. 14, p. 143111, Oct. 2011.

[111] Y.-K. R. Wu, A. E. Hollowell, C. Zhang, and L. J. Guo, "Angle-Insensitive Structural Colours based on Metallic Nanocavities and Coloured Pixels beyond the Diffraction Limit," *Sci. Rep.*, vol. 3, Feb. 2013.

[112] V. R. Shrestha, S.-S. Lee, E.-S. Kim, and D.-Y. Choi, "Aluminum Plasmonics Based Highly Transmissive Polarization-Independent Subtractive Color Filters Exploiting a Nanopatch Array," *Nano Lett.*, vol. 14, no. 11, pp. 6672–6678, Nov. 2014.

[113] J. G. Gordon II and J. D. Swalen, "The effect of thin organic films on the surface plasma resonance on gold," *Opt. Commun.*, vol. 22, no. 3, pp. 374–376, Sep. 1977.

[114] J. G. Gordon II and S. Ernst, "Surface plasmons as a probe of the electrochemical interface," *Surf. Sci.*, vol. 101, no. 1–3, pp. 499–506, Dec. 1980.

[115] J. Homola, "Surface Plasmon Resonance Sensors for Detection of Chemical and Biological Species," *Chem. Rev.*, vol. 108, no. 2, pp. 462–493, Feb. 2008.

[116] A. D. Taylor, J. Ladd, S. Etheridge, J. Deeds, S. Hall, and S. Jiang, "Quantitative detection of tetrodotoxin (TTX) by a surface plasmon resonance (SPR) sensor," *Sens. Actuators B Chem.*, vol. 130, no. 1, pp. 120–128, Mar. 2008.

[117] M. Piliarik, M. Vala, I. Tichý, and J. Homola, "Compact and low-cost biosensor based on novel approach to spectroscopy of surface plasmons," *Biosens. Bioelectron.*, vol. 24, no. 12, pp. 3430–3435, Aug. 2009.

[118] A. G. Brolo, R. Gordon, B. Leathem, and K. L. Kavanagh, "Surface Plasmon Sensor Based on the Enhanced Light Transmission through Arrays of Nanoholes in Gold Films," *Langmuir*, vol. 20, no. 12, pp. 4813–4815, Jun. 2004.

[119] X. D. Hoa, A. G. Kirk, and M. Tabrizian, "Towards integrated and sensitive surface plasmon resonance biosensors: A review of recent progress," *Biosens. Bioelectron.*, vol. 23, no. 2, pp. 151–160, Sep. 2007.

[120] T. R. Jensen, M. D. Malinsky, C. L. Haynes, and R. P. Van Duyne, "Nanosphere Lithography: Tunable Localized Surface Plasmon Resonance Spectra of Silver Nanoparticles," *J. Phys. Chem. B*, vol. 104, no. 45, pp. 10549–10556, Nov. 2000.

[121] K. A. Willets and R. P. Van Duyne, "Localized surface plasmon resonance spectroscopy and sensing," in *Annual Review of Physical Chemistry*, vol. 58, Palo Alto: Annual Reviews, 2007, pp. 267–297.

[122] Y. Shen, J. Zhou, T. Liu, Y. Tao, R. Jiang, M. Liu, G. Xiao, J. Zhu, Z.-K. Zhou, X. Wang, C. Jin, and J. Wang, "Plasmonic gold mushroom arrays with refractive index sensing figures of merit approaching the theoretical limit," *Nat. Commun.*, vol. 4, Aug. 2013.

[123] R. Ameling, L. Langguth, M. Hentschel, M. Mesch, P. V. Braun, and H. Giessen, "Cavity-enhanced localized plasmon resonance sensing," *Appl. Phys. Lett.*, vol. 97, no. 25, p. 253116, Dec. 2010.

[124] S. Chen, M. Svedendahl, R. P. V. Duyne, and M. Käll, "Plasmon-Enhanced Colorimetric ELISA with Single Molecule Sensitivity," *Nano Lett.*, vol. 11, no. 4, pp. 1826–1830, Apr. 2011.

[125] I. Ament, J. Prasad, A. Henkel, S. Schmachtel, and C. Sönnichsen, "Single Unlabeled Protein Detection on Individual Plasmonic Nanoparticles," *Nano Lett.*, vol. 12, no. 2, pp. 1092–1095, Feb. 2012.

[126] K. Saha, S. S. Agasti, C. Kim, X. Li, and V. M. Rotello, "Gold Nanoparticles in Chemical and Biological Sensing," *Chem. Rev.*, vol. 112, no. 5, pp. 2739–2779, May 2012.

[127] A. J. Haes and R. P. V. Duyne, "A unified view of propagating and localized surface plasmon resonance biosensors," *Anal. Bioanal. Chem.*, vol. 379, no. 7–8, pp. 920–930, Jul. 2004.

[128] M.-C. Estevez, M. A. Otte, B. Sepulveda, and L. M. Lechuga, "Trends and challenges of refractometric nanoplasmonic biosensors: A review," *Anal. Chim. Acta*, vol. 806, pp. 55–73, Jan. 2014.

[129] M. E. Stewart, C. R. Anderton, L. B. Thompson, J. Maria, S. K. Gray, J. A. Rogers, and R. G. Nuzzo, "Nanostructured Plasmonic Sensors," *Chem. Rev.*, vol. 108, no. 2, pp. 494–521, Feb. 2008.

[130] S. Lal, S. Link, and N. J. Halas, "Nano-optics from sensing to waveguiding," *Nat. Photonics*, vol. 1, no. 11, pp. 641–648, Nov. 2007.

[131] S. Lal, N. K. Grady, G. P. Goodrich, and N. J. Halas, "Profiling the Near Field of a Plasmonic Nanoparticle with Raman-Based Molecular Rulers," *Nano Lett.*, vol. 6, no. 10, pp. 2338–2343, Oct. 2006.

[132] T. Siegfried, M. Kind, A. Terfort, O. J. F. Martin, M. Zharnikov, N. Ballav, and H. Sigg, "Reusable plasmonic substrates fabricated by interference lithography: a platform for systematic sensing studies," *J. Raman Spectrosc.*, vol. 44, no. 2, pp. 170–175, Feb. 2013.

[133] E. C. Le Ru, E. Blackie, M. Meyer, and P. G. Etchegoin, "Surface Enhanced Raman Scattering Enhancement Factors: A Comprehensive Study," *J. Phys. Chem. C*, vol. 111, no. 37, pp. 13794–13803, Sep. 2007.

[134] Y.-C. Pu, G. Wang, K.-D. Chang, Y. Ling, Y.-K. Lin, B. C. Fitzmorris, C.-M. Liu, X. Lu, Y. Tong, J. Z. Zhang, Y.-J. Hsu, and Y. Li, "Au Nanostructure-Decorated TiO2 Nanowires Exhibiting Photoactivity Across Entire UV-visible Region for Photoelectrochemical Water Splitting," *Nano Lett.*, vol. 13, no. 8, pp. 3817–3823, Aug. 2013.

[135] R. de Waele, S. P. Burgos, A. Polman, and H. A. Atwater, "Plasmon Dispersion in Coaxial Waveguides from Single-Cavity Optical Transmission Measurements," *Nano Lett.*, vol. 9, no. 8, pp. 2832–2837, Aug. 2009.

[136] D. M. O'Carroll, C. E. Hofmann, and H. A. Atwater, "Conjugated Polymer/Metal Nanowire Heterostructure Plasmonic Antennas," *Adv. Mater.*, vol. 22, no. 11, pp. 1223–1227, Mar. 2010.

[137] M. Karg, T. A. F. König, M. Retsch, C. Stelling, P. M. Reichstein, T. Honold, M. Thelakkat, and A. Fery, "Colloidal self-assembly concepts for light management in photovoltaics," *Mater. Today*, vol. 18, no. 4, pp. 185–205, May 2015.

[138] S. Pillai, K. R. Catchpole, T. Trupke, and M. A. Green, "Surface plasmon enhanced silicon solar cells," *J. Appl. Phys.*, vol. 101, no. 9, p. 093105, May 2007.

[139] M. L. Brongersma, N. J. Halas, and P. Nordlander, "Plasmon-induced hot carrier science and technology," *Nat. Nanotechnol.*, vol. 10, no. 1, pp. 25–34, Jan. 2015.

[140] B. O'Regan and M. Grätzel, "A low-cost, high-efficiency solar cell based on dye-sensitized colloidal TiO2 films," *Nature*, vol. 353, no. 6346, pp. 737–740, Oct. 1991.

[141] S. Mubeen, J. Lee, N. Singh, S. Krämer, G. D. Stucky, and M. Moskovits, "An autonomous photosynthetic device in which all charge carriers derive from surface plasmons," *Nat. Nanotechnol.*, vol. 8, no. 4, pp. 247–251, Apr. 2013.

[142] C. Gomes Silva, R. Juárez, T. Marino, R. Molinari, and H. García, "Influence of Excitation Wavelength (UV or Visible Light) on the Photocatalytic Activity of Titania Containing Gold Nanoparticles for the Generation of Hydrogen or Oxygen from Water," *J. Am. Chem. Soc.*, vol. 133, no. 3, pp. 595–602, Jan. 2011.

[143] J. Mertz, "Radiative absorption, fluorescence, and scattering of a classical dipole near a lossless interface: a unified description," *J. Opt. Soc. Am. B*, vol. 17, no. 11, pp. 1906–1913, Nov. 2000.

[144] G. Li, R. Zhu, and Y. Yang, "Polymer solar cells," *Nat. Photonics*, vol. 6, no. 3, pp. 153–161, Mar. 2012.

[145] K. Marchuk and K. A. Willets, "Localized surface plasmons and hot electrons," *Chem. Phys.*, vol. 445, pp. 95–104, Dec. 2014.

[146] G. Sonavane, K. Tomoda, and K. Makino, "Biodistribution of colloidal gold nanoparticles after intravenous administration: Effect of particle size," *Colloids Surf. B Biointerfaces*, vol. 66, no. 2, pp. 274–280, Oct. 2008.

[147] N. Lewinski, V. Colvin, and R. Drezek, "Cytotoxicity of Nanoparticles," *Small*, vol. 4, no. 1, pp. 26–49, Jan. 2008.

[148] M. Brust, M. Walker, D. Bethell, D. J. Schiffrin, and R. Whyman, "Synthesis of thiol-derivatised gold nanoparticles in a two-phase Liquid–Liquid system," *J. Chem. Soc. Chem. Commun.*, no. 7, pp. 801–802, Jan. 1994.

[149] N. L. Rosi and C. A. Mirkin, "Nanostructures in Biodiagnostics," *Chem. Rev.*, vol. 105, no. 4, pp. 1547–1562, Apr. 2005.

[150] K. Sokolov, M. Follen, J. Aaron, I. Pavlova, A. Malpica, R. Lotan, and R. Richards-Kortum, "Real-Time Vital Optical Imaging of Precancer Using Anti-Epidermal Growth Factor Receptor Antibodies Conjugated to Gold Nanoparticles," *Cancer Res.*, vol. 63, no. 9, pp. 1999–2004, Jan. 2003.

[151] D. P. O'Neal, L. R. Hirsch, N. J. Halas, J. D. Payne, and J. L. West, "Photo-thermal tumor ablation in mice using near infrared-absorbing nanoparticles," *Cancer Lett.*, vol. 209, no. 2, pp. 171–176, Jun. 2004.

[152] E. C. Dreaden, S. C. Mwakwari, Q. H. Sodji, A. K. Oyelere, and M. A. El-Sayed, "Tamoxifen–Poly(ethylene glycol)–Thiol Gold Nanoparticle Conjugates: Enhanced Potency and Selective Delivery for Breast Cancer Treatment," *Bioconjug. Chem.*, vol. 20, no. 12, pp. 2247–2253, Dec. 2009.

[153] D. J. de Aberasturi, A. B. Serrano-Montes, and L. M. Liz-Marzán, "Modern Applications of Plasmonic Nanoparticles: From Energy to Health," *Adv. Opt. Mater.*, p. n/a–n/a, Feb. 2015.

[154] E. Boisselier and D. Astruc, "Gold nanoparticles in nanomedicine: preparations, imaging, diagnostics, therapies and toxicity," *Chem. Soc. Rev.*, vol. 38, no. 6, pp. 1759–1782, May 2009.

[155] J. Schanda, *Colorimetry: Understanding the CIE System*. John Wiley & Sons, 2007.

[156] M. D. Fairchild, *Color Appearance Models*. John Wiley & Sons, 2005.

[157] S. I. Newton, *Opticks:: Or, A Treatise of the Reflections, Refractions, Inflections and Colours of Light*. William Innys at the West-End of St. Paul's., 1730.

[158] B. Silliman, *First Principles of Physics: Or Natural Philosophy, Designed for the Use of Schools and Colleges*. H.C. Peck & T. Bliss, 1859.

[159] OpenStax Colleg, "Biology," 11-Jun-2013. [Online]. Available: http://cnx.org/contents/185cbf87-c72e-48f5-b51e-f14f21b5eabd@9.17/Biology. [Accessed: 09-Mar-2015].

[160] T. Young, "The Bakerian Lecture: On the Theory of Light and Colours," *Philos. Trans. R. Soc. Lond.*, vol. 92, pp. 12–48, Jan. 1802.

[161] *Technical Report: Colorimetry, CIE 15:2004, 3rd Edition.* Vienna: CIE, Central Bureau, 2004.

[162] "CIE - International Comission on Illumination." [Online]. Available: http://www.cie.co.at/. [Accessed: 13-May-2015].

[163] H. Lochbihler, "Colored images generated by metallic sub-wavelength gratings," *Opt. Express*, vol. 17, no. 14, pp. 12189–12196, Jul. 2009.

[164] M. Stokes, M. Anderson, S. Chandrasekar, and R. Motta, "A Standard Default Color Space for the Internet - sRGB." [Online]. Available: https://www.scribd.com/doc/189817894/A-Standard-Default-Color-Space-for-the-Internet-sRGB. [Accessed: 24-Apr-2015].

[165] S. Westland and C. Ripamonti, *Computational colour science using MATLAB*. Hoboken, NJ: J. Wiley, 2004.

[166] University of Eastern Finland, Spectral Color Research Group, "www.uef.fi - Spectral Database." [Online]. Available: https://www.uef.fi/fi/spectral/spectral-database. [Accessed: 25-Feb-2015].

[167] C. Vieu, F. Carcenac, A. Pépin, Y. Chen, M. Mejias, A. Lebib, L. Manin-Ferlazzo, L. Couraud, and H. Launois, "Electron beam lithography: resolution limits and applications," *Appl. Surf. Sci.*, vol. 164, no. 1–4, pp. 111–117, Sep. 2000.

[168] N. C. Lindquist, P. Nagpal, K. M. McPeak, D. J. Norris, and S.-H. Oh, "Engineering metallic nanostructures for plasmonics and nanophotonics," *Rep. Prog. Phys.*, vol. 75, no. 3, p. 036501, Mar. 2012.

[169] J. Dong, J. Liu, G. Kang, J. Xie, and Y. Wang, "Pushing the resolution of photolithography down to 15nm by surface plasmon interference," *Sci. Rep.*, vol. 4, Jul. 2014.

[170] S. Y. Chou, P. R. Krauss, W. Zhang, L. J. Guo, and L. Zhuang, "Sub-10 nm imprint lithography and applications," *J. Vac. Sci. Technol. B*, vol. 15, no. 6, pp. 2897–2904, Dec. 1997.

[171] T. Levola and P. Laakkonen, "Replicated slanted gratings with a high refractive index material for in and outcoupling of light," *Opt. Express*, vol. 15, no. 5, pp. 2067–2074, Mar. 2007.

[172] C. L. Haynes and R. P. Van Duyne, "Nanosphere Lithography: A Versatile Nanofabrication Tool for Studies of Size-Dependent Nanoparticle Optics," *J. Phys. Chem. B*, vol. 105, no. 24, pp. 5599–5611, Jun. 2001.

[173] P. Hanarp, M. Käll, and D. S. Sutherland, "Optical Properties of Short Range Ordered Arrays of Nanometer Gold Disks Prepared by Colloidal Lithography," *J. Phys. Chem. B*, vol. 107, no. 24, pp. 5768–5772, Jun. 2003.

[174] M. C. Gwinner, E. Koroknay, L. Fu, P. Patoka, W. Kandulski, M. Giersig, and H. Giessen, "Periodic Large-Area Metallic Split-Ring Resonator Metamaterial Fabrication Based on Shadow Nanosphere Lithography," *Small*, vol. 5, no. 3, pp. 400–406, Feb. 2009.

[175] A. J. Haes and R. P. Van Duyne, "A nanoscale optical biosensor: Sensitivity and selectivity of an approach based on the localized surface plasmon resonance spectroscopy of triangular silver nanoparticles," *J. Am. Chem. Soc.*, vol. 124, no. 35, pp. 10596–10604, Sep. 2002.

[176] K. M. McPeak, S. V. Jayanti, S. J. P. Kress, S. Meyer, S. Iotti, A. Rossinelli, and D. J. Norris, "Plasmonic Films Can Easily Be Better: Rules and Recipes," *ACS Photonics*, Feb. 2015.

[177] H. Qiu, F. Wang, P. Wu, L. Pan, L. Li, L. Xiong, and Y. Tian, "Effect of deposition rate on structural and electrical properties of Al films deposited on glass by electron beam evaporation," *Thin Solid Films*, vol. 414, no. 1, pp. 150–153, Jul. 2002.

[178] T. Siegfried, Y. Ekinci, O. J. F. Martin, and H. Sigg, "Engineering Metal Adhesion Layers That Do Not Deteriorate Plasmon Resonances," *ACS Nano*, vol. 7, no. 3, pp. 2751–2757, Mar. 2013.

[179] C.-J. Ting, F.-Y. Chang, C.-F. Chen, and C. P. Chou, "Fabrication of an antireflective polymer optical film with subwavelength structures using a roll-to-roll micro-replication process," *J. Micromechanics Microengineering*, vol. 18, no. 7, p. 075001, Jul. 2008.

[180] L. Yu, C. G. Koh, L. J. Lee, K. W. Koelling, and M. J. Madou, "Experimental investigation and numerical simulation of injection molding with micro-features," *Polym. Eng. Sci.*, vol. 42, no. 5, pp. 871–888, 2002.

[181] K. Du, I. Wathuthanthri, Y. Liu, W. Xu, and C.-H. Choi, "Wafer-Scale Pattern Transfer of Metal Nanostructures on Polydimethylsiloxane (PDMS) Substrates via Holographic Nanopatterns," *ACS Appl. Mater. Interfaces*, vol. 4, no. 10, pp. 5505–5514, Oct. 2012.

[182] P. Nagpal, N. C. Lindquist, S.-H. Oh, and D. J. Norris, "Ultrasmooth Patterned Metals for Plasmonics and Metamaterials," *Science*, vol. 325, no. 5940, pp. 594–597, Jul. 2009.

[183] R. Liedert, L. K. Amundsen, A. Hokkanen, M. Mäki, A. Aittakorpi, M. Pakanen, J. R. Scherer, R. A. Mathies, M. Kurkinen, S. Uusitalo, L. Hakalahti, T. K. Nevanen, H. Siitari, and H. Söderlund, "Disposable roll-to-roll hot embossed electrophoresis chip for detection of antibiotic resistance genemecA in bacteria," *Lab. Chip*, vol. 12, no. 2, pp. 333–339, Dec. 2011.

[184] S. H. Ahn and L. J. Guo, "High-Speed Roll-to-Roll Nanoimprint Lithography on Flexible Plastic Substrates," *Adv. Mater.*, vol. 20, no. 11, pp. 2044–2049, 2008.

[185] S. H. Ahn and L. J. Guo, "Large-Area Roll-to-Roll and Roll-to-Plate Nanoimprint Lithography: A Step toward High-Throughput Application of Continuous Nanoimprinting," *ACS Nano*, vol. 3, no. 8, pp. 2304–2310, Aug. 2009.

[186] H. Osaki, "Tribology of videotapes," *Wear*, vol. 200, no. 1–2, pp. 244–251, 1996.

[187] X.-M. Yan, A. M. Contreras, M. M. Koebel, J. A. Liddle, and G. A. Somorjai, "Parallel Fabrication of Sub-50-nm Uniformly Sized Nanoparticles by Deposition through a Patterned Silicon Nitride Nanostencil," *Nano Lett.*, vol. 5, no. 6, pp. 1129–1134, Jun. 2005.

[188] M. Matschuk and N. B. Larsen, "Injection molding of high aspect ratio sub-100 nm nanostructures," *J. Micromechanics Microengineering*, vol. 23, no. 2, Feb. 2013.

[189] J. Saarinen, E. Noponen, J. Turunen, T. Suhara, and H. Nishihara, "Asymmetric Beam Deflection by Doubly Grooved Binary Gratings," *Appl. Opt.*, vol. 34, no. 14, pp. 2401–2405, May 1995.

[190] M. G. Moharam and T. K. Gaylord, "Rigorous coupled-wave analysis of planar-grating diffraction," *J. Opt. Soc. Am.*, vol. 71, no. 7, p. 811, Jul. 1981.

[191] M. G. Moharam and T. K. Gaylord, "Diffraction analysis of dielectric surface-relief gratings," *J. Opt. Soc. Am.*, vol. 72, no. 10, p. 1385, Oct. 1982.

[192] K. Han and C.-H. Chang, "Numerical Modeling of Sub-Wavelength Anti-Reflective Structures for Solar Module Applications," *Nanomaterials*, vol. 4, no. 1, pp. 87–128, Jan. 2014.

[193] T. Clausnitzer, T. Kämpfe, E.-B. Kley, A. Tünnermann, U. Peschel, A. V. Tishchenko, and O. Parriaux, "An intelligible explanation of highly-efficient diffraction in deep dielectric rectangular transmission gratings," *Opt. Express*, vol. 13, no. 26, pp. 10448–10456, Dec. 2005.

[194] A. M. Kern and O. J. Martin, "Surface integral formulation for 3D simulations of plasmonic and high permittivity nanostructures," *J. Opt. Soc. Am. A*, vol. 26, no. 4, p. 732, Apr. 2009.

[195] B. Gallinet, A. M. Kern, and O. J. F. Martin, "Accurate and versatile modeling of electro-magnetic scattering on periodic nanostructures with a surface integral approach," *J. Opt. Soc. Am. A*, vol. 27, no. 10, p. 2261, Oct. 2010.

[196] X. Jing, J. Zhang, S. Jin, P. Liang, and Y. Tian, "Design of highly efficient transmission gratings with deep etched triangular grooves," *Appl. Opt.*, vol. 51, no. 33, pp. 7920–7933, Nov. 2012.

[197] P. Lalanne, S. Astilean, P. Chavel, E. Cambril, and H. Launois, "Design and fabrication of blazed binary diffractive elements with sampling periods smaller than the structural cut-off," *J. Opt. Soc. Am. A*, vol. 16, no. 5, p. 1143, 1999.

[198] O. Sandfuchs, R. Brunner, D. Pätz, S. Sinzinger, and J. Ruoff, "Rigorous analysis of shadowing effects in blazed transmission gratings," *Opt. Lett.*, vol. 31, no. 24, p. 3638, 2006.

[199] B. Goebel, L. L. Wang, and T. Tschudi, "Multilayer technology for diffractive optical elements," *Appl. Opt.*, vol. 35, no. 22, p. 4490, Aug. 1996.

[200] C. David, "Fabrication of stair-case profiles with high aspect ratios for blazed diffractive optical elements," *Microelectron. Eng.*, vol. 53, no. 1–4, pp. 677–680, Jun. 2000.

[201] M. Oliva, D. Michaelis, F. Fuchs, A. Tünnermann, and U. D. Zeitner, "Highly efficient broad-band blazed grating in resonance domain," *Appl. Phys. Lett.*, vol. 102, no. 20, p. 203114, May 2013.

[202] D. C. Flanders, "Submicrometer periodicity gratings as artificial anisotropic dielectrics," *Appl. Phys. Lett.*, vol. 42, no. 6, pp. 492–494, Mar. 1983.

[203] H. Iizuka, N. Engheta, H. Fujikawa, K. Sato, and Y. Takeda, "Role of propagating modes in a double-groove grating with a +1st-order diffraction angle larger than the substrate-air critical angle," *Opt. Lett.*, vol. 35, no. 23, pp. 3973–3975, Dec. 2010.

[204] P. Lalanne, S. Astilean, *Pierre Chavel, E. Cambril, and H. Launois, "Blazed binary sub-wavelength gratings with efficiencies larger than those of conventional échelette gratings," *Opt. Lett.*, vol. 23, no. 14, p. 1081, Jul. 1998.

[205] J. M. Miller, N. deBeaucoudrey, P. Chavel, J. Turunen, and E. Cambril, "Design and fabrication of binary slanted surface-relief gratings for a planar optical interconnection," *Appl. Opt.*, vol. 36, no. 23, pp. 5717–5727, Aug. 1997.

[206] B.-O. Cho, S.-W. Hwang, J.-H. Ryu, I.-W. Kim, and S.-H. Moon, "Fabrication Method for Surface Gratings Using a Faraday Cage in a Conventional Plasma Etching Apparatus," *Electrochem. Solid-State Lett.*, vol. 2, no. 3, pp. 129–130, Jan. 1999.

[207] S. Astilean, P. Lalanne, P. Chavel, E. Cambril, and H. Launois, "High-efficiency subwavelength diffractive element patterned in a high-refractive-index material for 633 nm," *Opt. Lett.*, vol. 23, no. 7, pp. 552–554, Apr. 1998.

[208] F. Lütolf, M. Stalder, and O. J. F. Martin, "Up-scalable method to amplify the diffraction efficiency of simple gratings," *Opt. Lett.*, vol. 39, no. 23, pp. 6557–6560, Dec. 2014.

[209] F. Lutolf, M. Stalder, and G. Basset, "Optical Grating Coupling Structure," WO2015062641 (A1), 07-May-2015.

[210] D. Flanders and A. White, "Application of Almost-Equal-to 100 a Linewidth Structures Fabricated by Shadowing Techniques," *J. Vac. Sci. Technol.*, vol. 19, no. 4, pp. 892–896, 1981.

[211] M. Bass, C. DeCusatis, J. Enoch, V. Lakshminarayanan, G. Li, C. MacDonald, V. Mahajan, and E. V. Stryland, *Handbook of Optics, Third Edition Volume IV: Optical Properties of Materials, Nonlinear Optics, Quantum Optics (set)*. McGraw Hill Professional, 2009.

[212] Y. Ye, R. Shao, Y. Zhou, and L. Chen, "Wide-angle transmissive filter based on a guided-mode resonant grating," *Appl. Opt.*, vol. 51, no. 24, pp. 5785–5790, Aug. 2012.

[213] A. Rakic, "Algorithm for the Determination of Intrinsic Optical-Constants of Metal-Films - Application to Aluminum," *Appl. Opt.*, vol. 34, no. 22, pp. 4755–4767, Aug. 1995.

[214] B. Bai, X. Meng, J. Laukkanen, T. Sfez, L. Yu, W. Nakagawa, H. P. Herzig, L. Li, and J. Turunen, "Asymmetrical excitation of surface plasmon polaritons on blazed gratings at normal incidence," *Phys. Rev. B*, vol. 80, no. 3, p. 035407, Jul. 2009.

[215] A. Baron, E. Devaux, J.-C. Rodier, J.-P. Hugonin, E. Rousseau, C. Genet, T. W. Ebbesen, and P. Lalanne, "Compact Antenna for Efficient and Unidirectional Launching and Decoupling of Surface Plasmons," *Nano Lett.*, vol. 11, no. 10, pp. 4207–4212, Oct. 2011.

[216] C. Palmer and E. Loewen, *Diffraction Grating Handbook*, Sixth Edition, 6th edition. Newport Corporation, 2005.

[217] D. Crouse and P. Keshavareddy, "Polarization independent enhanced optical transmission in one-dimensional gratings and device applications," *Opt. Express*, vol. 15, no. 4, pp. 1415–1427, Feb. 2007.

[218] L. Martín-Moreno, F. J. García-Vidal, H. J. Lezec, K. M. Pellerin, T. Thio, J. B. Pendry, and T. W. Ebbesen, "Theory of Extraordinary Optical Transmission through Subwavelength Hole Arrays," *Phys. Rev. Lett.*, vol. 86, no. 6, pp. 1114–1117, Feb. 2001.

[219] Q. Cao and P. Lalanne, "Negative Role of Surface Plasmons in the Transmission of Metallic Gratings with Very Narrow Slits," *Phys. Rev. Lett.*, vol. 88, no. 5, p. 057403, Jan. 2002.

[220] H. Lezec and T. Thio, "Diffracted evanescent wave model for enhanced and suppressed optical transmission through subwavelength hole arrays," *Opt. Express*, vol. 12, no. 16, pp. 3629–3651, Aug. 2004.

[221] N. Bonod, E. Popov, L. Li, and B. Chernov, "Unidirectional excitation of surface plasmons by slanted gratings," *Opt. Express*, vol. 15, no. 18, pp. 11427–11432, Sep. 2007.

[222] H. Lochbihler, "Surface polaritons on gold-wire gratings," *Phys. Rev. B*, vol. 50, no. 7, pp. 4795–4801, Aug. 1994.

[223] J. A. Porto, F. J. Garcia-Vidal, and J. B. Pendry, "Transmission resonances on metallic gratings with very narrow slits," *Phys. Rev. Lett.*, vol. 83, no. 14, pp. 2845–2848, Oct. 1999.

[224] B. Ung and Y. Sheng, "Interference of surface waves in a metallic nanoslit," *Opt. Express*, vol. 15, no. 3, pp. 1182–1190, Feb. 2007.

[225] J. Weiner, "The physics of light transmission through subwavelength apertures and aperture arrays," *Rep. Prog. Phys.*, vol. 72, no. 6, p. 064401, Jun. 2009.

[226] T. Siegfried, Y. Ekinci, O. J. F. Martin, and H. Sigg, "Gap Plasmons and Near-Field Enhancement in Closely Packed Sub-10 nm Gap Resonators," *Nano Lett.*, vol. 13, no. 11, pp. 5449–5453, Nov. 2013.

[227] F. J. Garcia-Vidal, L. Martin-Moreno, T. W. Ebbesen, and L. Kuipers, "Light passing through subwavelength apertures," *Rev. Mod. Phys.*, vol. 82, no. 1, pp. 729–787, Mar. 2010.

[228] K. L. van der Molen, K. J. Klein Koerkamp, S. Enoch, F. B. Segerink, N. F. van Hulst, and L. Kuipers, "Role of shape and localized resonances in extraordinary transmission through periodic arrays of subwavelength holes: Experiment and theory," *Phys. Rev. B*, vol. 72, no. 4, p. 045421, Jul. 2005.

[229] H. Liu and P. Lalanne, "Microscopic theory of the extraordinary optical transmission," *Nature*, vol. 452, no. 7188, pp. 728–731, Apr. 2008.

[230] M. V. Sosnova, N. L. Dmitruk, A. V. Korovin, S. V. Mamykin, V. I. Mynko, and O. S. Lytvyn, "Local plasmon excitations in one-dimensional array of metal nanowires for sensor applications," *Appl. Phys. B*, vol. 99, no. 3, pp. 493–497, Nov. 2009.

[231] C. Escobedo, "On-chip nanohole array based sensing: a review," *Lab. Chip*, vol. 13, no. 13, pp. 2445–2463, Jun. 2013.

[232] A. Lesuffleur, H. Im, N. C. Lindquist, and S.-H. Oh, "Periodic nanohole arrays with shape-enhanced plasmon resonance as real-time biosensors," *Appl. Phys. Lett.*, vol. 90, no. 24, p. 243110, Jun. 2007.

[233] B. Y. Zheng, Y. Wang, P. Nordlander, and N. J. Halas, "Color-Selective and CMOS-Compatible Photodetection Based on Aluminum Plasmonics," *Adv. Mater.*, vol. 26, no. 36, pp. 6318–6323, Sep. 2014.

[234] C. Rockstuhl, S. Fahr, and F. Lederer, "Absorption enhancement in solar cells by localized plasmon polaritons," *J. Appl. Phys.*, vol. 104, no. 12, p. 123102, Dec. 2008.

[235] P. Lalanne and H. Liu, "A New Look at Grating Theories Through the Extraordinary Optical Transmission Phenomenon," in *Plasmonics*, S. Enoch and N. Bonod, Eds. Springer Berlin Heidelberg, 2012, pp. 85–103.

[236] B. Gallinet and O. J. F. Martin, "Influence of Electromagnetic Interactions on the Line Shape of Plasmonic Fano Resonances," *ACS Nano*, vol. 5, no. 11, pp. 8999–9008, Nov. 2011.

[237] N. Verellen, Y. Sonnefraud, H. Sobhani, F. Hao, V. V. Moshchalkov, P. V. Dorpe, P. Nordlander, and S. A. Maier, "Fano Resonances in Individual Coherent Plasmonic Nanocavities," *Nano Lett.*, vol. 9, no. 4, pp. 1663–1667, Apr. 2009.

[238] B. Luk'yanchuk, N. I. Zheludev, S. A. Maier, N. J. Halas, P. Nordlander, H. Giessen, and C. T. Chong, "The Fano resonance in plasmonic nanostructures and metamaterials," *Nat. Mater.*, vol. 9, no. 9, pp. 707–715, Sep. 2010.

[239] M. Sarrazin, J.-P. Vigneron, and J.-M. Vigoureux, "Role of Wood anomalies in optical properties of thin metallic films with a bidimensional array of subwavelength holes," *Phys. Rev. B*, vol. 67, no. 8, p. 085415, Feb. 2003.

[240] V. A. Fedotov, M. Rose, S. L. Prosvirnin, N. Papasimakis, and N. I. Zheludev, "Sharp trapped-mode resonances in planar metamaterials with a broken structural symmetry," *Phys. Rev. Lett.*, vol. 99, no. 14, p. 147401, Oct. 2007.

[241] J. Zhao, C. Zhang, P. V. Braun, and H. Giessen, "Large-Area Low-Cost Plasmonic Nanostructures in the NIR for Fano Resonant Sensing," *Adv. Mater.*, vol. 24, no. 35, pp. OP247–OP252, Sep. 2012.

[242] B. Gallinet and O. J. Martin, "Ab initio theory of Fano resonances in plasmonic nanostructures and metamaterials," *Phys. Rev. B*, vol. 83, no. 23, p. 235427, 2011.

[243] M. Rahmani, B. Luk'yanchuk, and M. Hong, "Fano resonance in novel plasmonic nanostructures," *Laser Photonics Rev.*, vol. 7, no. 3, pp. 329–349, May 2013.

[244] A. Christ, T. Zentgraf, J. Kuhl, S. G. Tikhodeev, N. A. Gippius, and H. Giessen, "Optical properties of planar metallic photonic crystal structures: Experiment and theory," *Phys. Rev. B*, vol. 70, no. 12, p. 125113, Sep. 2004.

[245] B. Gallinet, L. Davoine, G. Basset, and M. Schnieper, "Up-scalable low-cost fabrication of plasmonic and photonic nanostructures for sensing," 2013, vol. 8818, p. 88180Z–88180Z–6.

[246] A. Christ, O. J. F. Martin, Y. Ekinci, N. A. Gippius, and S. G. Tikhodeev, "Symmetry Breaking in a Plasmonic Metamaterial at Optical Wavelength," *Nano Lett.*, vol. 8, no. 8, pp. 2171–2175, Aug. 2008.

[247] B. Gallinet and O. J. F. Martin, "Relation between near–field and far–field properties of plasmonic Fano resonances," *Opt. Express*, vol. 19, no. 22, p. 22167, Oct. 2011.

[248] F. Hao, Y. Sonnefraud, P. V. Dorpe, S. A. Maier, N. J. Halas, and P. Nordlander, "Symmetry Breaking in Plasmonic Nanocavities: Subradiant LSPR Sensing and a Tunable Fano Resonance," *Nano Lett.*, vol. 8, no. 11, pp. 3983–3988, Nov. 2008.

[249] A. E. Miroshnichenko, S. Flach, and Y. S. Kivshar, "Fano resonances in nanoscale structures," *Rev. Mod. Phys.*, vol. 82, no. 3, pp. 2257–2298, Aug. 2010.

[250] L. Zhu, J. Kapraun, J. Ferrara, and C. J. Chang-Hasnain, "Flexible photonic metastructures for tunable coloration," *Optica*, vol. 2, no. 3, p. 255, Mar. 2015.

[251] X. Han, Y. Liu, and Y. Yin, "Colorimetric Stress Memory Sensor Based on Disassembly of Gold Nanoparticle Chains," *Nano Lett.*, vol. 14, no. 5, pp. 2466–2470, May 2014.

[252] L. Davoine, V. Paeder, G. Basset, M. Schnieper, and H. P. Herzig, "Resonant absorption of a chemically sensitive layer based on waveguide gratings," *Appl. Opt.*, vol. 52, no. 3, pp. 340–349, Jan. 2013.

[253] R. Melik, E. Unal, N. K. Perkgoz, C. Puttlitz, and H. V. Demir, "Flexible metamaterials for wireless strain sensing," *Appl. Phys. Lett.*, vol. 95, no. 18, p. 181105, Nov. 2009.

[254] A. Barbara, P. Quémerais, E. Bustarret, and T. Lopez-Rios, "Optical transmission through subwavelength metallic gratings," *Phys. Rev. B*, vol. 66, no. 16, Oct. 2002.

[255] H. Gao, C. Gu, Z. Y. Zheng, S. J. Chen, and H. Y. Hao, "Nearly perfect absorption in a single-layer metallic grating with rectangular grooves on its front surface," *Appl. Phys. B*, pp. 1–9, Jul. 2014.

[256] V. I. Belotelov, A. N. Kalish, A. K. Zvezdin, A. V. Gopal, and A. S. Vengurlekar, "Fabry-Perot plasmonic structures for nanophotonics," *J. Opt. Soc. Am. B-Opt. Phys.*, vol. 29, no. 3, pp. 294–299, Mar. 2012.

[257] H.-Q. Li, K.-J. Wang, Z.-G. Yang, and J.-S. Liu, "Unexpected unidirectional perfect absorption of light in a freestanding optical thin metallic grating with extremely small filling factor," *J. Opt. Soc. Am. B-Opt. Phys.*, vol. 31, no. 4, pp. 806–809, Apr. 2014.

[258] S. Collin, F. Pardo, R. Teissier, and J.-L. Pelouard, "Horizontal and vertical surface resonances in transmission metallic gratings," *J. Opt. Pure Appl. Opt.*, vol. 4, no. 5, p. S154, Sep. 2002.

[259] A. Feuerstein and M. Mayr, "High-Vacuum Evaporation of Ferromagnetic Materials - a New Production Technology for Magnetic Tapes," *Ieee Trans. Magn.*, vol. 20, no. 1, pp. 51–56, 1984.

[260] P. B. Johnson and R. W. Christy, "Optical Constants of the Noble Metals," *Phys. Rev. B*, vol. 6, no. 12, pp. 4370–4379, Dec. 1972.

[261] D. Crouse and P. Keshavareddy, "Role of optical and surface plasmon modes in enhanced transmission and applications," *Opt. Express*, vol. 13, no. 20, pp. 7760–7771, Oct. 2005.

[262] A. Roszkiewicz and W. Nasalski, "Resonant transmission enhancement at one-dimensional metal gratings," *J. Phys. B At. Mol. Opt. Phys.*, vol. 46, no. 2, p. 025401, Jan. 2013.

[263] Y. Jourlin, S. Tonchev, A. V. Tishchenko, and O. Parriaux, "Sharp Plasmon-Mediated Resonant Reflection From an Undulated Metal Layer," *IEEE Photonics J.*, vol. 6, no. 5, pp. 1–6, Oct. 2014.

[264] R. Verre, Z. J. Yang, T. Shegai, and M. Käll, "Optical Magnetism and Plasmonic Fano Resonances in Metal–Insulator–Metal Oligomers," *Nano Lett.*, 2015.

[265] M. A. Kats, N. Yu, P. Genevet, Z. Gaburro, and F. Capasso, "Effect of radiation damping on the spectral response of plasmonic components," *Opt. Express*, vol. 19, no. 22, pp. 21748–21753, Oct. 2011.

[266] D. K. Gramotnev and S. I. Bozhevolnyi, "Plasmonics beyond the diffraction limit," *Nat. Photonics*, vol. 4, no. 2, pp. 83–91, Feb. 2010.

[267] L. Gao, Y. Zhang, H. Zhang, S. Doshay, X. Xie, H. Luo, D. Shah, Y. Shi, S. Xu, H. Fang, J. A. Fan, P. Nordlander, Y. Huang, and J. A. Rogers, "Optics and Nonlinear Buckling Mechanics in Large-Area, Highly Stretchable Arrays of Plasmonic Nanostructures," *ACS Nano*, Apr. 2015.

[268] J. Zhou, Y. Gu, P. Fei, W. Mai, Y. Gao, R. Yang, G. Bao, and Z. L. Wang, "Flexible Piezotronic Strain Sensor," *Nano Lett.*, vol. 8, no. 9, pp. 3035–3040, Sep. 2008.

[269] B. Lee, "Review of the present status of optical fiber sensors," *Opt. Fiber Technol.*, vol. 9, no. 2, pp. 57–79, Apr. 2003.

[270] A. M. R. Pinto and M. Lopez-Amo, "Photonic Crystal Fibers for Sensing Applications," *J. Sens.*, vol. 2012, p. e598178, Apr. 2012.

[271] T. Chen, S. Li, and H. Sun, "Metamaterials Application in Sensing," *Sensors*, vol. 12, no. 3, pp. 2742–2765, Feb. 2012.

[272] C. I. Aguirre, E. Reguera, and A. Stein, "Tunable Colors in Opals and Inverse Opal Photonic Crystals," *Adv. Funct. Mater.*, vol. 20, no. 16, pp. 2565–2578, Aug. 2010.

[273] H. Fudouzi and T. Sawada, "Photonic Rubber Sheets with Tunable Color by Elastic Deformation," *Langmuir*, vol. 22, no. 3, pp. 1365–1368, Jan. 2006.

[274] D. Ge, E. Lee, L. Yang, Y. Cho, M. Li, D. S. Gianola, and S. Yang, "A Robust Smart Window: Reversibly Switching from High Transparency to Angle-Independent Structural Color Display," *Adv. Mater.*, vol. 27, no. 15, pp. 2489–2495, Apr. 2015.

[275] X. Zhu, L. Shi, X. Liu, J. Zi, and Z. Wang, "A mechanically tunable plasmonic structure composed of a monolayer array of metal-capped colloidal spheres on an elastomeric substrate," *Nano Res.*, vol. 3, no. 11, pp. 807–812, Oct. 2010.

[276] X. Zhang, J. Zhang, H. Liu, X. Su, and L. Wang, "Soft plasmons with stretchable spectroscopic response based on thermally patterned gold nanoparticles," *Sci. Rep.*, vol. 4, Feb. 2014.

[277] S. Noda, K. Tomoda, N. Yamamoto, and A. Chutinan, "Full Three-Dimensional Photonic Bandgap Crystals at Near-Infrared Wavelengths," *Science*, vol. 289, no. 5479, pp. 604–606, Jul. 2000.

[278] M. Campbell, D. N. Sharp, M. T. Harrison, R. G. Denning, and A. J. Turberfield, "Fabrication of photonic crystals for the visible spectrum by holographic lithography," *Nature*, vol. 404, no. 6773, pp. 53–56, Mar. 2000.

[279] C. G. Schäfer, B. Viel, G. P. Hellmann, M. Rehahn, and M. Gallei, "Thermo-cross-linked Elastomeric Opal Films," *ACS Appl. Mater. Interfaces*, vol. 5, no. 21, pp. 10623–10632, Nov. 2013.

[280] "LASSIE-FP7 | Large Area Solid State Intelligent Efficient luminaires." [Online]. Available: http://lassie-fp7.eu/. [Accessed: 16-Jul-2015].

[281] D. S. Michael, "Projection display with grating arranged to avoid double images," GB2494115 (A), 06-Mar-2013.

[282] R. A. Barry and P. Wiltzius, "Humidity-Sensing Inverse Opal Hydrogels," *Langmuir*, vol. 22, no. 3, pp. 1369–1374, Jan. 2006.

[283] C. Zhang, A.-X. Yin, R. Jiang, J. Rong, L. Dong, T. Zhao, L.-D. Sun, J. Wang, X. Chen, and C.-H. Yan, "Time–Temperature Indicator for Perishable Products Based on Kinetically Programmable Ag Overgrowth on Au Nanorods," *ACS Nano*, vol. 7, no. 5, pp. 4561–4568, May 2013.

List of Abbreviations

AFM	Atomic force microscope
CIE	Commission internationale de l'éclairage
CM	Cavity Mode
CSEM	Centre Suisse Electronique et Microtechnique
DID	Diffractive identification device
EBL	Electron beam lithography
EFIE	Electric field integral equation
EOT	Extraordinary optical transmission
ETFE	Ethylene tetrafluoroethylene
FIB	Focused ion beam
IR	Infrared
LCD	Liquid-crystal display
LED	Light-emitting diode
LIL	Laser interference lithography
LSPR	Localized surface plasmon resonance
NIL	Nano imprint lithography
OVD	Optically variable device
PC	Polycarbonate
PDMS	Polydimethylsiloxane
PET	Polyethylene terephthalate
PMMA	Polymethylmethacrylate
PTFE	Polytetrafluoroethylene
PU	Polyurethane
PVD	Physical vapor deposition
R0, R1, R−1	zero/first/minus first reflection order
RCWA	Rigorous coupled wave analysis

sRGB	Standard red green blue
SEM	Scanning electron microscope
SIE	Surface integral equation
SPP	Surface plasmon polariton
T0, T1, T−1	zero/first/minus first transmission order
TE	Transverse electric polarization
TIR	Total internal reflection
TM	Transverse magnetic polarization
UV	Ultraviolet
WR	Wood–Rayleigh
ZnS	Zinc sulfide

Acknowledgements

Curriculum Vitae

Personal data

Name: Fabian Michael Lütolf

Born: November 28, 1985, Zofingen, CH

Address: Schönaustrasse 82, 4058 Basel

E-Mail: fabian.luetolf@gmx.net

Education

2011–present: PhD candidate at the Centre Suisse d' Electronique et Microtechnique (CSEM SA), enrolled in the Photonics doctoral school program at the Ecole polytechnique fédérale de Lausanne (EPFL)

2013: Bachelor of Arts in Business and Economics, Major in Business, University of Basel

2008–2010: Master of Science in Nanoscience, University of Basel, thesis in collaboration with CSEM

2004–2008: Bachelor of Science in Nanoscience, University of Basel

Languages

German: Native

English: Fluent

French: Conversational

Italian: Elementary

Publications

F. Lütolf, O. J. F. Martin, and B. Gallinet "Plasmonic Strain-Sensing with Fano-Resonant Nanowires," in preparation

F. Lütolf, O. J. F. Martin, and B. Gallinet "Fano-Resonant Aluminum and Gold Nanostructures Created with a Tunable, Up-Scalable Process," submitted

F. Lütolf, M. Stalder, and O. J. F. Martin, "Metallized gratings enable color and floating image effects by first order diffraction," submitted

F. Lütolf, M. Stalder, and O. J. F. Martin, "Up-scalable method to amplify the diffraction efficiency of simple gratings," Opt. Lett., vol. 39, no. 23, pp. 6557–6560, Dec. 2014.

Patents

F. Lutolf, M. Stalder, and G. Basset, "Optical Grating Coupling Structure," WO2015062641 (A1), 07–May–2015.

A. Hafner, M. Von Mühlenen, O. Enger, B. Gallinet, R. Ferrini, N. Marjanovic, M. Stalder, W. Tschanun, and G. Basset, "Solar Light Management," WO2015007580 (A1), 22–Jan–2015. (My name is currently missing but will be added when next published)

Conference contributions

F. Lütolf, "Optical effects in asymmetric metal gratings," Oral presentation, EOSAM, Berlin, Germany, September 2014

F. Lütolf, "Up–Scalable Method to Amplify the 1st Order Transmittance of Simple Gratings," Oral Presentation, Bragg Gratings, Photosensitivity, and Poling in Glass Waveguides by OSA, Barcelona, Spain, July 2014

F. Lütolf, L. Dümpelmann, C. Bosshard "Custom Nanostructures: From Design to Applications," Poster, Swiss Nano Convention, Brugg Windisch, Switzerland, May 2014